Optical Methods

for Studying Cell Mechanics

by

Yunze Yang

A Dissertation Presented in Partial Fulfillment
of the Requirements for the Degree
Doctor of Philosophy

Approved March 2016 by the
Graduate Supervisory Committee:

Nongjian Tao, Chair
Shaopeng Wang
Michael Goryll
Jennie Si

ARIZONA STATE UNIVERSITY

May 2016

ABSTRACT

Mechanical properties of cells are important in maintaining physiological functions of biological systems. Quantitative measurement and analysis of mechanical properties can help understand cellular mechanics and its functional relevance and discover physical biomarkers for diseases monitoring and therapeutics.

This dissertation presents a work to develop optical methods for studying cell mechanics which encompasses four applications. Surface plasmon resonance microscopy based optical method has been applied to image intracellular motions and cell mechanical motion. This label-free technique enables ultrafast imaging with extremely high sensitivity in detecting cell deformation. The technique was first applied to study intracellular transportation. Organelle transportation process and displacement steps of motor protein can be tracked using this method. The second application is to study heterogeneous subcellular membrane displacement induced by membrane potential (de)polarization. The application can map the amplitude and direction of cell deformation. The electromechanical coupling of mammalian cells was also observed. The third application is for imaging electrical activity in single cells with sub-millisecond resolution. This technique can fast record actions potentials and also resolve the fast initiation and propagation of electromechanical signals within single neurons. Bright-field optical imaging approach has been applied to the mechanical wave visualization that associated with action potential in the fourth application. Neuron-to-neuron viability of membrane displacement was revealed and heterogeneous subcellular response was observed.

All these works shed light on the possibility of using optical approaches to study millisecond-scale and sub-nanometer-scale mechanical motions. These studies revealed ultrafast and ultra-small mechanical motions at the cellular level, including motor protein-driven motions and electromechanical coupled motions. The observations will help understand cell mechanics and its biological functions. These optical approaches will also become powerful tools for elucidating the interplay between biological and physical functions.

To my beloved parents,

Xiazhen Qiu and Dazhong Yang

and my dear wife,

Jia Zeng

ACKNOWLEDGMENTS

I would like to express my sincere gratitude and appreciation to my advisor, Dr. Nongjian Tao, for his continued guidance, encouragement and support during my Ph.D. years. I am always astonished by his wealth of knowledge and extraordinary scientific scope, which inspires me to think and drives me to learn. From him, I see a great scientist, an inventor, an extraordinary leader, who makes his great devotion to the academia and innovation to the fields. Thanks for always keeping the office door open for discussion and providing me the freedom to explore.

I would like to especially thank my committee member, Dr. Shaopeng Wang, for his continued help and support during my Ph.D. He is always the first person to ask for when I have troubles in the lab. I am always amazed by his extraordinary technical commands and broad spectrum of knowledge, from which I learned a lot.

Many thanks to my committee members, Dr. Michael Goryll and Dr. Jennie Si, for valuable discussion of my projects from time to time. I greatly appreciate your insights and help.

I have been enjoying my time as one of the team members of the BB center. I would like to express my sincere gratefulness to Dr. Wei Wang for leading me into the SPR field and Dr. Xiaonan Shan for discussion and troubleshooting during my early Ph.D. years. My explicit thanks to Dr. Xianwei Liu, my close workmate, who contributes equally to most of the works I presented here. Many thanks to my peers, Dr. Yan Guan and Dr. Jin Lu, for informative discussions and feedback. I would like to express my appreciation to Dr. Hui Yu for his insightful thoughts and discussions on the projects. Many thanks to Dr. Linliang Yin, Karan Syal, Fenni Zhang and Yan Wang, who I am

working closely with and discussed a lot on the projects. Finally, I would like to express my sincere thanks to all SPR team members who make my Ph.D. experience colorful and unforgettable.

The works presented here would not be possible without the technical support of Dr. Jie Wu and Dr. Ming Gao from Barrow Neurological Institute and grant support from National Institute of Health (NIH) and Gordon and Betty Moore Foundation.

TABLE OF CONTENTS

Page

LIST OF FIGURES

Figure Page

CHAPTER 1 SIGNIFICANCE AND OBJECTIVE

Mechanical properties are intrinsic to all materials. Eukaryotic cells are one type of material that composed of soft matters and fluids(Bao and Suresh 2003). Each cell displays a unique mechanical signature(Moeendarbary and Harris 2014), which determines the behaviors of the cell in physiological conditions(Levental, Georges et al. 2007, Tyler 2012). Modulation of intracellular biomaterials, coupling them with other energy sources and their interaction with external mechanical stimuli will cause mechanical perturbations to cells(Janmey and McCulloch 2007). Such mechanical perturbation plays physiological roles in regulating the cell function, enabling a cross talk between mechanical and biochemical regulatory machinery(Pickup, Mouw et al. 2014). Many studies revealed that cell mechanical signature is highly correlated with disease development such as cancer progression(Lu, Weaver et al. 2012, Pickup, Mouw et al. 2014). Therefore, the mechanical signature can be potentially used for diagnosis and prognosis(Otto, Rosendahl et al. 2015). Biological response to the mechanical stimuli can also greatly determine the stem cell fate during differentiation(Guilak, Cohen et al. 2009).

Although many approaches have been developed for probing the mechanical properties, technology is still lacking for ultrafast imaging cell deformation. High speed imaging is critical for small objects because the speed of motion increases as the object size decreases. This also introduces technical difficulties, since signal from the motion becomes harder to detect as the size decreases. Traditional mechanical probing methods, such as AFM and optical tweezers(Bao and Suresh 2003), can provide accurate measurement; however, they are not capable of spatially mapping the mechanical strain and lack of measurement throughput.

Fast development in biotechnology in these decades provides valuable insights of the intrinsic regulatory machinery from genotypic level. However, a huge gap still exists between physical understanding of cell mechanics and its biological relevance. One barrier is that the mechanical property exists as a functional regulator only at the macroscopic level, which can be attributed to the population-level systematic behavior of cellular mechanics. Thus it is hard to study the interplay between mechanical force and its biological signaling, including force recognition, signal transduction, downstream amplification and the crosstalk between biochemical regulations. Lack of quantitative measurement in biology also limits the use of mechanical properties as physical biomarker for cell phenotyping.

My work is to develop optical methods for studying cell mechanics. In Chapter 2 and Chapter 3, I review the biological basis of cell mechanics and its properties as a whole cell. Chapter 3 also introduces biological significance of cell mechanics in disease development and other biological processes. Surface plasmon resonance microscopy based optical method has been applied to study intracellular motions and cell mechanical motion. This imaging method is label free and provides ultrafast imaging capability with extremely high sensitivity in detecting cell deformation. Chapter 4 demonstrates the application of surface plasmon resonance microscopy in studying intracellular transportation. I explored organelle transportation process using this imaging method and nanometer displacement step of motor protein was observed. Using this approach, I also observed a small membrane displacement induced by membrane potential (de)polarization (Chapter 5). The displacement is governed by the intrinsic mechanical property of the whole cell. The capability of tiny displacement probing on cell membrane

allows a direct imaging of action potential in neurons using this method (Chapter 6). Bright-field imaging was also employed for action potential imaging. Mechanical waves that accompany action potential were resolved (Chapter 7). I summarize the findings and discussed the future works in Chapter 8.

CHAPTER 2 BIOLOGICAL BASIS OF CELL MECHANICS

Biofilaments and Motor Proteins

Biofilaments

Eukaryotic cells can form a three-dimensional protein scaffold, named cytoskeleton(Fletcher and Mullins 2010). Cytoskeleton plays the most critical role in maintaining the shape of eukaryotic cells, interacting with external mechanical stimuli and is involved in multiple cellular processes, such as cell division and movement. The main components of cytoskeleton are three types of biofilaments: actin filaments, intermediate filaments and microtubules, all of which are protein polymers composed of hundreds of protein subunits.

Microfilaments and actins

Microfilaments or actin filaments are the thinnest protein polymer structure among all three types. Microfilaments are universally found in eukaryotic cells. They are critical in regulating cell motility and interacting with external forces. The building block of the microfilaments is the actin monomer, a 42-kD protein in cytoplasm, whose concentration is extremely high. These proteins either exist as monomers, known as G-actin (“G” for Globular), or dynamically form linear polymers, known as F-actin (“F” for filamentous). Each microfilament contains two interwined strands of subunits, whose thickness is about 6 nm.

Actin filaments are polarized. The fast-growing end is denoted as the plus (+) end. Actin monomers nucleate at this end with the help of ATP. The other end is called the minus (-) end. F-actin dissembles with the help of other depolymerization proteins. Typically, these microfilaments are formed at the edge of eukaryotic cells. The dynamic

treadmilling process generates or retracts the force at the cell edge and control the cell edge movement during cell migration. Many other proteins, such as Acting-Related Protein-2/3 (Arp2/3) complex, determine the microfilament nucleation and cross linking, which plays a significant role in forming 3D network structures. The mass per unit length of actin filaments is about 16kD/nm.

Intermediate filaments

Intermediate filaments are thicker than microfilaments. They are composed of a family of proteins sharing similar secondary structure and features. Multiple types of intermediate filaments can be found in the same cell. Some intermediate filaments, such as neurofilaments, are exclusively expressed in certain cell types. The common secondary structure of intermediate filament monomer is the central α-helical rod domain, which is composed of four α-helix segments. The N and C terminals vary among intermediate filament proteins. Two intermediate filament monomers dimerize in parallel and form a dimer. The center α-helical rod domains of both monomers align together and form coiled coil during dimerization. Dimer is the building block of the intermediate filament, whose diameter is about 10 nm on average. Many building blocks bundle together to form a rope-like higher structure.

Unlike microtubule and actin filaments, intermediate filament is non-polarized and does not involve treadmilling activity. However, intermediate filaments are still dynamic. The mass per unit length of intermediate filaments is about 35 kD/nm. This number varies depending on the filament type. The typical mass of neurofilaments is about 50 kD/nm per unit length.

Microtubules and tublins

Microtubule is the thickest biofilaments among all three types(Howard and Hyman 2003). It is composed of two types of tubulin proteins, α- and β- tubulin. Heterodimer of these two proteins form a unit of 8 nm in length. These units assemble as a long linear polymer end-to-end, which is called protofilaments. Typically, thirteen long protofilaments form a hollow cylinder, called a microtubule. The outer diameter of formed microtubule is about 25 nm, while the inner diameter is about 12 nm. The α β tubulin dimer has a molecular weight of about 100 kD. The overall molecular mass per unit length of a microtubule is about 160 kD/nm.

Similar to actin filaments, the microtubule is also polarized. The fast growing end is called the plus (+) end, which is terminated by the β-tubulin. The other end, the minus (-) end, is where the α-tubulin is exposed. In vivo, dimers nucleate at the plus end, while the minus end is generally anchored to the centrosome. Therefore, the plus end is typically dynamic. The conversion from growing to dissembling is called catastrophe, whereas the conversion from dissembling to synthesis is called rescue. Microtubules acts as tracks for motor proteins to transport organelles and cargos. They also provides solid support for maintaining the cell shape. Microtubules also participate in cell division and play important roles in regulating cell morphology.

Motor proteins

Molecular motors are one category of proteins that can generate motion or mechanical work. These motor proteins participate in many cellular processes. For example, F_0F_1ATP synthase, one type of motor protein, rotates and generates ATP based

on cross-membrane proton gradient. DNA polymerase, another motor protein, actively participates in DNA replication.

Motor proteins are one specific family of molecular motors that move along cytoskeleton biofilaments. These proteins are involved in processes such as active transport of proteins, vesicles and organelles, muscle contraction, chromosome separation during cell division, and other cell motility functions. Deficiencies of these motor proteins are related to multiple diseases and syndromes. Three types of motor proteins have been discovered: myosin, kinesin and dynein.

Actin motor – myosin

Myosin is a superfamily of proteins that walks along the actin filaments. Myosin consumes energy from ATP hydrolysis and generates mechanical force along with protein configuration change. The successive configuration change and interaction of myosin to the actin induces the mechanical motion along the track. Myosin is specifically involved in actin-guided motion. Myosin proteins can be divided into 18 family classes. The characteristic feature of myosin includes three functional domains. (a) The head domain: The head domain is the actin binding site. The binding affinity is regulated by ATP and ADP. Myosin uses the energy from ATP and generates motion on the actin. (b) The tail domain: The tail domain is the site which interacts with the cargo molecules or other myosin. This domain is critical in regulating transportation behaviors. (c) The neck domain: The neck domain acts as a linker between the tail domain and head domain. It works as lever arm that transduces the mechanical force at the interface of head domain and actin track to the tail domain.

Myosin superfamily can be also separated into conventional and unconventional families. Conventional family is the myosin II family, which is highly expressed in muscle cells and responsible for muscle contraction. These myosin motors contain two heavy chains and four light chains. Heavy chains constitute the coiled coil structure in neck domain. Four light chains (two for each heavy chain) bind to the heavy chains at the neck of head domain, which can regulate the function of muscle contraction. Unconventional myosin families include those involved in cargo transportation in cytoplasm. Among them, two families, myosin V and myosin VI, are the most studied. Myosin V consists a dimer with two heavy chains in coiled-coil structure. The two heads successively step along the actin filaments to the plus end of the filament with 37 nm in size. Myosin V also contains a calmodulin binding domain at the head. One light chain, LC8, binds to the tail of heavy chain of the myosin. It stabilizes the structure rather than binds to the cargos. Myosin VI is another unconventional family of proteins that is involved in transportation inside cells. However, it travels towards the minus end of the actin filaments.

Microtubule motors – kinesin and dynein

Two types of motor proteins are involved in microtubule guided transportation: kinesin and dynein. Kinesin motors move in the anterograde direction towards the plus end of microtubule (to the axon tip in neuron transportation); dynein motors move in the retrograde direction towards the minus end of microtubule (to the soma in neuron transportation).

Kinesin superfamily is composed of 14 protein families. Kinesin I family (KIF5) is the first discovered kinesin family *in vitro*. This protein family is also called

conventional kinesin, which is studied as a motor model for kinesin mechanics. The structure of kinesin I is similar to that of myosin mentioned earlier, which contains track-binding head domains, long-stalk neck domains and cargo-carrying tail domain. In vertebrates, conventional kinesin motor is composed of two heavy chains and two light chains. Two heavy chains bind as a dimer, forming a long coiled-coil stalk neck, two tail regions and two globular heads. Two light chains interact with the tail regions and regulate the selection and recognition of cargos. In fact, three heavy chain genes and three light chain genes in vertebrates are involved in this tetramer formation. These genes combine in various permutations and functionally regulate the specific cargo transportation. The head domain successively binds to tubulins and generates motion along the microtubule. Each step is about 8 nm in length, which is similar to the length of each α β tubulin unit.

Dynein is another superfamily of proteins involved in retrograde transportation on microtubules. Dynein is relatively less understood because it is difficult to express whole length dynein in other in vitro systems, due to its huge molecular weight. The structure of cytoplasmic dynein has been better studied. Each monomer dynein has a heavy chain, composing 6 AAA+ ATPase-like domains arranged as a ring. Four of the AAA+ domains play a role as the ATP hydrolysis site. The other two stabilize the structure. The heavy chain also forms small globular head domain, which mediates the binding to the tubulin structure. A coiled-coil structure is also involved in heavy chain structure, which facilitates the dimerization of two dynein as a functional unit. The neck and cargo-binding region of cytoplasmic dynein is relatively complicated. It also includes one light chain, LC8, which regulates the cargo binding. Dimeric cytoplasmic dynein also takes 8-

nm steps during movement. However, each individual motor domain of dynein dimer walks in a 16-nm-step manner. There are still debates on the dynamic pattern of cytoplasmic dynein motion.

Biomembranes and Membrane Proteins

Eukaryotic cells separate themselves from the environment solution by plasma membrane. Phospholipid bilayer, which contains many types of phospholipids, constitutes this physical barrier. Membrane proteins are embedded in this two-dimensional liquid layer. They form lipid rafts or domains and actively participate in transducing external signals into the cell. Interaction between plasma membrane and membrane protein is also important in mechanosensing and mechanical signal transductions.

Plasma membrane

Plasma membrane has several features. On one hand, it is dynamic and viscoelastic. It forms a two-dimensional semi-fluidic plain, with lateral diffusion coefficient in the order of 10-12 m^2/s. Phospholipids are involved in many dynamic motions such as trans-gauche isomerization, rotation, wobbling, as well as transmembrane flip-flop events.

On the other hand, phospholipid bilayer is a Maxwell material. It has both viscous and elastic components(Evans and Hochmuth 1978). Its tension and viscosity depends on frequency. The relaxation time is at the level of tens of microseconds. The susceptibility of deformation to the force can be quantified by different types of moduli, including those related to compressibility (volume, area and thickness change), rigidity (in-plain shear or extension) or curvature elasticity (surface bending). Compared with compression

modulus, bending modulus of membrane is much smaller, which means that lipid membrane is more sensitive to the bending deformation. This property allows cells to perform bending-like motions in a low energy-cost manner, such as exocytosis, endocytosis and cell morphological manipulation (protrusion or repulsion). In eukaryotic cells, the intrinsic viscoelastic properties are governed by the cytoskeleton mechanics, which will be discussed later.

Plasma membrane also serves as an electrical barrier for separating the inside of cells from the outside(Mosgaard, Zecchi et al. 2015). Bilayer of membrane can be electrically modelled as the combination of one parallel capacitor of lipid bilayer -Cm, and two layers of double layer capacitor - CD, at the interface of lipids to the solution in series. The capacitance of lipid bilayer is typically in the range of ~1 μF/cm2 for eukaryotic cells. Double layer capacitance can be quantified by $C_D = \epsilon_w \epsilon_0 / K_D$, where ϵ_w is relative permittivity of water, K_D is Debye length, which is quantified as $K_D = (\epsilon_w \epsilon_0 k_B T / 2z^2 {e_0}^2 n)^{1/2}$($k_B$, Boltzmann's constant; e_0, electron charge, ϵ_0, permittivity of free space, z, ion valence, n, ionic strength). In normal physiological condition, the double layer capacitance is much bigger than lipid bilayer capacitance. Therefore, most of the transmembrane potential drops on the lipid bilayer.

Membrane proteins

Membrane proteins are functional units that transduce extracellular signal into the cell and regulate the physiological functions. Membrane proteins compose of 20% of the type of proteins of a single cell.

Similar to other proteins, membrane proteins undergo a dynamic conformational change when they bind to different stimuli or during events such as ion channel

open/close and ion transportation of membrane transporters. Binding of extracellular signal will also induce down-stream mechanical motion of membrane proteins, such as protein dimerization in Receptor Tyrosine Kinase bindings and G-protein release in G-protein-coupled receptor (GPCR) signaling. The two-dimensional membrane supports mechanical movements of membrane proteins. This interface also enables cell unit function in communication and recognition with other cells, such as aligned connexins in electrical synapses and aligned pairs of receptors in immune synapse formation.

The interplay between membrane protein and cell plasma membrane also plays a significant role(Phillips, Ursell et al. 2009). Membrane protein can help shape the plasma membrane mechanics. One example is the clathrin-regulated membrane budding and SNAP (Soluble NSF Attachment Protein) Receptor (SNARE) induced membrane fusion(McMahon and Gallop 2005). The incorporation of membrane protein into the lipid bilayer also induces changes in local membrane curvature, thickness and elasticity. Lipid bilayer can actively regulate cellular functions as well. The mechanical stress of the plasma membrane regulates membrane protein functions. Mechanosensitive ion channels are an extensively-studied model found in many organisms(Peyronnet, Tran et al. 2014). Local membrane tension or membrane curvature will directly induce the configuration change of the mechanosensitive ion channel, which further affect the gating of ions transfer cross the membrane. Recently, a piezoelectric protein, Piezo family protein, was found in mammalian cells and play a role in tension sensing in mechanoreceptors. Although the molecular mechanism of channel gating is still obscure, it indicates that direct mechanical sensing is important for cells in physiological conditions.

Extracellular Matrix and Cell-substrate Interaction

Extracellular matrix (ECM)

In multicellular organisms, extracellular matrix (ECM) molecules act as a support for cells and transduce force from one cell to another. ECM is involved in multiple cellular processes in physiological condition, such as cell growth, differentiation, migration, and regulatory roles in cell-cell communications and cancer progression. The molecular constitution of ECM depends on the multicellular structures. The main components include proteoglycans, polysaccharide, protein fibers, and other functional proteins. On the opposite side of extracellular matrix – inside the cells - a transmembrane protein, integrin, is the receptor sensing the extracellular force. Many extracellular proteins, such as collagen, fibronectin and laminin, contain integrin-recognition sites (such as RGD motif). The recognition causes a direct binding of cell-surface integrin to the extracellular matrix and transduces mechanical force into the cytoskeleton inside the cell. The cell thereby sense the force, amplifies the force and triggers downstream responses. Therefore, integrin works not only as a connection between the inside cytoskeleton and the outside ECM, but also functionally serves as a force sensor for the cell.

Integrin and cell-substrate interaction

Integrin is a heterodimer composed of α and β subunits. Several subtypes of α and β subunits can combine and form heterodimers. Integrin plays significant roles in cell mechanotrasduction. Together with other adapter proteins, such as talin, vinculin and actinin, integrin can form focal adhesions, which are large protein clusters allowing cells to anchor to the surface. Inside the cells, actin filaments connect to integrins and provide

the motion force. The focal adhesions dynamically assemble and disassemble, allowing cells to migrate on the surface with the support of the substrate.

Dynamic interaction between cell and substrate allows the cell to migrate on the surface. The crawling process is also called cell locomotion. A simple mechanical model has been proposed in describing the process. The cell firstly protrudes at the leading edge through actin filament synthesis. The tip of the leading end finds the new location and forms the new focal adhesion. The posterior part of the cell detaches and old focal adhesions at the posterior part dissemble. Via this dynamic process, the cell migrates to a new location.

CHAPTER 3 MECHANICS OF THE CELL AND MECHANICAL CELL BIOLOGY

The Whole Cell – Soft Materials and Fluids

The composition of an individual cell is extremely complicated. A cell contains soft materials and fluids with a variety of compositions. The mechanics of a whole cell is mainly determined by the viscoelastic property of the cytoskeleton structure(Pourati, Maniotis et al. 1998). The cytoskeleton scaffold forms a three-dimensional network wrapped by the plasma membrane. This structure shapes the eukaryotic cell and determines the mechanical properties. The mechanics of cytoskeleton have been characterized by several methods(Trepat, Lenormand et al. 2008, Hoffman and Crocker 2009). The findings show that cytoskeleton mechanics of all cell types share several properties.

Power law relation of cell rheology

Dynamic mechanical analysis using methods such as optical magnetic twisting cytometry (OMTC), atomic force microscopy (AFM) and optical tweezers indicates that the storage modulus (G') of the cell has a weak power-law relationship with the frequency, that is $G'(f) \propto f^{\alpha}$, where α is in the range of 0.1-0.2. This relationship spans the spectrum range from 0.01 Hz to 1kHz. The loss modulus (G'') of the cell follows a similar power law below frequency ~30 Hz. The dynamic modulus is given by $G^*(f) = G' + iG''$. The ratio of the loss modulus and storage modulus, known as hysteresivity, $\eta = G''/G'$, remains constant between 0.2 and 0.4 below 30 Hz. This indicates that below 30 Hz, the cell is mainly elastic. G'' shows a much higher power coefficient above 30 Hz, and starts to dominate over storage modulus above hundreds of Hertz. This suggests that at a high frequency range, the viscous property of the cell becomes dominant.

Subdiffusive and superdiffusive motion of particle

Quantification of particle motions inside cells or embedded in the cytoskeleton can provide valuable information on cell mechanical properties. To quantify the motion, mean square displacement (MSD) of the particle vs. various time intervals Δt is calculated. Their relation is $MSD = D\Delta t^{\beta}$, where β is the power coefficient. For particles undergoing pure Brownian motion, $\beta = 1$, which means the impulsive forces are randomly applied and the direction of the next step and the previous step are uncorrelated. $\beta > 1$ indicates that the forces in time series has positive correlation, which means the next step is likely to be in the same direction as the previous step. This regime is also called superdiffusive region. For the $\beta < 1$ case, the correlation is in the opposite way, which means that the next step is likely to be in the opposite direction from the previous step. This is also called subdiffusive. Particles inside cells or attached to the cytoskeleton have a typical $\beta = 0.2$ for time interval below 1 s and a $\beta = 1.6$ for large Δt. The transition of $\beta = 1$ is in the order of 1 s. This analysis demonstrates the complexity of the motions inside cells.

Cell Mechanics and Biological Functions

Cell mechanics and oncology

The ability of cancer cells to migrate is important for cancer metastasis(Wirtz, Konstantopoulos et al. 2011). Cell migration is involved in several processes of metastasis, from leaving the primary tumor to the localizing in the secondary tumor. A tumor cell first detaches from the primary tumor. It migrates to the blood vessels via attaching to the basal membrane and intravasating into the blood. It then circulates in the blood system as circulating tumor cell (CTC). After that, the cell attaches to blood vessel

wall again and extravasates to a new location. Finally it grows into a secondary tumor. During these processes, the mechanical property of the cell and its interaction with extracellular environment determines the ability of cell migration. The capability of cancer cell to squeeze into the blood vessel by crossing the basal membrane is also related to the cell deformation capability. Typically, mechanical probing measurement shows that a tumor cell is softer than a normal cell(Cross, Jin et al. 2007, Plodinec, Loparic et al. 2012).

Cancer cells at different stages of progression may have different mechanical properties. Cell mechanics have potential to become biomarkers for cancer diagnosis and stratification. Therefore, the intrinsic mechanical signature of cells can also be used as phenotypic readout of cancer progression. High-throughput mechanical probing methods, such as deformability cytometry, have been developed to identify tumor populations(Darling and Di Carlo 2015, Otto, Rosendahl et al. 2015). Another application is external manipulation of cell mechanics. Modulating the extracellular mechanical environment and targeting the intracellular mechanical-related machinery are both helpful in controlling the metastasis capability. By targeting myosin, researchers have developed an alternative approach to cancer treatment to suppress metastasis(Surcel, Ng et al. 2015).

Cell mechanics and stem cells

Extensive studies have revealed that external mechanical stimuli can regulate the fate of stem cells, such as muscle satellite cells and hematopoietic stem cells. Stem cells can remember mechanical cues, for instance, the stiffness, from the extracellular matrix(Yang, Tibbitt et al. 2014). These physical properties can influence the localization

of transcription factors, regulate gene expressions and affect the lineage commitment of stem cells(Yang, Tibbitt et al. 2014). Mechanical environment can also regulate cell reprogramming(Downing, Soto et al. 2013, Caiazzo, Okawa et al. 2016).

CHAPTER 4 LABEL-FREE TRACKING OF SINGLE ORGANELLE TRANSPORTATION IN CELLS WITH NANOMETER PRECISION USING A PLASMONIC IMAGING TECHNIQUE

Imaging and tracking of nano- and micrometer-sized organelles in cells with nanometer precision is crucial for understanding cellular behaviors at the molecular scale. Because of the fast intracellular dynamic processes, the imaging and tracking method must also be fast. In addition, to ensure that the observed dynamics is relevant to the native functions, it is critical to keep the cells under their native states. Here, a plasmonics-based imaging technique is demonstrated for studying the dynamics of organelles in 3D with high localization precision (5 nm) and temporal (10 ms) resolution. The technique is label-free and can track subcellular structures in the native state of the cells. Using the technique, nanometer steps of organelle (e.g., mitochondria) transportation are observed along neurite microtubules in primary neurons, and the 3D structure of neurite microtubule bundles is reconstructed at the nanometer scale from the tracks of the moving organelles.

Introduction

Imaging and tracking fast intracellular dynamic processes with nanometer precision is critical to understand the underlying molecular processes of many biological phenomena, including cell growth, mass transportation, signaling transduction and cell migration(Hirokawa and Takemura 2005). Myriad intracellular events are well orchestrated at the molecular level within the tiny volume of a single cell. Aberrant regulations cause various developmental and neurodegenerative diseases(De Vos, Grierson et al. 2008, Sheng and Cai 2012). Despite the great need, tracking the intracellular dynamics remains a difficult challenge. A technique for this task requires high spatial localization accuracy and temporal resolution. It should also be non-invasive in order to minimize perturbations to the native dynamic processes under study. To date, the most popular method is fluorescence imaging techniques(Yildiz, Forkey et al. 2003, Huang, Wang et al. 2008, Huang, Bates et al. 2009, Patterson, Davidson et al. 2010, Schindler, Chen et al. 2014). Although powerful, fluorescence emission is relatively weak, which requires time to collect sufficient photons, thus limiting the imaging speed. Moreover, labeling of living systems with fluorescent tags may disturb their native cellular processes and affect the original physiological functions.

To overcome these drawbacks, label-free imaging techniques have been employed for imaging and tracking. Previous studies on unstained lipid droplet demonstrated a nonperturbative tracking strategy using coherent anti-Stokes Raman scattering (CARS) microscopy and stimulated Raman scattering (SRS) microscopy(Nan, Potma et al. 2006, Dou, Zhang et al. 2012). Other nonlinear optical techniques, such as second harmonic generation (SHG) microscopy and third harmonic generation (THG) microscopy, have

also been applied for studying dynamic trafficking of lipid bodies(Debarre, Supatto et al. 2006). By combining with multi-photon excited native fluorescence, these multimodal methods showed a powerful imaging capability of studying intrinsic metabolic signals in tissue(Zipfel, Williams et al. 2003). However, the imaging rates of these techniques are limited for studying fast dynamic processes.(Jungst, Winterhalder et al. 2011)

Surface plasmon resonance (SPR) is a surface sensing technique widely used in life sciences and pharmaceutical discovery. The extremely high sensitivity to mass density changes on the surface makes SPR an indispensable technique in assessing protein-protein interaction and studying binding kinetics. Recently, SPR microscopy has been demonstrated in the total internal reflection (TIR) configuration(Huang, Yu et al. 2007). This plasmonics-based microscopy technique provides superior spatial resolution, allowing for studying protein binding kinetics(Wang, Yang et al. 2012). However, tracking of subcellular organelles with high spatial and temporal resolution has not been shown previously.

Here, I demonstrate tracking of single organelle dynamics in cells with this plasmonics-based imaging technique(Huang, Yu et al. 2007, Wang, Shan et al. 2010, Shan, Díez-Pérez et al. 2012, Wang, Yang et al. 2012). The technique excites surface plasmonic waves on a gold surface with light, and the presence of an organelle on or near the surface scatters the plasmonic waves (Figure 4-3 a), leading to a high contrast image of the organelle without labels. By analyzing the high contrast plasmonic images over time, I have tracked intracellular dynamics in three dimensions with nanometer localization precision and millisecond temporal resolution, and observed stepwise movement of the organelles (mitochondria) that are originated from the motor proteins.

Materials and Methods

Cell culture and fluorescence staining

Primary rat hippocampus neurons (Life Technologies, Carlsbad, CA, USA) were recovered from cryopreservation and seeded on poly-L-lysine (Trevigen, Gaithersburg, MD, USA) coated sensor chip surface at ~10^5 cells/cm^2. After incubation in a humidified atmosphere with 5% CO_2 at 37°C for 4~8 days, cells attached to the surface and were ready for experiment. Neurons were cultured in neurobasal medium (Life Technologies, Carlsbad, CA, USA) with B-27® supplement (Life Technologies, Carlsbad, CA, USA) and GlutaMAX™ (Life Technologies, Carlsbad, CA, USA). Mitochondria were stained with MitoTracker® Orange CMTMRos (Life Technologies, Carlsbad, CA, USA) for observations.

Plasmonic imaging

An inverted microscope (X81, Olympus, Shinjuku, Tokyo, Japan) with total internal reflection (TIR) configuration illumination was implemented in the plasmonic imaging system. P-polarized light beam (~5 mW) from a 680 nm fiber-coupled superluminescent diode (SLD) (Qphotonics LLC, Ann Arber, MI, USA) was introduced into the microscope via a TIR fluorescence tube lens (TIRF module, Olympus, Shinjuku, Tokyo, Japan) and a 50/50 beam splitter (Thorlabs, Newton, New Jersey, USA). The reflected light from the gold surface was detected by a CMOS camera (ORCA-Flash 4.0, Hamamatsu Photonics, Hamamatsu, Japan) with 4M pixels and a pixel size of 6.5 μm. A total of 160 x optical zoom was achieved by using a high numeric aperture 100 x objective combined with a 1.6 x magnification changer. Sensor chips were prepared by coating BK-7 glass coverslips with a ~1.5 nm chromium layer and the followed with a

~47 nm gold layer. To remove contaminations, each chip was rinsed with deionized water and ethanol followed by hydrogen-flame annealing. Before cell seeding, gold surface was modified with poly-L-lysine (5 μg/ml) solution for ~1 hour in a Flexi-Perm (Sarstedt, Newton, NC, USA) cell culture chamber attached on chip surface. For intracellular organelle observation, full resolution (2048 x 2048 px) image sequences at a video rate (25 fps) or a fast rate (100 fps) were either recorded in the computer memory and then saved to disk, or directly streamed into a solid-state drive (SSD) array.

Organelle localization and tracking

A custom MATLAB (Natick, MA, USA) program was used to accurately localize the mass centroid of the organelle. 2-D Gaussian function was employed for precise positioning throughout the whole image sequences. Before fitting, images were spatially filtered with 7 x 7 pixel average kernel. Local plasmonic intensity was obtained by calculating the mean value of the center 13 x 17 pixel region.

Organelle step analysis

When a target organelle moved laterally during the recording, a negative intensity region appeared after the first frame was subtracted from the whole image sequences. This region was used as a reference to evaluate the system noise and control the quality of stepping analysis in each case. To analyze the stepwise organelle movements, the signal drift was corrected by low-pass filtering of the recorded images in the reference area. Corrected x-y trajectory was then aligned along the principal axis of motion. On-axis (along the principal axis of motion) and off-axis (perpendicular to the principal axis of motion) components were assigned to the trajectory. The direction of the principal axis was determined by minimizing the off-axis distance variation over the entire trace.

For step detection, a step-finding algorithm developed by Drs. Jacob Kerssemakers and Marileen Dogterom was employed to analyze the on-axis component(Kerssemakers, Munteanu et al. 2006). This algorithm is accomplished by least-square fitting using a series of amplitude-undetermined steps. High ratio of χ^2_{fit} and $\chi^2_{\text{counter-fit}}$ indicated the real steps in the trajectory. To unbiasedly analyze the step size, I applied Chung-Kennedy filtering procedure to single on-axis trajectory(Chung and Kennedy 1991). This filter uses forward and backward moving average algorithm to preserve the step feature while removing noise. This algorithm has been widely used to reduce noise for quantitative analysis of biological events(Nan, Sims et al. 2005, Qiu, Derr et al. 2012). Pair-wised histogram of filtered trace was further implemented for statistical analysis and step size identification. For every trajectory, a reference region was fitted with 2D Gaussian function, and long-term drift was corrected in order to characterize the positioning inaccuracy due to the system noise over time.

Microtubule 3D structure mapping

Sequential x-y trajectories of organelle were translated into net displacement by pixelated distance calculation according to their common tracks. Intensity and position were determined by Gaussian fitting along the displacement trajectory. Height of the microtubule bundle can be calculated from the plasmonic image intensity.

Z-Axis Displacement Calculation and Localization Accuracy Evaluation

Z-axis displacement was calculated from local intensity change and calibrated decay constant of plasmonic intensity. Intensity profile along z-axis can be expressed as exponential decay equation: $I_{\Delta z} = I_0 \exp\frac{\Delta z}{\lambda}$, where I_0 is the intensity of reference point, Δz is the relative height change along z-axis of reference point, $I_{\Delta z}$ is the intensity value

at height Δz, λ is the decay constant. I calibrated the decay constant using different thickness of CYTOP coating surface with particles on top (Figure 4-1). A decay constant of 95.8 nm was achieved. Based on the local plasmonic intensity and calibrated decay constant, I can extract the relative height information Δz based on the equation. In Figure 4-9d, the maximum intensity point was used as reference for Δz calculation. To evaluate the z-axis localization accuracy, I mapped the intensity variations into displacement by the same procedure as described above. Generally, for each individual trajectory, a variation of 100 intensity unit (a.u.) was achieved (Figure 4-9c and Figure 4-7d as typical trajectories). After translating the intensity into z-axis displacement, I estimated a

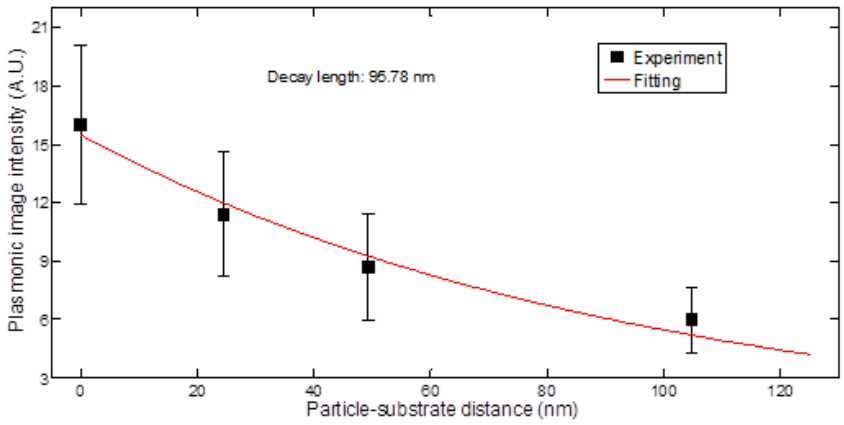

Figure 4-1 Decay Length Calibration Using CYTOP Coating

Plasmonic intensity profile with different particle-substrate distance. Nanometer z-axis displacement was controlled by thin film coating of CYTOP (refractive index: 1.34) with different thickness. Red curve shows the fitting result using exponential decay function with decay constant of 95.8 nm.

localization accuracy of ~5 nm in the z-direction.

Evaluation of Localization Accuracy in X and Y-Directions

The shadow region was used for evaluating of localization accuracy (Figure 4-2a). The localization accuracy was determined by 2D Gaussian fitting of this negative region over whole video clip. Figure 4-2b shows the control region fitting of the trajectory of Figure 4-8over 10 s. Standard deviation of 6.1 nm in x direction and 4.3 nm in y direction was observed in this case. Generally, a standard deviation of about 5 nm was achieved in

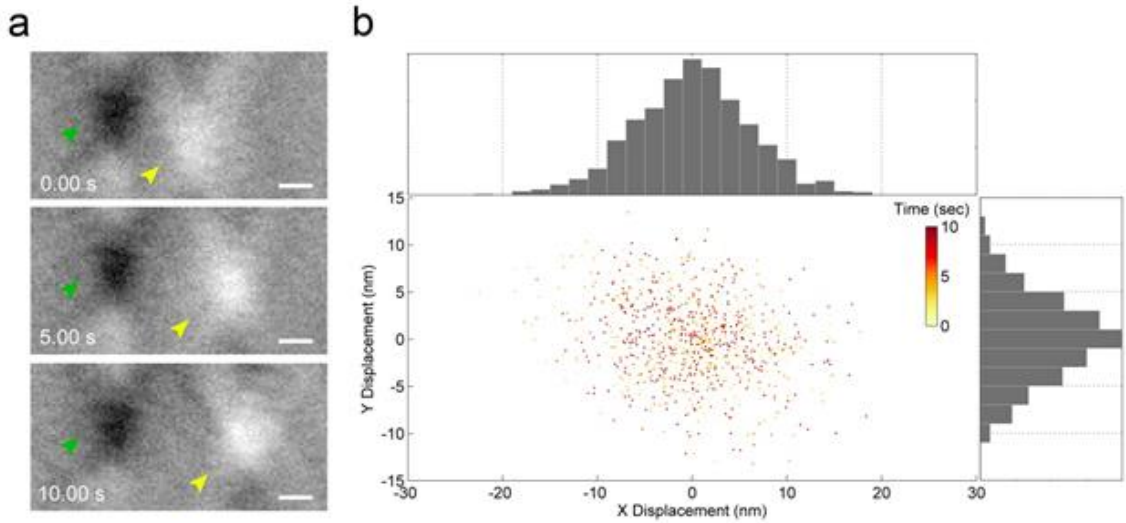

Figure 4-2 Negative Control Region and Tracking Accuracy Identification
(a) Time-lapse plasmonic images of moving organelle after first frame subtraction. Yellow arrow indicates the moving organelle over time. Green arrow indicates the negative shadow region, which is formed after organelle leave. (b) Fitting position in negative control region over time. Histograms show the distribution of fitting position in x and y direction. Scale bar: (a) 500 nm.

both x and y directions of this plasmonic tracking method. The noise levels on both directions are comparable.

Data analysis

All data analysis were carried out by using custom-written MATLAB scripts and/or Image J (Schneider, Rasband et al. 2012). Multiple Kymograph Image J plugin was used in moving organelle visualization.

Results and Discussion

Plasmonic imaging of intracellular organelle dynamics in live cell

Figure 4-3b and c show a bright field and corresponding plasmonic images of a live cell. Compared to the traditional bright field image (b), the plasmonic image (c) shows a much higher image contrast. This high contrast imaging capability allows for tracking of individual organelles inside a cell. In order to focus on the dynamics of the organelles, I subtract the first frame from the subsequent frames. The time-differential images reveal only moving organelles, and thus suppressing non-moving objects in the. Figure 4-3d is such a differential image, which shows several bright spots as marked by white arrows. Zooming-in of a lower left region of the image reveals more clearly the bright spots, each with a "V" shape tail along the propagation direction of the surface plasmonic wave (Figure 4-3e). The tail is due to the scattering of the surface plasmonic wave by the organelles, which also shows up in the plasmonic images of nanoparticles as reported previously by our group (Shan, Diez-Perez et al. 2012).

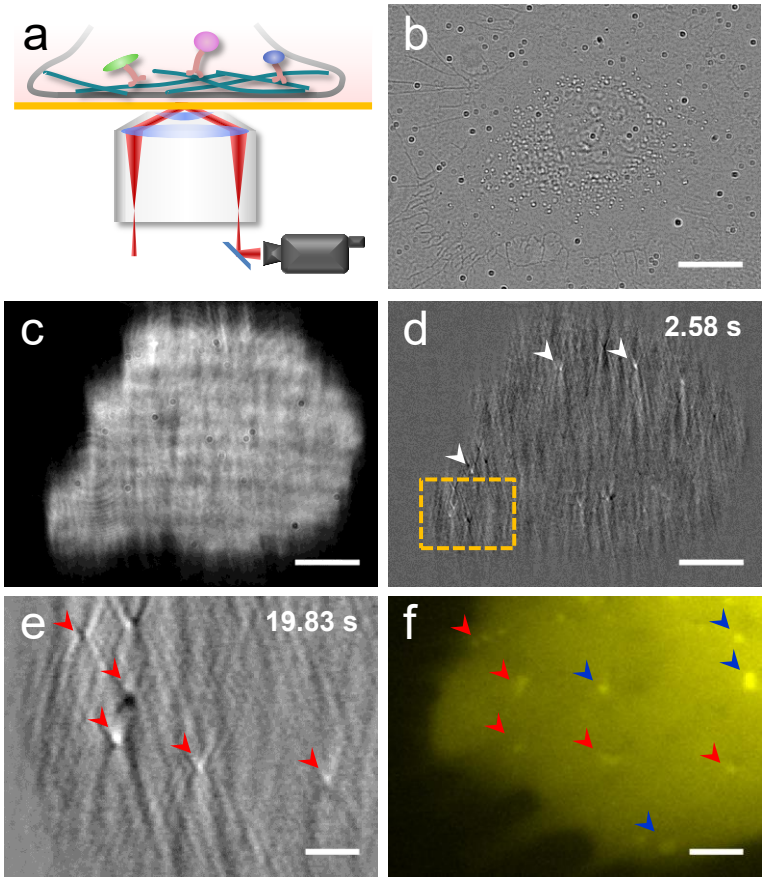

Figure 4-3 Plasmonic Imaging of Intracellular Organelle Dynamics in Live Cell. (a) Schematic diagram of plasmonic imaging setup for imaging intracellular processes. (b, c) Transmitted (b) and plasmonic (c) images of single SH-EP1 cell. (d) A representative image of intracellular organelles after subtracting the first frame, where the white arrows indicate the intracellular organelles. (e, f) Zoom-in images of another plasmonic image after subtracting the first frame (e) and epi-fluorescence (f) labeled with MitoTracker® in region marked by orange boxes in (d). Red arrows indicate common features of plasmonic images and fluorescence. Blue arrows indicate fluorescence-only features. Note the blurry of the fluorescence image of (f) is affected by the gold film. Scale bar: (b-d) 25 μm; (e, f) 5 μm.

To identify the organelles, I stained the cell with a fluorescent dye, MitoTracker®, which targets at mitochondria. Figure 4-3f is a fluorescent image of the same region as the time-differential plasmonic image shown in Figure 4-3e. The

organelles revealed in the plasmonic image match well with those in the fluorescent image (Figure 4-4), which indicates that the features tracked by the plasmonic imaging technique are mitochondria. However, some mitochondria in the fluorescent image do not show up in the plasmonic image, which is probably due to that they are located outside of

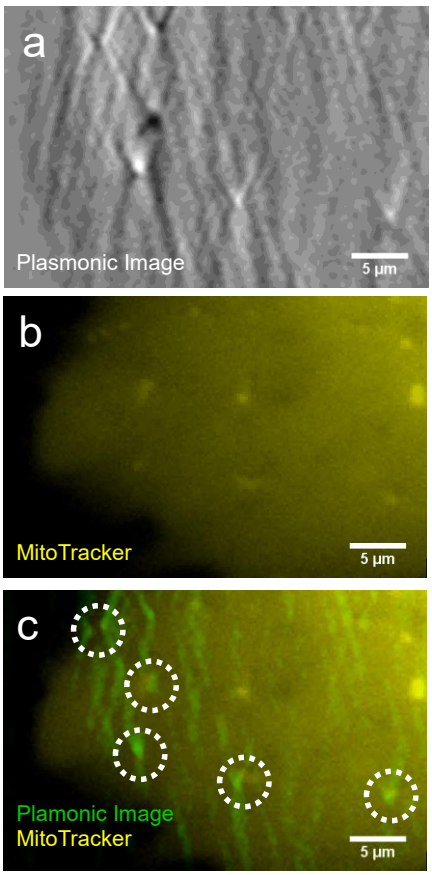

Figure 4-4 Overlay of Plasmonic and Fluorescent Images
(a) Differential plasmonic image of moving mitochondria. (b) Fluorescent image of mitochondria stained with MitoTracker. (c) Overly of plasmonic and fluorescent images. White circle shows the overlayed features in both plasmonic and fluorescent images. Scale bar: (a-c) 5 μm

the evanescent field associated with the plasmonic waves. In addition to dot-like mitochondria, I also observed elongated ones. Figure 4-6 shows two mitochondria sliding on the same track, each has a length of ~1.5 μm. Since mitochondria are the largest and

most abundant organelles in cell, I expected most of the features revealed in plasmonic image are from mitochondria.

Mitochondria are essential organelles responsible for energy production and many

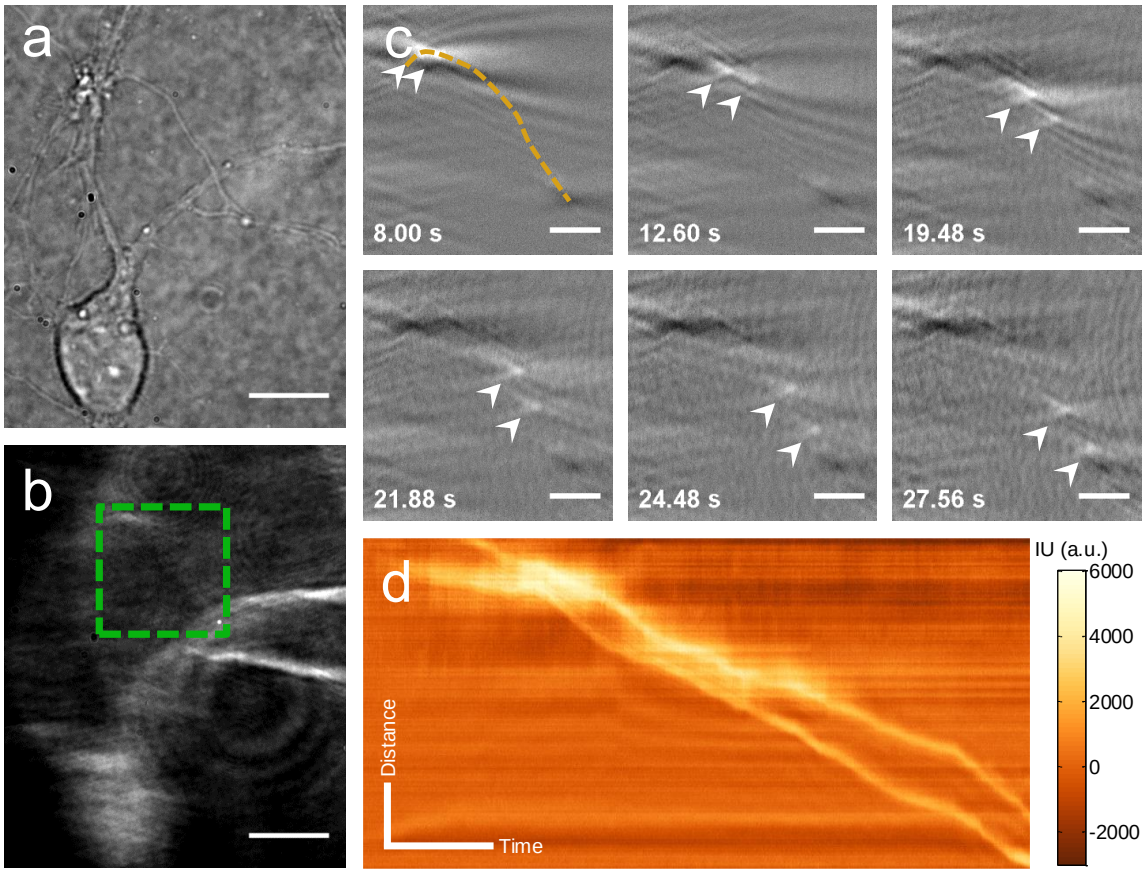

Figure 4-5 Plasmonic Tracking of Intracellular Organelle Dynamics in Live Cell. Transmitted **(a)** and plasmonic **(b)** images of primary hippocampus neuron obtained by the plasmonic imaging system. **(c)** Snapshots of plasmonic images of the movement of two intracellular organelles along the neurite structure (marked as dashed line) in region marked by a dashed box in (b). **(d)** Kymograph of two organelles in (c). Scale bar: (a), (b), 10 μm; (c) 3 μm; (d) Distance: 3 μm; Time: 5 s.

other cellular processes, including cell apoptosis and aging(Chan 2006, Lin and Beal 2006). Their trafficking and distribution are critical for local energy supply in distal structures, such as axons and dendrites in neurons. Various neurodegenerative diseases are related to inappropriate mitochondrial trafficking(De Vos, Grierson et al. 2008, Chen

and Chan 2009). Plasmonic imaging provides a label-free approach to study mitochondria in native state, eliminating complications with dye-labeling process, which could hinder the respiratory function of mitochondria. To explore the long-range axonal transport, I studied the organelle dynamics in primary neurons. The plasmonic imaging of the neurons has superior image contrast, compared to the traditional bright field optical images, allowing me to resolve clearly minor structures, such as axons and dendrites (Figure 4-5a and Figure 4-5b). It also allows me to observe confined organelle transportation in the neurite structure. Figure 4-5c shows several snapshots of the time-differential plasmonic images of two organelles marked with arrows moving from upper left towards the lower right of the frame. The moving tracks of the two organelles (the yellow dashed line in Figure 4-5c) follow well the neurite structure as shown in the plasmonic image marked by a dashed square box in Figure 4-5b. The dynamics of the two organelles moving along the neurite structure is described by plotting the distance vs. time, or known as kymographs in Figure 4-5d. The kymographs provide detailed information about the motion of the organelles. For example, the local slope is the velocity of the moving organelle. These examples demonstrate a label-free imaging of single organelle dynamics in cells.

Observation of organelle stepping by fast tracking

I show below that it is also possible to accurately track the movement of the organelles with the plasmonic imaging capability. As shown in Figure 4-3e, the plasmonic image of an organelle displays a V-shape diffraction pattern with a bright spot at the apex of the "V" (Figure 4-7a,b). The bright spot reflects the center of mass of the organelle. By fitting the bright spot with a 2D Gaussian distribution function, I located the position of the organelle, and tracked its transportation by following the position over

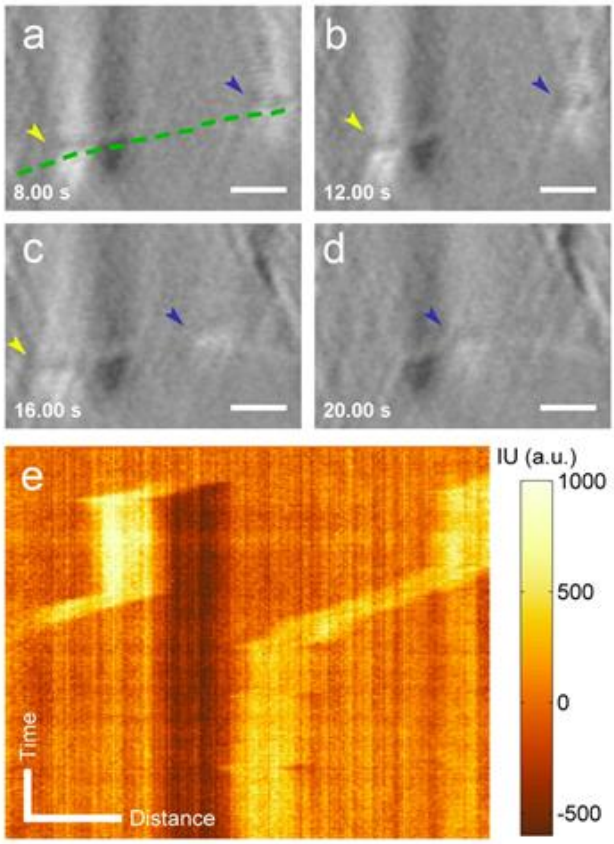

Figure 4-6 Elongated Mitochondria

(a-d) Plasmonic images of two elongated mitochondria moving along the same track over time. Yellow arrow indicates the first mitochondrion. Blue arrow indicates the second mitochondrion. (e) Kymograph of these two mitochondria on track showing as dashed green line in (a). Scale bar: (a-d) 2 μm (e) Distance: 2 μm; Time: 5 s.

time (Figure 4-7c,d).

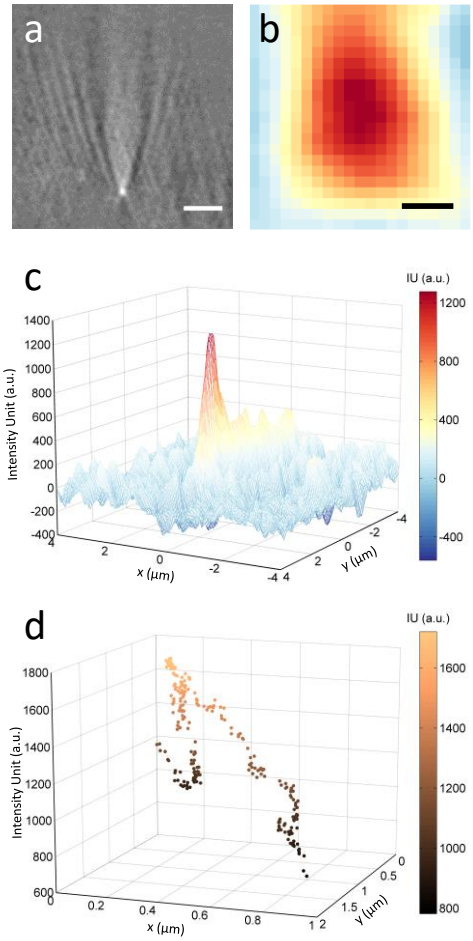

Figure 4-7 Fast Tracking Intracellular Organelle by 2D Gaussian Fitting.
(a) A typical plasmonic image of individual organelle. (b) Center region of the organelle in (a). (c) 3D plot of plasmonic intensity of organelle in (a). (d) A represented trace of one organelle movement after tracking by 2D Gaussian fitting. Scale bar: (a) 3 μm; (b) 200 nm.

Recent studies have revealed that motor proteins move along their tracks in a stepwise manner by alternating their track-binding motor domain(Vale 2003, Yildiz, Forkey et al. 2003, Yildiz, Tomishige et al. 2004, Kural, Kim et al. 2005, Nan, Sims et al. 2005, Nan, Potma et al. 2006, Cui, Wu et al. 2007, Nan, Sims et al. 2008, Sims and Xie 2009, DeWitt, Chang et al. 2012, Gu, Sun et al. 2012). This microtubule-depended motion is a universal model for organelle transporting, including mitochondria, lipid

droplets, endosomes, and lysosomes. Most of these previous works are based on labeling the motor proteins or organelles with fluorescent tags, which may disturb the native behavior of the motor proteins. In fact, evidence has shown that changing in the load of the motor proteins may alter the stepping sizes(Mallik, Carter et al. 2004), which underscores the importance of non-invasive and label-free plasmonic imaging and tracking of organelle transportation. Additionally, plasmonic imaging intensity is rather bright, compared to fluorescent imaging, making it possible to track fast movement of organelles.

To track the fast organelle transportation dynamics, I recorded moving organelles in neurites using a frame rate up to 100 frames per second. Faster frame rates are also

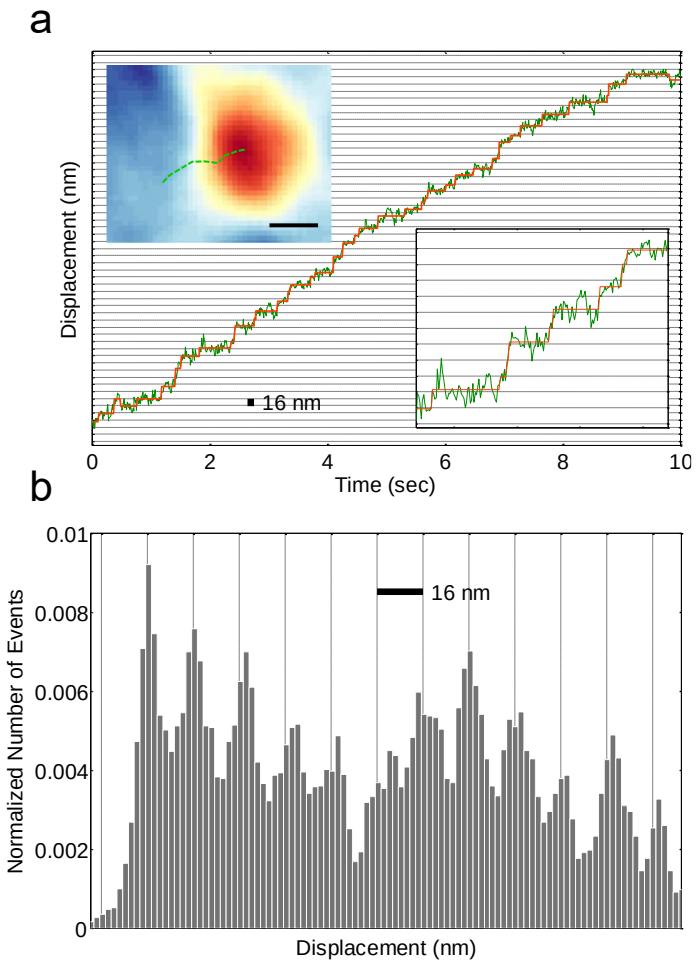

Figure 4-8 Stepping Observation of Single Organelle.

(a) Green line: the trajectory of an organelle moving in cell over time. Red line: fitting of the trajectory with a stepwise function. Upper left inset: Trajectory of a moving organelle in x-y plane. Bottom right: zoom in of the trajectory between time 1.7 s and 3 s. (b) Pair-wised histogram of organelle displacement, showing discrete peaks with a separation of 16 nm. Scale bar: (a) Space between two horizontal grid line: 16 nm. Top inset: 400 nm (b) space between two vertical line: 16 nm.

possible because the plasmonic imaging measures the scattering of the plasmonic waves by the organelles, which is sufficiently strong and can be detected with a fast camera.

Figure 4-8a shows the displacement of an organelle determined with the plasmonic tracking method over time. Stepwise changes in the displacement with a step size of ~16 nm can be identified (inset of lower right of Figure 4-8a). This step size is consistent with previous reports for microtubule-based movement of dynein(Mallik, Carter et al. 2004, Nan, Sims et al. 2005, Rai, Rai et al. 2013). Pair-wise statistical analysis of the displacement reveal pronounced peaks separated with 16 nm intervals, which further confirms the stepwise transportation of the organelles observed here (Figure 4-8b). Note that both 8 nm and 16 nm step sizes have been reported in kinesin and dynein driven motion(Yildiz, Tomishige et al. 2004, Reck-Peterson, Yildiz et al. 2006). The absence of the 8 nm-steps in the present work might be due to the complexity of organelle behavior in native environment.

In addition to accurate tracking of the organelle displacement laterally (x-y or the image plane), the plasmonic imaging technique can track the organelle displacement vertically (z-direction). This is because the evanescent field associated with the surface plasmonic waves decays exponentially from the surface into the solution phase, and consequently, the plasmonic imaging intensity is also an exponential function of the vertical position (z displacement) of the organelle. I experimentally verified the z-axis decay constant by measuring the imaging intensity of small particles placed at various distances from the gold surface (Figure 4-1). The measured decay constant (95.8 nm) is consistent with simulation result using multiple layer model.(Shan, Huang et al. 2009, Shan, Wang et al. 2010, Shan, Fang et al. 2014) From the measured plasmonic imaging intensity change, and the decay constant, I was able to determine the z component of the displacement with high accuracy. The capability of accurate tracking in z direction is not

available for the conventional fluorescence-based imaging method, which makes the present plasmonic tracking method unique for studying the dynamics of subcellular organelles in 3D.

Three-dimensional mapping of microtubule bundle

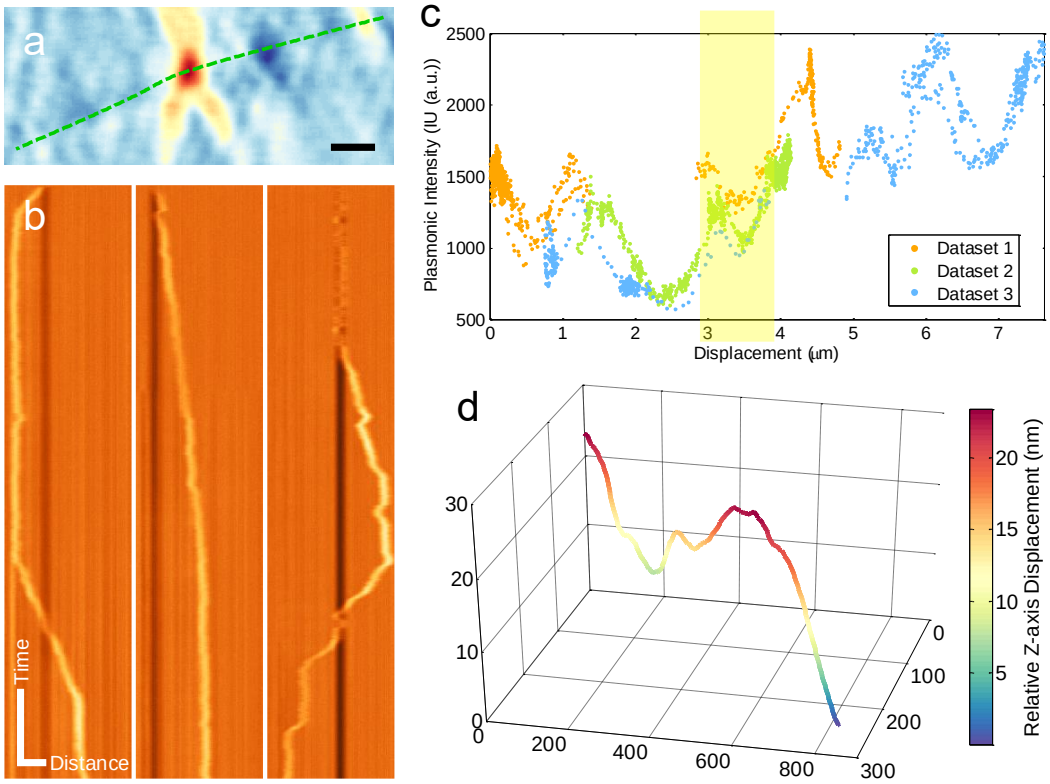

Figure 4-9 3D Mapping of Microtubule Structure by Single Organelle Tracking. (a) Trajectory of moving organelle in x-y plane. (b) Kymograph of three different runs of the same organelle. Vertical direction: time. Horizontal direction: distance. (c) Plasmonic image intensity variation of an organelle along its track. (d) 3D structure of microtubule bundle of the region highlighted with yellow shade in (c). Scale bar: (a) 1 μm (b) Time: 5 s; Distance: 2 μm.

To obtain structural information of microtubules, I monitored the movement of single organelles back and forth along a section of a neurite fiber (Figure 4-9a). Kymographs of three different recordings are plotted in Figure 4-9b, which show different movements of the organelle along the same microtubule. The plasmonic

imaging intensity of the organelle is plotted against the net displacement along the neurite fiber in Figure 4-9c, which reveals a large variation of the intensity along the fiber. The patterns of the intensity variation for repeated recordings of the organelle moving back and forth along the fiber are similar, which indicates that the plasmonic intensity depends mainly on the location along the fiber. I thus believe that the observed variation in the plasmonic imaging intensity of the organelle was due to the local variation in the distance between the microtubule and the surface. This z-position information, along with the x and y positions, allowed me to extract the 3D structure of the microtubule from the plasmonic images. Figure 4-9d shows the extracted 3D structure of a section of microtubule bundle.

I evaluated the accuracy of displacement tracking in x-y directions by Gaussian fitting of the negative shadow region. The standard deviation in x-y direction is about 5 nm (Figure 4-2), which is sufficient for resolving a 16 nm step of the motor proteins. To further validate the observation of the 16 nm step in the pair-wise histogram analysis and eliminate the possible artificial measurement errors, I performed same analysis procedure to a step-exclusive ramp signal with similar noise. I did not observe obvious steps (Figure 4-10). The accuracy of displacement tracking z-direction was determined from the plasmonic imaging intensity noise, which corresponds to an accuracy of ~ 5nm. Noise from camera and light source limited the tracking accuracy. It can be fundamentally improved by using ultrafast camera with high-power light source and averaging over frames. The temporal resolution of present study is 10 ms, limited by the frame rate of the camera used in the experiment. This temporal resolution compares favorably with the

fluorescence-based method, and much faster frame-camera could be used to acquire plasmonic images, which would allow for even faster tracking speed.

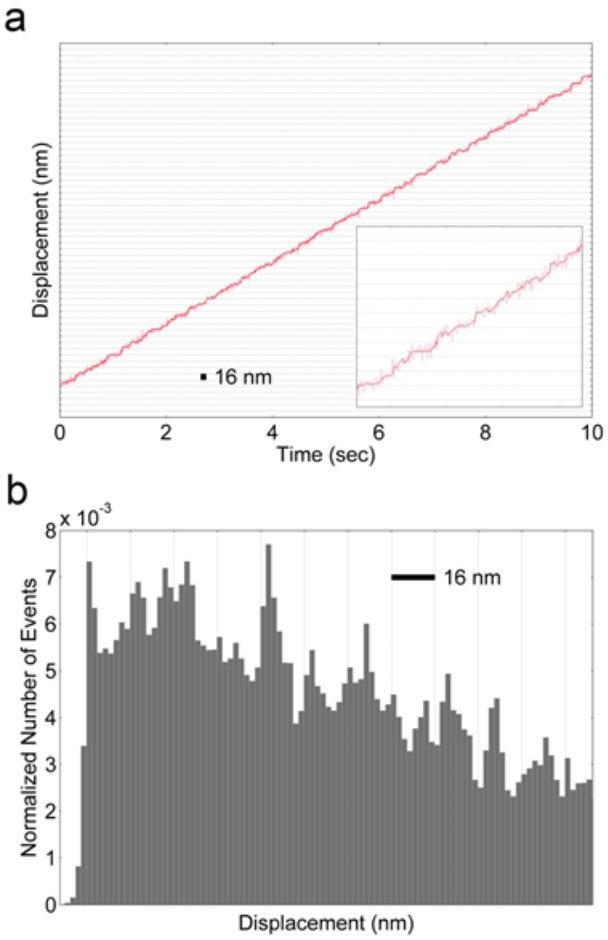

Figure 4-10 Simulated Ramp Signal with Similar Noise Level

(a) Light red line: simulated ramp signal with similar noise level as in negative control region over time. Red line: simulated signal after Chung-Kennedy filtering procedure. Inset: zoom-in signals from 1.7 s to 3s. (b) Pairwised histogram of simulated signal after Chung-Kennedy filtering. No peaks can be observed. Scale bar: (a) Distance between two horizontal grid line: 16 nm. (b) Distance between two vertical lines: 16 nm.

Conclusion

In conclusion, I have demonstrated a plasmonic imaging technique for tracking single organelle dynamics with nanometer precision. The scattering of the surface plasmonic waves by organelles creates high contrast images of the organelles, allowing for tracking of organelle dynamics with 5 nm accuracy, and ms-time resolution. Compared to fluorescent tracking techniques, the present plasmonic imaging method is label-free, fast, and provides accurate position information in all the three dimensions. Using the plasmonic tracking technique, I have successfully observed stepwise transportation of organelles in cell native state, providing molecular-scaled information of the motor proteins behind the organelle transportation. From the tracks of the individual organelles, I have further extracted the 3D structure of microtubule bundles in live cells. I anticipate the plasmonic imaging technique provide a powerful new tool for quantitative analysis of intracellular dynamic in live cells.

CHAPTER 5 VISUALIZING SUBCELLULAR ELECTROMECHANICAL DEFORMATION USING PLASMON-BASED DISPLACEMENT MICROSOCOPY (PLADIM)

Thermodynamics predicts that potential change is always accompanied with mechanical deformation. In mammalian cells, membrane potential depolarization is associated with subtle cellular deformation. This anisotropic mechanical response plays a significant role in regulating action potential firing in neurons and controls the mechanosensitive ion channels. However, methods for probing this nanometer to sub-nanometer scale deformation are limited. Scanning probe and optical beam can provide accurate displacement measurement; however, they are insufficient to resolve heterogeneous responses within single cells. Here, I provided a plasmon-based imaging method for visualizing heterogeneous subcellular displacement accompanied with electrical stimulation. This method is ultrasensitive to the deformation, and can map the deformation amplitude and direction down to subcellular level. Using this technique, for the first time, I comprehensively characterized electromechanical coupling of mammalian cells, and revealed a bidirectional deformation mode inside cells. Spectrum analysis further raveled an elastic behavior during cell deforming from Hertz to hundred Hertz range, which was mainly determined by mechanical property of cytoplasm. I also examined the effect of mechanical perturbation by depolarizing actin fibers. A significant directional phase shift was observed. I expect this imaging method will provide new approach for quantifying mechanical responses. This work will also shed light on the quantitative studies in mechanobiology.

Introduction

Electricity is one of the fundamental driving forces in biological systems(Hodgkin and Huxley 1952). It causes mechanical responses in various spatiotemporal aspects, such as intermolecular interactions induced by electrostatic forces(Leckband 2000) and structural changes in voltage-gated ion channels(Bezanilla 2008). The electromechanical coupling effect is also the basic machinery for heart cell beating and auditory sensing of hair cells.

Cellular deformation accompanied with membrane depolarization in mammalian cells has been recently resolved using atomic force microscopy (AFM)(Zhang, Keleshian et al. 2001). The nanometer scale displacement was physically predicted from thermodynamic Lippmann equation that surface tension changes proportionally with membrane potential. This universal mechanical force is pivotal in regulating neuron action potential firing and controlling mechanical gating at molecular level(Mueller and Tyler 2014). However, methods for quantifying this electromechanical responses is limited. AFM provides an accurate measurement on cellular displacement, but it lacks spatial resolution(Zhang, Keleshian et al. 2001). Moreover, to measure cellular displacement, a close contact to the cell of AFM tip is required. This causes the indention in the cell body, which might bias the measurement and cannot reflect the real mechanical response under cell native state. Other probing methods, including piezoelectric nanoribbon transducer(Nguyen, Deshmukh et al. 2012) and optical methods, such as spectral-domain optical coherence phase microscopy (SD-OCT) have also been applied for deformation measurement(Akkin, Joo et al. 2007). They are either one-location measurement or whole cell measurement, which are insufficient to resolve

subcellular responses. Quantitative phase microscopy has been employed recently(Oh, Fang-Yen et al. 2012). This label-free method provides imaging capability. However, quantitative information in subcellular level has not been systematically characterized yet.

Here, I demonstrated a plasmon-based imaging method that can accurately quantify the sub-nanometer cell displacement. Combined with ultrafast camera, this method provided a broad bandwidth measurement capability for displacement quantification. Using this technique, I systematically characterized the electromechanical property of cells, and revealed a heterogeneous subcellular response in both deformation magnitude and movement direction.

Materials and Methods

Cell culture

Wildtype HEK293T cell line (ATCC) was seeded on fibronectin (Sigma) coated gold film one day before the experiment. Cells were cultured in DMEM (Lonza) medium with 10% FBS (Life Technologies) according to user's manual from ATCC. After overnight incubation in 5% CO_2 humidified atmosphere at 37°C, cells attached to the sensor surface and were ready for experiment.

Electrophysiology

Cultured cells were recorded at room temperature in whole-cell configuration using Axopatch 200B system (Axon Instruments). Membrane potential was modulated sinusoidally from -60 mV to 140 mV in the voltage-clamp mode. Electrical current was simultaneously recorded. Glass micropipettes were pulled using a flaming puller (P-97, Sutter Instrument, CA). Intracellular recording solution containing 10 mM NaCl, 135 mM K-gluconate, 10 mM HEPES, 2 mM $MgCl_2$, 2 mM Mg-ATP and 1 mM EGTA (pH 7.4) was injected to the tip of pulled micropipettes. Micropipettes with typical resistance 3-10 MΩ was used for recording. The extracellular recording solution contains 135 mM NaCl, 5 mM KCl, 1.2 mM $MgCl_2$, 5 mM HEPES, 2.5 mM $CaCl_2$ and 10 mM glucose at pH 7.4. To depolymerize the actin structure, cells were incubated at 37 °C for 30 min in 10 μM cytochalasin D (CD)-containing media before measurements. Control cells were maintained in the normal culture media. Experiments with and without CD-treated cells were performed in the normal recording media.

Plasmonic imaging

An inverted microscope (IX81, Olympus, Shinjuku, Tokyo, Japan) with a 60× NA 1.49 oil immersion objective was implemented in the plasmonic imaging system. P-polarized light beam from a 670 nm superluminescent light emitting diode (SLD-26-HP, Superlum, https://www.superlumdiodes.com) was introduced into the microscope via a total internal reflection fluorescence tube lens (TIRF module, Olympus, Shinjuku, Tokyo, Japan) and a 50/50 beam splitter (Thorlabs, Newton, New Jersey, USA). The reflected light from the gold surface was detected by an CMOS (Complementary metal-oxide-semiconductor) camera (PIKE) with the full resolution (640 px × 480 px) recording at 106.6 frame per second (fps). To reveal the spectral response of the cell, an ultra-fast CMOS camera (Phantom V310, Vision Research, http://www.visionresearch.com) with a frame rate of 1000 fps was used. For step hyperpolarization and depolarization experiment, 10000 fps was applied to match the electrical sampling rate. Cameras were externally triggered by the patch clamp voltage controller for synchronization. Sensor chips were made from BK-7 glass coverslips by evaporated coating of ~1.5 nm chromium layer and a ~47 nm gold layer on top. Chips were rinsed with deionized water and ethanol before cell plating. Cells were cultured in a removable Flexi-Perm (Sarstedt, Newton, NC, USA) silicone cell culture chamber placed on top of the chip surface.

Displacement spectrum calculation

Raw plasmonic images were smoothed at 5×5 pixel (600×600 nm on PIKE camera) spatially to minimize the pixel noise. Fast Fourier transform (FFT) was applied to the images along time. Amplitude and phase-shift images at the lock-in frequency was obtained. Applied micropipette potential was used as reference for phase-shift

calculation. Local amplitude and phase-shift was obtained by manually choosing the region of interest and calculating the mean pixel value. Z-axis displacement was quantified by plasmonic amplitude-displacement relations. For potential step experiments, image sequences were aligned with polarization/depolarization steps. Multiple cycles were run on each potential step repeatedly. Image sequences were averaged over multiple cycles to enhance the signal to noise ratio. Local displacement was plotted and calculated for each potential step with 5 millisecond moving average smoothed over time. Spectral response was fitted with linear equation in logarithm scale. All post-acquisition analyses were carried out using custom-written MATLAB (Natick, MA, USA) scripts.

Results and Discussion

The Plasmon-based Displacement Microscopy (PLADIM)

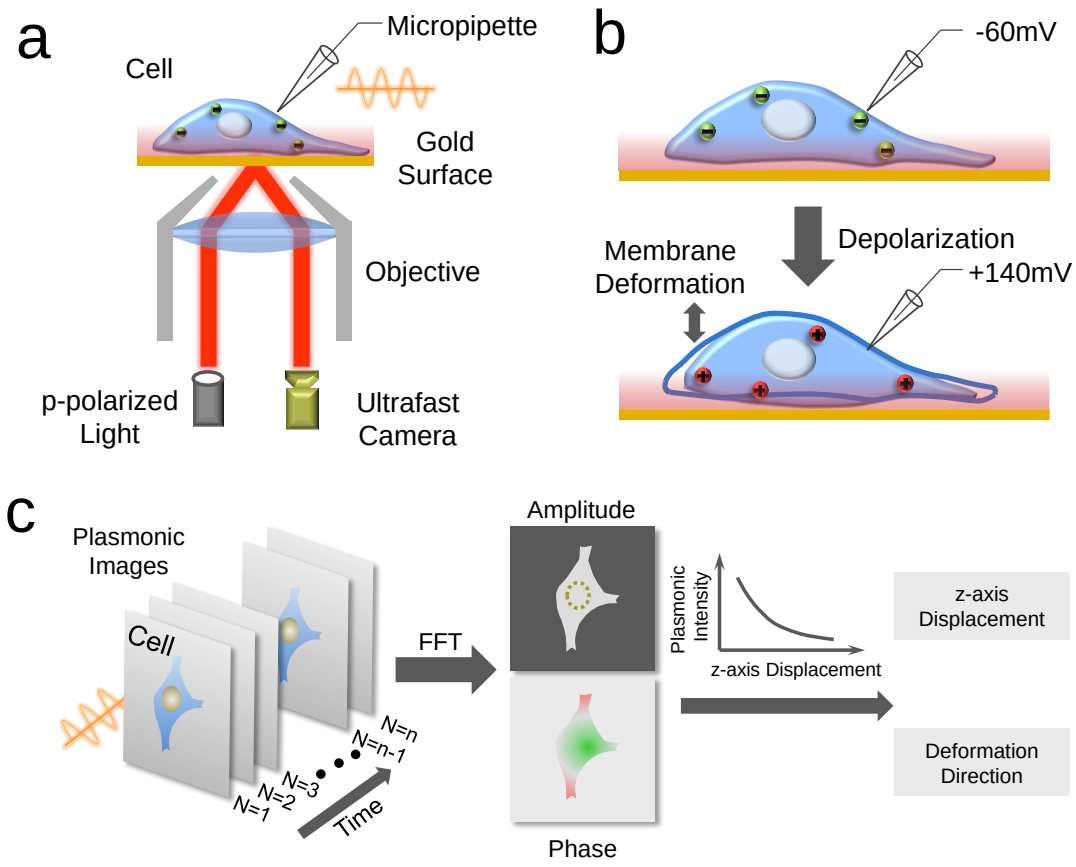

Figure 5-1 Plasmon-based Displacement Microscopy (PLADIM).
a) Cells are plated on the gold coated coverslip and imaged with plasmonic microscopy. Single frequency electrical modulation waveform was coupled into the cell from a micropipette in a whole-cell patch configuration. Plasmonic images was captured using a fast camera. b) Membrane potential change induces mechanical deformation on membrane, which predicted by Lippmann equation. c) Plasmonic images was analyzed by applying fast Fourier transform (FFT) along time. Amplitude and phase-shift images were picked on modulation frequency. Based on relations of z-axis displacement and plasmonic intensity, displacement magnitude and displacement direction can be resolved.

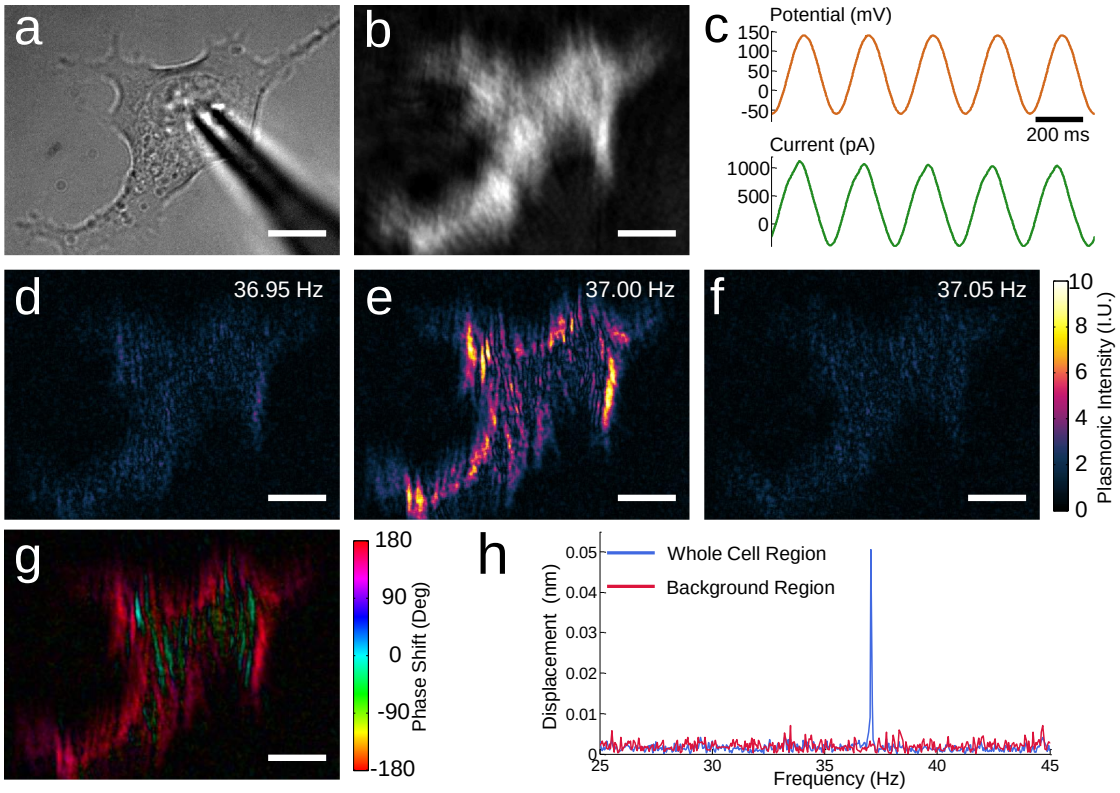

Figure 5-2 Electromechanical Response of the Cell.

Transmitted a) and plasmonic b) images of the cell that modulated with 37 Hz sinusoidal waveform c). d-e) Amplitude images of the modulated cell at different frequencies. Strong plasmonic intensity signal was observed at the modulation frequency e). No obvious signal at the nearby frequencies d) and f). g) Phase-shift image of the modulated cell. h) Spectrum response of the plasmonic intensity at the whole cell region and background region without cell. Obvious peak was observed at the modulation frequency in the whole cell region. Scale bar: 10 um.

I built a plasmonic imaging system on an inverted microscope (Figure 5-1a). HEK293T cells were cultured on top of a glass coverslip coated with 47 nm-thick gold film. High numerical aperture objective coupled incident light onto the gold surface and directed the reflected light into a CMOS camera for imaging. When the incident light reaches surface plasmon resonance angle, plasmonic images were recorded. At the resonance angle, because the evanescent wave created on the surface decays

exponentially into the solution with an extremely short decay constant at only about 100 nm, plasmonic imaging is ultrasensitive to the displacement along the direction perpendicular to the surface. Previously, I have successfully detected a 0.1 nm displacement of nanoparticle oscillation using the plasmonic imaging method.

Previous studies indicated that cell electromechanical fluctuation is only within the range of sub-nanometer to nanometer. To unveil such small signals, I modulated the membrane potential at a single frequency by coupling a 200 mV peak-to-peak amplitude sinusoidal waveform into the cell while simultaneously capturing plasmonic images(Figure 5-1b). Small mechanical signal can be isolated by applying fast Fourier transform (FFT) to the image sequences along the time axis (Figure 5-1c) and extracted the amplitude and phase-shift images at the modulation frequency. These images represented corresponding intensity fluctuation magnitude and response delay that is relative to the modulating force. To further quantify the cell deformation, I calculated local displacement from modulation amplitude based on intensity decay function along the z-axis. For small plasmonic intensity change ΔI, the fractional intensity change, $\Delta I/I$, is linear with displacement change Δz over decay constant λ. I experimentally verified that the intensity decay constant along the z-axis is about 100 nm, which is close to theoretical simulation result.

Visualizing Heterogeneous Subcellular Electromechanical Response

Figure 5-2a-b showed transmitted and plasmonic images of a cell clamped with a micropipette. Plasmonic image represented the mass density of cell bottom part that was within the penetration depth of the surface evanescent wave. Since micropipette is beyond the penetration depth, it cannot be observed on the plasmonic image. I then drove

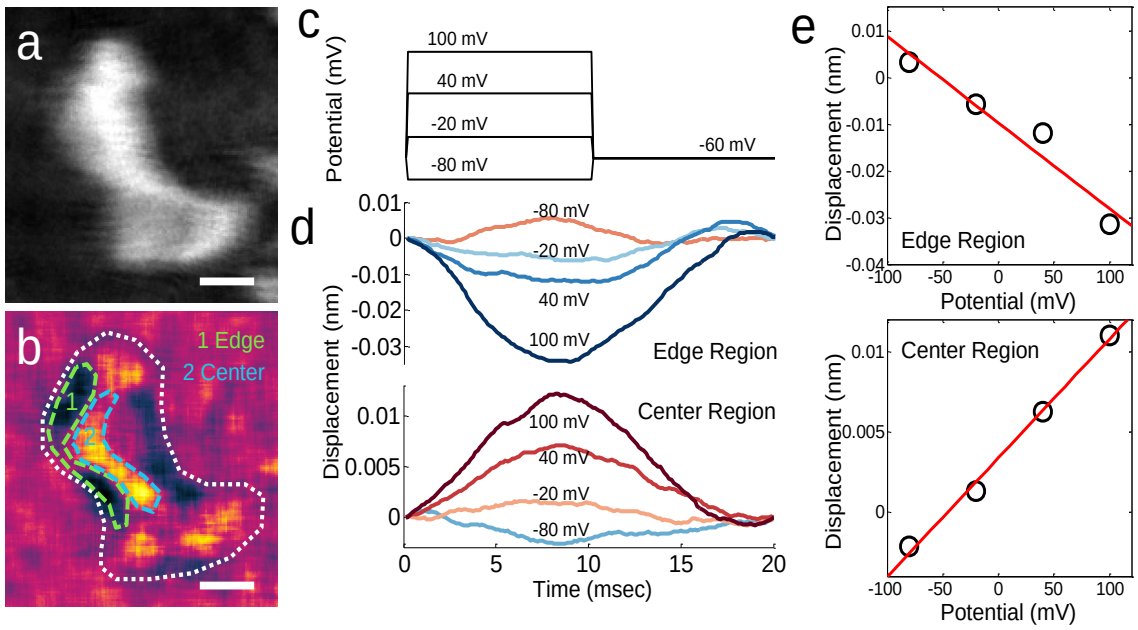

Figure 5-3 Cell Deformation with Different Modulation Amplitude

a) Plasmonic image of potential stepwise modulated cell. b) Differential plasmonic image of depolarized cell at potential step of 100 mV. White line indicated the morphology of the cell. c) Potential step protocol used in modulation. d) Averaged displacement profile calculated from cell edge region and cell center region that responded to the stepwise modulation. e) Relationship of averaged displacement calculated from cell edge region and cell center region at the steady state with the potential steps. Scale bar: 10 um.

the membrane potential oscillation from -60 mV to 140 mV by coupling a 37 Hz sinusoidal waveform from the whole-cell patched electrode for 10 seconds (Figure 5-2c). An enhanced amplitude signal at the lock-in frequency was observed comparing with nearby frequencies (Figure 5-2d-f). To clearly examine the spectral response, I plotted the frequency spectrum in the whole cell region and the background region outside the cell (Figure 5-2h). A sharp peak at the stimulation frequency clearly showed in the whole-cell region plot, while a relative flat noise showed in the background region. This sharp peak illustrated the electrical induced mechanical response of the cell. From the amplitude

image at the stimulation frequency (Figure 5-2e), heterogeneous subcellular mechanical response was clearly visualized. Cell edge showed a much higher mechanical fluctuation than the center region.

To quantify the time delay of this mechanical response, I analyzed the phase-shift of the response at the stimulation frequency. Figure 5-2g presented the phase-shift of the same cell relative to the driving micropipette potential signal. Interestingly, two types of deformation in opposite phases were observed inside cell. The center region showed a phase-locking (0°) response (cyan), while the edge area was mainly ~180° out of phase (red). No intermediate phase lag was observed. This 0° and 180° only phase-shift map indicated that deformation follows the driving electrical force at the modulation frequency, while domains at the cell center and the cell edge moved in opposite directions, that is, the center regions moved towards the gold surface and the edge regions moved away from the surface when the membrane potential is depolarized (Figure 5-2b). This observation is consistent with the hypothesis that the whole cell volume is conserved during the process of electrical-driven mechanical deformation. Thus, by combining plasmonic imaging system with electrophysiological stimulation, I visualized heterogeneous subcellular response within single cells induced from electromechanical coupling.

Electromechanical Deformation Is Proportional to the Membrane Potential

To further study the relationship between mechanical response and membrane potential, I measured corresponding mechanical response at different membrane polarization levels. The clamped cell was electrically hyperpolarized and depolarized from -80 mV to 100 mV at the interval of 20 mV per step (Figure 5-3c). Plasmonic

response was simultaneously monitored (Figure 5-3a). Figure 5-3b showed a cellular response of depolarization from -60 mV to 100 mV. Consistent with the AC modulation results, the cell center showed an increased response with the membrane depolarization, while the cell edge showed an opposite response. To accurately quantify the dynamic response of cell deformation, I plotted the temporal profile of averaged displacement in the center region and the edge region respectively (Figure 5-3d). Both regions exhibited a gradual deformation change with stepwise membrane potential modulation. Displacement magnitude showed a linear relationship with the membrane potential at the steady state. I plotted displacement magnitude versus membrane potential for both the cell center and the edge in Figure 5-3e. Deformation magnitude changed linearly with membrane potential, with an averaged displacement about 0.002 nm per 10 mV potential change. The number is higher than that in the cell center, which only displayed a 0.0005 nm change per 10 mV depolarization. These numbers are about one order smaller than previous studies, which I think is mainly due to the confined mechanical movement at the bottom of adherent cells. Therefore, I confirmed that electromechanical response is linearly proportional to the membrane potential. The cell center and cell edge displayed an opposite deformation direction.

Elastic Behavior of Cell Electromechanical Deformation

I now turn to the detailed mechanism of electromechanical coupling on single cell. Thermodynamics predicts that transmembrane voltage modulates membrane tension leading to mechanical deformation in the membrane. The relationship between membrane surface tension and membrane potential for a single interface can be described as Lippmann equation: $d\gamma/dV = -q$, where γ is the surface tension, V is the membrane

electrical potential, and q is the excess mobile charge in the double layer of the membrane surface. However, thermodynamics does not tell how much cell will deform with the given changes of membrane potential. The actual magnitude and time delay of the deformation induced by the membrane tension is determined by the mechanical properties of the cytoplasm.

To examine how fast cells can respond to the driving electrical force mechanically and study the mechanical properties of the cell systematically, I performed a spectral measurement on the deformation displacement. I measured the cellular mechanical response over the frequency range from 7 Hz to 312.5 Hz with same modulation amplitudes. Figure 5-4a-e illustrated the plasmonic response at different frequencies. For data visualization, plasmonic amplitude was shown in brightness value and the phase-shift was encoded in hue value. My measurements displayed a quasi-in phase mechanical response with the applied potential modulation (0° and 180° only) over the frequency range. To explain the results, a complex bending modulus $G = G' + iG''$ is introduced, where G' is bending storage modulus and G'' is bending loss modulus. $G(f)$ is examined by calculating the ratio between applied oscillatory force $F(f)$ at frequency f and corresponding displacement $x(f)$, that is, $F(f)/x(f)$, in the frequency domain. Thus, the behavior of a cell (G) can be modeled as a combination of an in-phase elastic component, which described in G', and a 90° phase-lag viscous component, G'' in series (Figure 5-4f). Therefore, the in-phase mechanical response showed in Figure 5-4a-e revealed that the cell was mainly an elastic body rather than a viscous one within the frequency range.

Because Lippmann equation predicted a correspondent change in membrane potential and in surface tension, I can extract the cytoplasm mechanical properties by

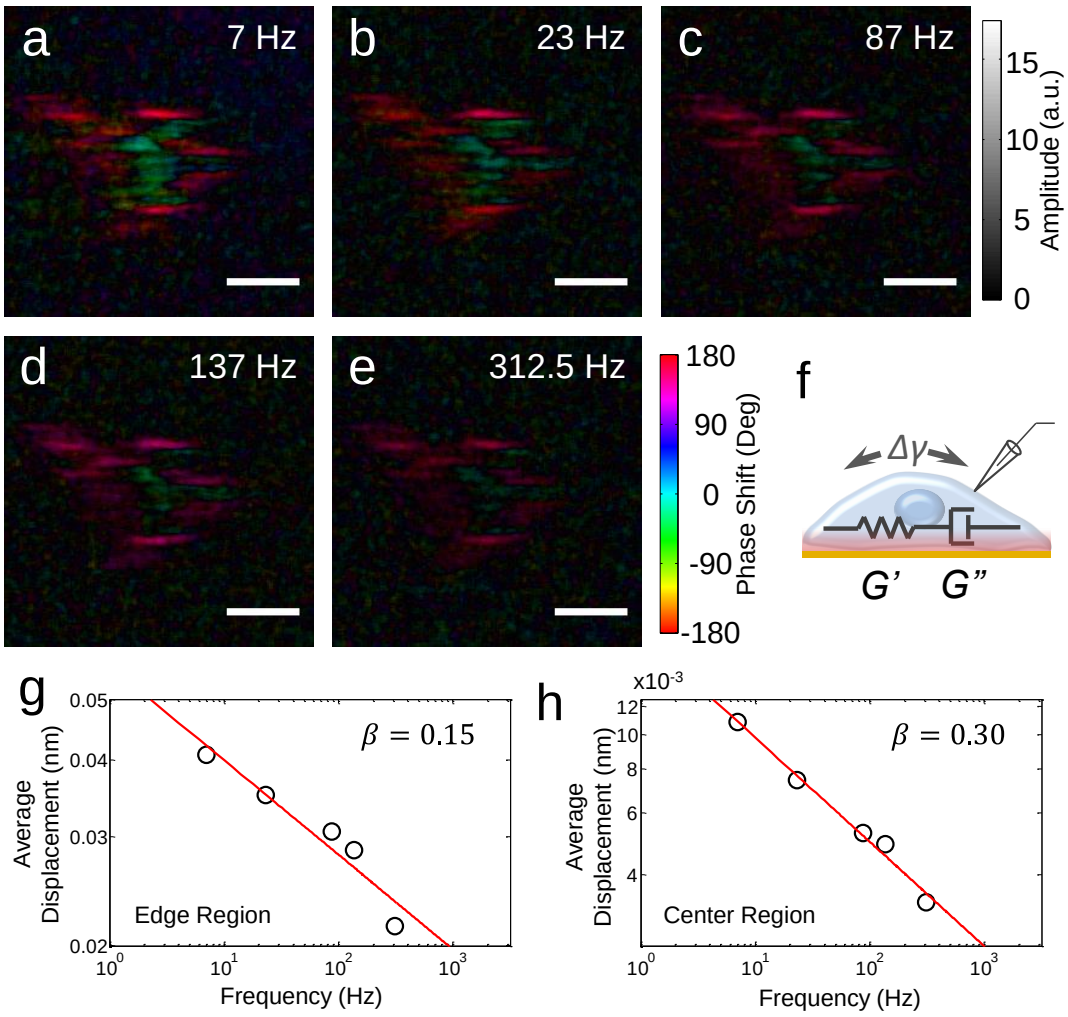

Figure 5-4 Cell Deformation with Different Modulation Frequency

a-e) Cellular response with different modulation frequencies. f) Mechanical model of cell deformation. g-h) Averaged displacement in the cell edge and the cell center in response to the modulation frequencies. Data was plotted in log-log scale and fitted with linear equation. Scale bar: 20 um.

analyzing the relation between displacement and the applied voltage. I calculated the averaged displacement at both the cell center and the edge and examined the amplitude response over frequencies. Figure 5-4g-h showed the spectral response of displacement

with same stimulation amplitude at both regions. Fitted with linear equation in log-log scale, the displacement followed a negative power-law form: $|x(f)| \sim f^{-\beta}$ with β equals to 0.15 and 0.3 in edge and center region respectively. Storage modulus, the inverse of displacement with the same modulation amplitude, thus displayed a positive power-law relationship with frequency, $|G'(f)| \sim f^{\beta}$. This weak positive power relationship is in agreement with previous rheological measurements using intracellular microbead or cytoskeleton-attached magnetic nanoparticle conducted on other types of cells. The power index β for the cell edge is consistent with these studies, while the number for the cell center is two times higher, which indicated a stronger relationship with the increasing frequency in the cell center. Thus, I systematically characterized the cell spectral electromechanical deformation and revealed a heterogeneous subcellular response. Spectrum analysis further unveiled an elastic behavior during cell deforming from Hertz to hundreds of Hertz range. I also verified this sub-nanometer deformation was mainly determined by mechanical property of cytoplasm.

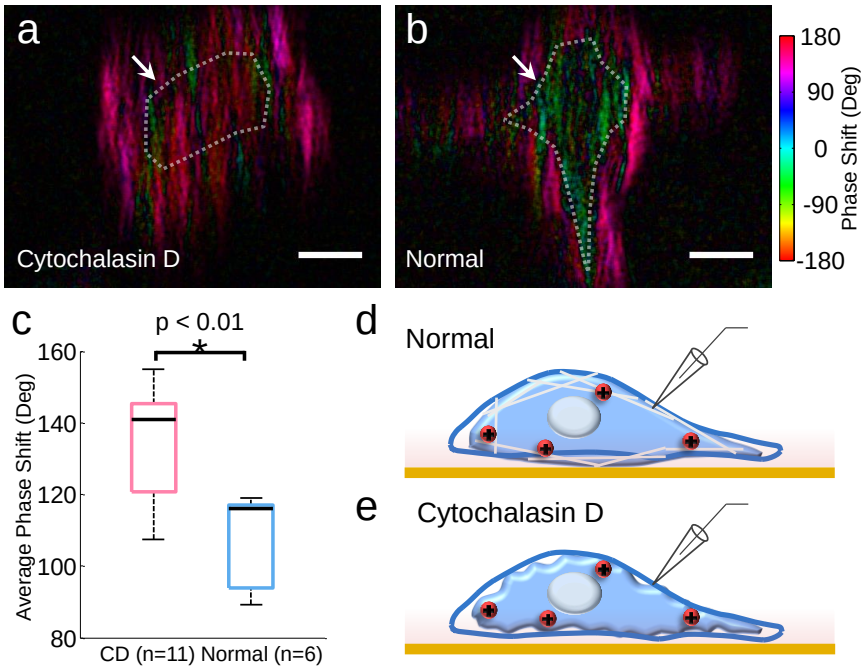

Figure 5-5 . Electromechanical Response of Cells Treated with Cytochalasin D
a-b) Electromechanical response of cytochalasin D treated a) and normal cells b). White lines indicated the cell center regions which supposed to show phase-locking response in normal condition. c) Averaged phase shift of the whole cell region. $p<0.01$, t-test. d-e) Cartoons illustrated the possible mechanism of electromechanical response for cytochalasin D treated and normal cells. Scale bar: 10 um

Perturbation in Cytoskeleton Causes Altered Subcellular Response

By perturbing mechanical structure of cells, I expected electromechanical response would be altered as well consequently. To confirm this hypothesis, I treated the cells with an actin polymerization inhibitor, cytochalasin D, and examined the corresponding response. Intriguingly, after depolymerizing the actin frame, cells displayed a different mechanical response. Phase-shift in the cell center showed a much larger negative phase area compared with those in normal condition (Figure 5-5a-b, indicated as white dash lines). Correspondingly, the phase-following region, which moves towards to the gold surface along with the cell depolarization, was shrunk.

Compared with those well-separated phase regions at the cell center and the cell edge in the normal condition (Figure 5-5b), these 0° and 180° phase regions appeared randomly with undefined subcellular location. To examine the subcellular phase changes, I quantified the average phase over the whole cell area. A significant phase shift towards reverse phase (180°) after cytochalasin D treatment was observed (Figure 5-5c). This shift indicated a larger synchronous unidirectional region that moved inward over the whole cell. Because cytochalasin D breaks the structure of cytoskeleton, the soften effect are likely to reduce the modulus that are resistant to subtle surface area changes, and leads to the biased phase shift at the cell bottom. Such structural change can also contribute to a more randomized pattern observed here by generating smaller unconnected subdomains in the membrane structures (Figure 5-5d). Therefore, I confirmed the observation of structural change of electromechanical coupling. Cytochalasin D treatment also revealed an altered subcellular response to the driving electrical force.

Conclusion

In this paper, I demonstrated a plasmon-based imaging method for quantifying cellular deformation induced by potential changing. Sub-nanometer displacement was accurately detected. I resolved and visualized a heterogeneous subcellular displacement response in both deformation magnitude and movement direction. I also systematically characterized the electromechanical property of mammalian cells, and revealed subcellular anisotropic deformation in both amplitude and spectrum manners. I further examined the effect of mechanical perturbation by destructing the actin structure. An obvious directional shift in the cell center was observed. Thus, using plasmon-based imaging method, I successfully unveiled the inverse piezoelectric effect within single cells.

The extremely short penetration depth of evanescent wave created on the surface enables the ultrasensitive measurement on the subtle mechanical displacement of cells presented here. The sensitivity can be further improved by longer modulation time with more stimulation cycles. The plasmon-based imaging technique detects the reflected light; therefore, the imaging speed is not constrained. Higher speed camera can be implemented to achieve broader spectrum for deformation measurements. However, the applied electrical force might be problematic at higher frequencies due to the effect of the membrane capacitance and resistance in the electrical circuit formed in the whole-cell patch configuration.

In sum, I demonstrated an optical method for detecting sub-nanometer displacement from cell electromechanical coupling. I expect this electromechanical imaging capability can be used as a novel detecting strategy for measuring cell membrane

potentials, including action potential firing in neurons. The systematical study on cellular electromechanical coupling presented here will provide new insights into mechanobiology studies, and shed light on the understanding of biological function from an electromechanical aspect in systems, such as mechanosensitive ion channels and protein configuration changes in voltage-gated ion channels.

CHAPTER 6 PLASMONIC IMAGING OF ACTION POTENTIAL AND ITS PROPAGATION IN NEURONS WITH SUB-MILLISECOND RESOLUTION

Measuring the action potential and its fast propagation in neurons is critical to the understanding of neuron physiology. The patch clamp technique using micropipettes has been the gold standard, but a non-invasive tool with both high spatial and temporal resolution to resolve fast and local electrical activities is highly desirable. Here I report a plasmonic technique to image the electrical activities in mammalian neurons. The technique measures a mechanical deformation associated with an action potential in the neurons optically with sub-millisecond resolution, which allows me to image the fast initiation and propagation of action potentials within single mammalian neurons. The measured action potential waveforms agree with those simultaneously recorded with the patch clamp technique. I further show the technique works for both the current and voltage clamp modes. I anticipate that the plasmonic imaging technique will provide a new optical approach to study neuronal activities with complementary capabilities to the existing techniques.

Introduction

Neuronal signaling relies on the initiation and propagation of action potentials within a neuron and a network of neurons at millisecond or shorter time scales (Boyden, Zhang et al. 2005, St-Pierre, Marshall et al. 2014). The patch clamp technique is the gold standard tool that can measure the electrical activities of neurons with a micropipette at the millisecond time scale. While powerful, the technique can be invasive and has limited spatial resolution (Peterka, Takahashi et al. 2011). Fluorescent imaging techniques using Calcium (Grewe, Langer et al. 2010, Chen, Wardill et al. 2013, Berlin, Carroll et al. 2015), and voltage fluorescent indicators (Tsutsui, Karasawa et al. 2008, Popovic, Foust et al. 2011, Jin, Han et al. 2012, Kralj, Douglass et al. 2012, St-Pierre, Marshall et al. 2014) have been developed to provide high spatial resolution imaging of the electrical activities in neurons. However, the fluorescent imaging techniques are usually too slow to resolve the fast action potentials. To overcome the speed limitation, a novel engineered voltage indicator was developed, which together with a sub-frame interpolation approach, allows fast imaging of neuronal activities(Hochbaum, Zhao et al. 2014). Another recent effort was to use an electrochromic dye to measure electrical signals from dendritic spines(Popovic, Carnevale et al. 2015).

Here I report a label-free optical technique to image the action potentials in mammalian neurons with high spatial and temporal resolution. Using this capability, I image transient electrical activities in single neurons, and resolve the fast initiation and propagation of action potential within a neuron. I validate the plasmonic technique performing simultaneous electrical recording with the patch clamp technique. Furthermore, I show that the plasmonic imaging technique works in both current and

voltage clamp modes. Unlike the fluorescent imaging approaches, the present technique is based on plasmonic imaging, which does not require labeling of neurons, and measures intrinsic physical characteristics of the neurons, which can potentially provide complementary capabilities to the existing techniques.

Materials and Methods

Neurons cell culture

Primary rat hippocampus neurons (Life Technologies, Carlsbad, CA, USA) were recovered from cryopreservation and seeded on poly-L-lysine (Trevigen, Gaithersburg, MD, USA) coated gold film with a coverage of ~10^5 neurons/cm^2. After incubation in a humidified atmosphere with 5% CO_2 at 37°C for 4~8 days, the neurons attached to the surface and were ready for experiment. The neurons were cultured in neurobasal medium (Life Technologies, Carlsbad, CA, USA) with B-27® supplement (Life Technologies, Carlsbad, CA, USA) and GlutaMAX™ (Life Technologies, Carlsbad, CA, USA).

Plasmonic imaging set-up

The plasmonic imaging system was built on an inverted microscope (Olympus IX81) with a TIRF imaging attachment using a 60× NA 1.49 oil immersion objective. The light source was a 670 nm superluminescent light emitting diode (SLD-26-HP, Superlum, https://www.superlumdiodes.com). For high temporal resolution imaging, an ultra-fast CMOS (Complementary metal-oxide-semiconductor) camera (Phantom V310, Vision Research, http://www.visionresearch.com) with 10,000 frames per second in 256 pixels by 256 pixels was used. For resolving individual action potentials, a low noise sCMOS camera (scientific CMOS, ORCA-Flash 4.0, Hamamatsu, Japan) was also utilized at frame rate of 1603 fps with 2048 pixels by 128 pixels. Images were directly streamed into SSD hard-disks with parallel writing. To synchronize the electrical recording with plasmonic recording, cameras were externally triggered by the patch clamp voltage controller. The setup was placed on a floating optical table and enclosed in a custom build faradic cage and acoustic enclosure to minimize electrical and mechanical

noises. The gold films were prepare by evaporating 2 nm chromium adhesion followed, followed by ~47 nm gold on BK-7 glass coverslips. Each gold film was washed with water and ethanol followed by hydrogen-flame annealing in order to remove possible surface contamination. The gold films were modified with 140 µl of 5 µg/ml poly-L-lysine solution in 37 °C for one hour, and further rinsed with deionized water twice prior to cell seeding. A removable Flexi-Perm silicon chamber (SARSTEDT, http://www.sarstedt.com) was placed on top of the gold chip to serve as a culture chamber.

Electrophysiology

Cultured hippocampal neurons were recorded in whole-cell configuration, using Axopatch 200B amplifier (Axon Instruments) at room temperature on the plasmonic imaging set-up. To identify the plamonic signal, membrane potential was modulated sinusoidally from -60 mV to 140 mV in the voltage-clamp mode at 23 Hz for 10 seconds (otherwise indicated in manuscript). To trigger multiple action potentials, depolarizing current pulse trains with amplitude of 500 pA and duration of 2-4 ms were typically applied in a current clamp mode at 23 Hz for totally 4 seconds (otherwise indicated in manuscript). Typically, all the current pulses will excite action potentials. For noise identification, neurons were evoked at a pattern of combined 23 Hz and 37 Hz for total 86 cycles. Glass micropipettes were prepared by a flaming puller (P-97, Sutter Instrument, CA), which were filled with 10 mM NaCl, 135 mM K-gluconate, 10 mM HEPES, 2 mM $MgCl_2$, 2 mM Mg-ATP and 1 mM EGTA (pH 7.4). The resistance of these micropipettes is 5-10 MΩ. Neurons were recorded in extracellular recording

solution, containing 135 mM NaCl, 5 mM KCl, 1.2 mM $MgCl_2$, 5 mM HEPES, 2.5 mM $CaCl_2$ and 10 mM glucose at pH 7.4.

Sodium ion channel inhibitors TTX was added to the above extracellular recording solution for inhibiting action potential initiation (1 μM, final working concentration). For actin depolymerization experiment, cytochalasin D (CD) stock solution was diluted with culture medium to the final concentration of 10 mM, and the neurons were incubated at 37 °C for 30 min before measurements. Neurons of control group were maintained in normal culture media. Experiments with and without CD-treated neurons were both performed in the normal recording media.

Data analysis

In potential modulation experiment, raw plasmonic images were spatially smoothed with 3×3 pixel (0.9×0.9 μm) mean kernel. After aligning with the starting of the potential modulation, Fast Fourier Transform was applied to the plasmonic image sequences along time. Amplitude image at the lock-in frequency was picked. Subcellular response was obtained by examining the lock-in response at the frequency domain of the ROI intensity profile in the region that manually selected from the image. Relative phase-shift to the driving electrical signal was also examined. For action potential visualization with multiple pulse stimulations, image sequences were filtered with 11×11 pixel (3.3×3.3 μm) mean kernel and aligned with injected current pulses. The mean image stack was obtained by averaging over multiple cycles with typical cycle number of 40-150. Optical response was examined and displayed in a differential way by subtracting the first image of the mean image stack. To remove spatial noise, the mean image stack was temporally detrended pixel by pixel using a fitted linear function. High frequency

noise was further suppressed by a digital FIR low-pass filter with 1 kHz cut-off frequency. For individual spike resolving, a 50 ms moving average signal of intensity profile from the ROI was removed to subtract out the long-term drift (20 Hz high-pass filter). Bands at frequencies of 60 Hz, 120 Hz, 180 Hz, 300 Hz, 420 Hz and 540 Hz were digitally filtered, which were typical noise from electrical sources. Intensity profile was further smoothed with 5 ms moving average for plotting. The electrical signals recorded with the patch clamp were filtered by a 2 kHz low-pass Bessel filter. To accurately identify the time-lag of action potential propagation, Lorentzian function was utilized to fit the peak position of action potential at different region. Local intensity profile was plotted by manually choosing the region of interest. All post-acquisition analyses were carried out by custom-written MATLAB (Natick, MA, USA) codes.

Contributions to plasmonic imaging intensity

Ionic concentration effect on plasmonic imaging

The diffusion coefficient (D) of Na^+ ions in water at room at room temperature is 1.33×10^{-5} $cm^2\cdot s^{-1}$. According to the diffusion equation, $l = \sqrt{2Dt}$, the averaged diffusion distance for Na^+ ions is about 2.3 μm during the 2 ms action potential excitation period (Figure 6-1a). From the measure current, I estimated a total amount of ~2.7×10^{-17} mole of Na^+ ions transported into a neuron during an action potential spike (Figure 6-1b). The average diameter of the neurons is ~20 μm, from which the Na^+ ion concentration change near the gold film during action potential was determined to be ~1.6×10^{-5} mM, which corresponds to a shift in surface plasmon resonance angle of ~0.04 mDeg, 5 times smaller than the observed signal associated with the action potential spike.

Electrical contribution to plasmonic imaging intensity

The local surface charge density ($\Delta\sigma$) and surface plasmon resonance angle change ($\Delta\theta$) are related by $\Delta\sigma = \alpha\Delta\theta$, where α is a constant (=28 $C\cdot m^{-2}$ deg^{-1})(Foley, Shan et al. 2008). The total transient charge change due to the flow of Na^+ and K^+ ions during an action potential spike is 5.5×10^{-11} C as determined by integrating of the sodium and potassium current. The projected surface area of neuron calculated is 447 μm^2 (Figure 6-1), the induced surface charge density is 1.2×10^{-3} $C\cdot m^{-2}$, from which the plasmonic signal ($\Delta\theta$) is ~0.044 mDeg, which is 5 times smaller than the observed signal associated with the action potential spike..

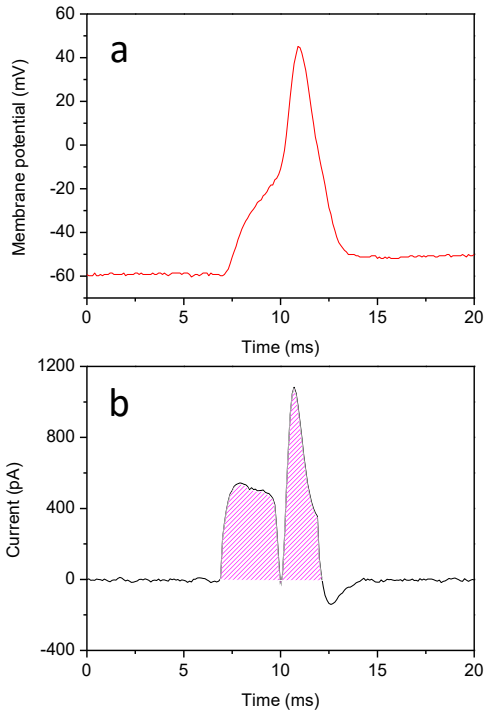

Figure 6-1 Membrane Potential Change
(a), and ionic current (b) recorded during action potential. The shaded area was integrated to calculate the ion flux during an action potential spike.

Results and Discussion

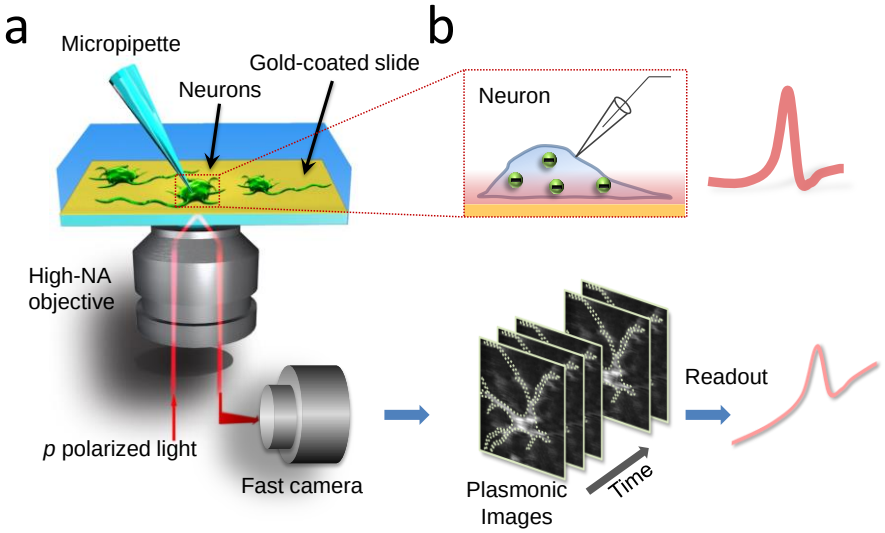

Figure 6-2 Setup of Plasmonic Imaging of Action Potential in Neurons.
(a) p-polarized light beam is directed onto a gold-coated glass coverslip through an oil immersion objective to excite plasmons on the gold surface, which is imaged optically with a fast camera. Neurons are cultured on the poly-L-lysine-coated gold surface, and a micropipette is patched on one neuron to trigger action potential that is recorded with both the patch clamp electronics and plasmonic imaging. (b) Plasmonic images are captured simultaneously with electrical action potential firing.

Plasmonic imaging of action potential

Figure 6-2a illustrates the plasmonic imaging setup built on an inverted optical microscope with a high numerical aperture oil emersion objective (Huang, Yu et al. 2007). Placed on the objective was a glass slide coated with a 47 nm-thick gold film. The film was further modified with a layer of poly-L-lysine, on which neurons were cultured. Incident light from a super luminescent diode was directed onto the gold surface through the objective, and the reflected light was collected with the same objective and then directed to a CMOS camera to create a plasmonic image (Figure 6-2a). The temporal resolution was limited by the CMOS camera, which was 10 μs in the present study for a

frame rate of 100,000 fps. The neuronal excitation was triggered with a conventional patch-clamp recording setup in either the current-clamp mode or the voltage-clamp mode, and the corresponding voltage or current were recorded electrically with the traditional patch clamp electronics, and optically with P-EIM, simultaneously (Figure 6-2b).

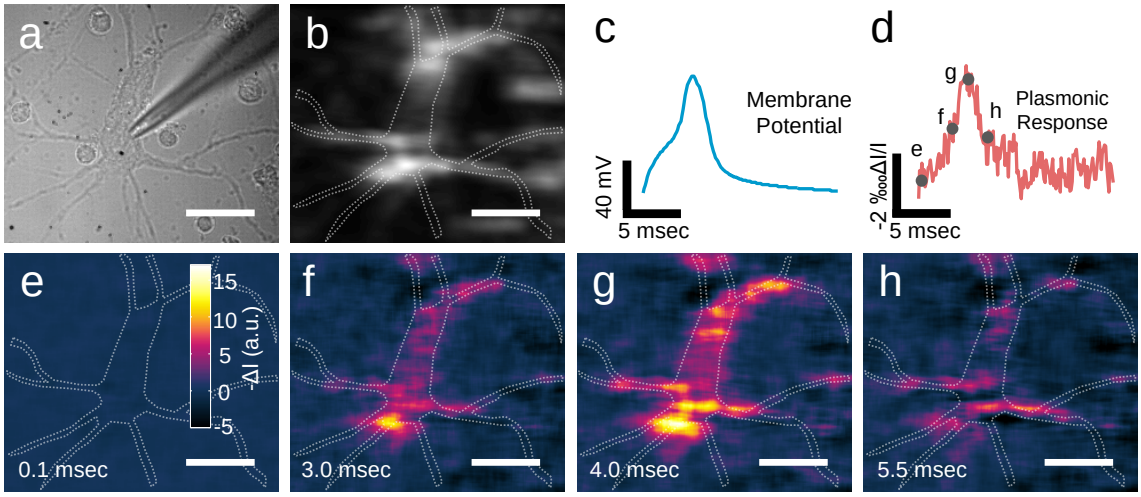

Figure 6-3 Plasmonic Imaging of Action Potential in Single Neurons.
(a) Optical transmission and (b) plasmonic images of a hippocampal neuron, where the dashed lines mark the edge of a neuron. (c) Patch clamp recording of action potential and (d) simultaneous P-EIM recording of action potential of the whole cell (frame rate of 10,000 fps). (e-h) Snapshot P-EIM images of action potential at the moments marked by the red spots in (d). The P-EIM images were averaged over 90 frames for noise reduction.

Figure 6-3a and b show both bright field and plasmonic images of a hippocampal neuron cultured from embryonic day 18 rat. A command current with peak value of 500 pA and width of 4 ms (in current-clamp mode) was injected through the patch electrode, and triggered a single action potential spike with a width of ~2 ms, as recorded with the patch clamp electronics (Figure 6-3c). The transient plasmonic image intensity of the neuron during the action potential firing process is shown in Figure 6-3d, exhibiting a spike with shape and width similar to the action potential spike obtained from the patch-

clamp recording. However, unlike the electrical recording, the P-EIM images provide both spatial and temporal resolution. Figure 6-3e-h show several snapshots of the movie during different stages of the action potential spike (marked in Figure 6-3d). Note that the P-EIM images shown in Figure 6-3 are differential images, obtained by subtracting each frame with the initial frame captured before the firing of the action potential and averaged over multiple stimulation cycles.

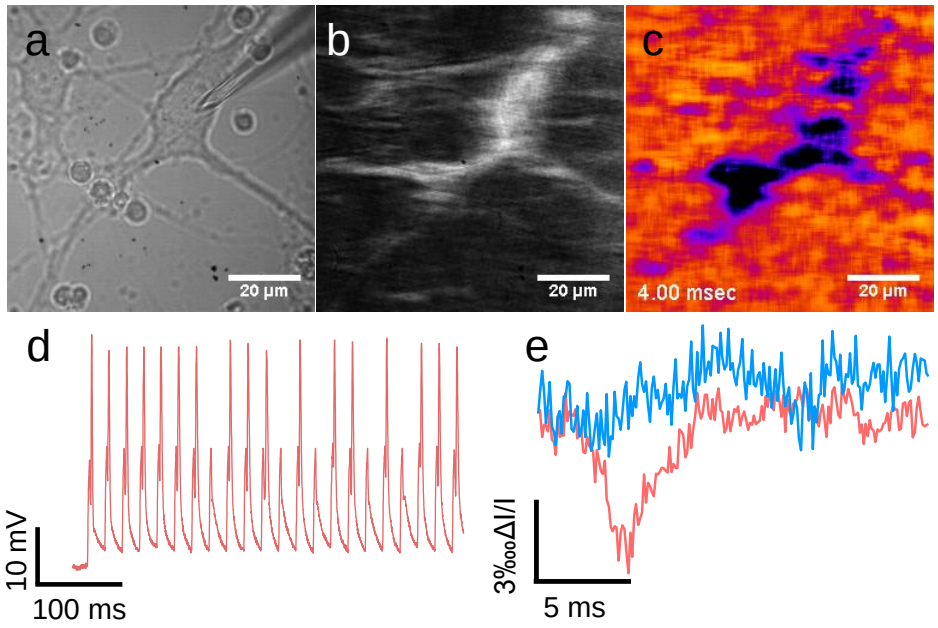

Figure 6-4 Failed Cycles of Action Potential Firing.
Optical transmission (a) and plasmonic (b) images of hippocampal neuron. A snapshot plasmonic imaging of action potential at 4 ms after triggering (c). Electrical recording of action potential with patch clamp (d). Plasmonic recording of a successful (blue) and failed (red) action potential firing.

I triggered neuronal action potentials repeatedly with a frequency of 50 Hz. In some cycles, action potentials were not generated, which is also often observed in the traditional patch-clamp electrical recording of action potential. This characteristic is distinctly different from the passive depolarization and polarization of the membrane,

which always accompany with electrical triggering (Figure 6-4). To further confirm that the plasmonic image response was caused by action potential, tetrodotoxin (TTX), a sodium ion channel inhibitor, was used to block action potential generation. The plasmonic images show no spikes that can be attributed to the action potential after blocking the sodium ion channel with TTX (Figure 6-5). These observations, together with the close resemblance in the shape and width of the plasmonic spikes with the electrically recorded action potential peaks, and additional evidence described below, confirm that the plasmonic signal is indeed generated by action potential.

Plasmonic imaging of action potential propagation in single neuron

P-EIM is capable of high spatial and temporal resolution imaging of action potential in neurons. Using this capability, I measured action potential initiation and propagation within a single neuron. Figure 6-6a and b show bright field and plasmonic

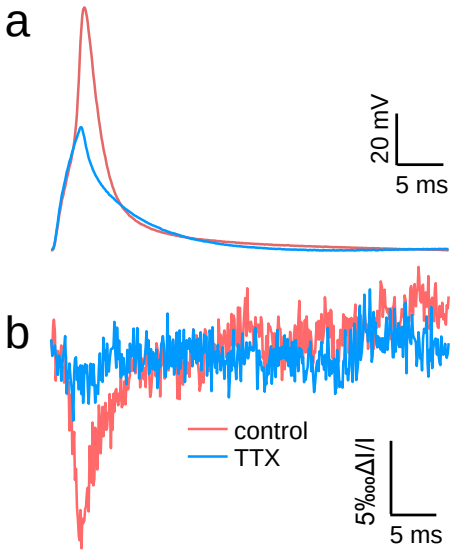

Figure 6-5 TTX Inhibition Effect

TTX inhibited Na+ ion channel (red) and control experiment (blue) measured with the patch clamp (a) and plasmonic recordings (b).

images of two neurons outlined with dashed lines, 1 and 2. Action potential was triggered in neuron 1 at the location marked with a white dot. Figure 6-6c plots the action potentials measured at different locations of neuron 1, and neuron 2, which show well-defined action potentials in neuron 1, but no action potential in neuron 2, indicating that the two neurons were not electrically connected. Examination of the action potentials at different locations reveals time delays at different locations of the neuron. For example, Figure 6-6d shows a 0.5-ms lag of action potential at two locations, one (outlined with green line) is near the triggering point, and the other one (outlined with purple line) is near the end of the axon (see Figure 6-6b). This observation indicates that the sub-millisecond temporal resolution of the present plasmonic imaging technique may be used to directly track signaling propagation within a single neuron, which has been an extremely difficult task with traditional methods.

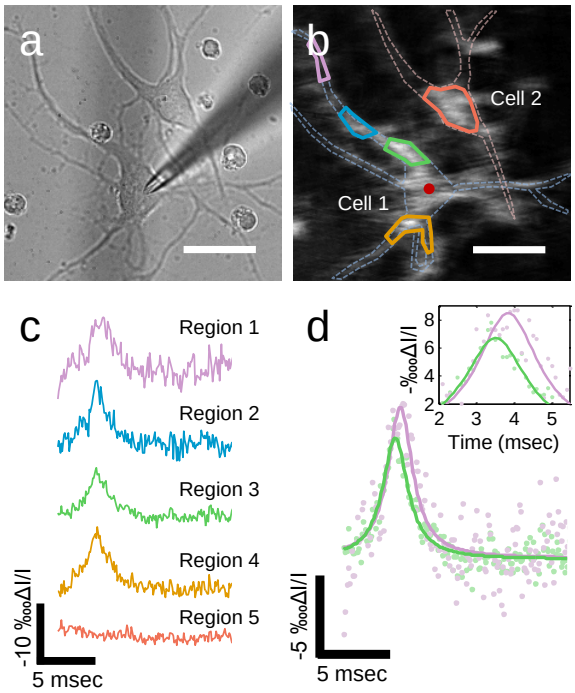

Figure 6-6 Plasmonic Imaging of Action Potential Propagation within a Single Neuron. (a) Optical transmission and (b) plasmonic images of 2 hippocampal neurons, where the dash lines mark the edges of the neurons, and the white dot marks the location of micropipette. (c) Time course of action potential at locations outlined by solid lines with the corresponding colors in b. (d) Comparison of action potential spikes at two locations showing time decay due to finite propagation speed of action potential. The green and orange lines are Lorentzian fitting to the P-EIM data.

To further validate the time delay in the action potentials between different regions of neuron, I recorded a movie of action potential propagation within a neuron with 10-μs temporal resolution. Figure 6-7a shows a few snapshots of the process. From the high-speed movie, I constructed a map of action potential time delay (Figure 6-7b and c). The map allowed me to estimate the propagation speed of action potential in a neuron to be ~ 0.1 m/s inside a single cell, which supports the reported values in literature (Debanne 2004, Kole and Stuart 2008). The map further shows that the time delay does not simply increase with the distance between a particular region and the triggering point.

It has been proposed that the initiation and propagation of action potential are highly dependent on the density of sodium ion channels (Kole, Ilschner et al. 2008). Therefore,

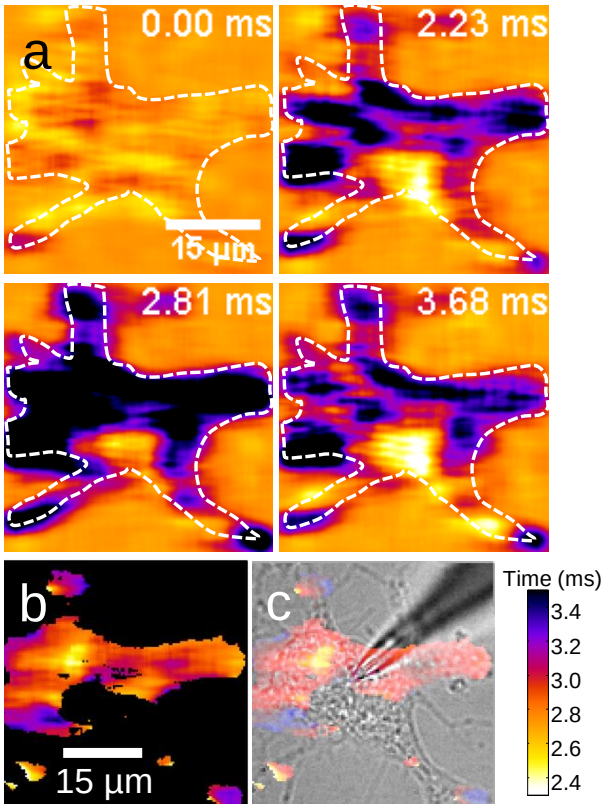

Figure 6-7 Snapshots of Action Potential Propagation

(a) Snapshots of action potential propagation (frame rate: 100,000 fps). (b) Action potential delay map. (c) Overlay of the action potential delay map with bright field image of the neuron.

the spatiotemporal pattern of action potential propagation may be used to map the heterogeneous distribution of sodium ion channels, which could help identify the special function of different regions within a neuron (Korchev, Negulyaev et al. 2000).

High-fidelity single spike detection

In order to resolve single spikes without temporally averaging, I further suppressed the noise by minimizing noise in the optical setup and using a low noise sCMOS camera. Action potentials were evoked by a sequence of short current pulses at a

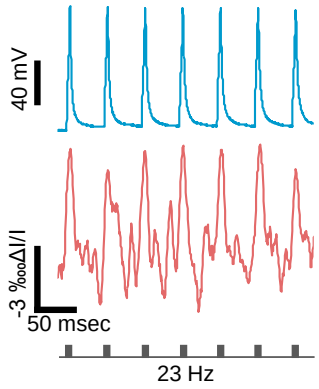

Figure 6-8 Imaging Single Action Potential Spikes
(a) P-EIM (blue), and patch clamp (red) recordings of individual action potential spikes of a neuron triggered with current pulses at frequency of 23 Hz (P-EIM frame rate: 1,600 fps).

frequency 23 Hz. Figure 6-8 shows the action potential spikes recorded with P-EIM (blue), and those recorded simultaneously with patch clamp electrode (red) in a neuron. Despite the remaining noise, individual spikes can be distinguished, which demonstrates P-EIM capability for visualizing individual action potential spikes.

Plasmonic imaging of ion channel activities in neurons

To elucidate ion channel activities, it is useful to follow the ionic current while clamping the voltage. To demonstrate this capability, I recorded ionic current and P-EIM signals simultaneously by depolarizing the neuron with fast voltage pulses. Figure 6-9a shows a current spike by the patch clamp (red), and the corresponding spike by P-EIM (blue). The plasmonic spike has a similar width and temporal response as the electrically recorded ionic current associated with the ionic flow during the opening of ion channels. To confirm the observation, I introduced a Na^+ channel blocker, TTX to the same neuron, and found that both the electrical and plasmonic spikes disappeared in the presence of

TTX (Figure 6-9b). I further confirmed this Na^+ flow-induced plasmonic spike by

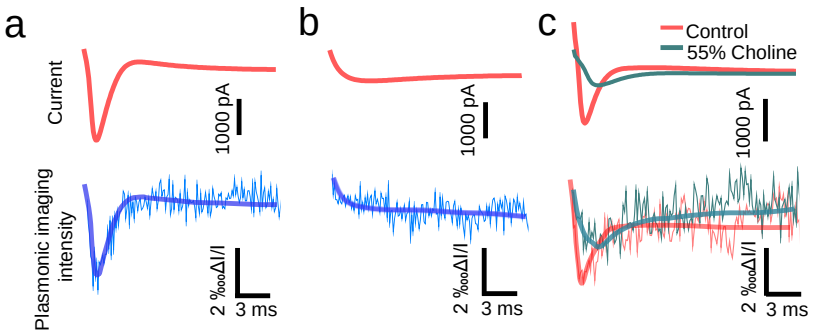

Figure 6-9 Imaging Ion Channel Activities in Voltage-clamp Modes.
(b) Patch clamp (top) and P-EIM (bottom) recordings of an ionic current spike recorded in voltage-clamp mode. (c) Patch clamp (top) and P-EIM (bottom) recordings of ionic current after blocking Na+ ion channels with TTX in voltage-clamp mode. (d) Patch clamp (top) and P-EIM (bottom) recordings of ionic current with (green) and without (red) replacing 55% of the extracellular Na+ by choline cations in voltage-clamp mode. Frame rate for (b-d): 10,000 fps.

replacing the Na^+ extracellular solution with iso-osmotic choline solution. Choline, a cation, is impermeant to the open Na^+ channels, so I expect a reduction in the plasmonic spikes. Indeed, I observed both the current spikes recorded by P-EIM and patch clamp dropped substantially when I replaced the buffer with 55% choline solution (green curves in Figure 6-9c). I also studied the potassium current contribution to the current and plasmonic spikes by inhibiting K^+ channel with 4-Aminopyridine (4-AP). These experiments confirmed that P-EIM is sensitive to Na^+ and K^+ ion fluxes.

Mechanisms of plasmonic imaging of action potential.

Thermodynamics predicts that transmembrane voltage modulates membrane tension leading to mechanical deformation in the membrane(Zhang, Keleshian et al. 2001). The relationship between membrane surface tension and membrane potential for a single interface could be described as: $d\gamma / dV = -q$, known as Lippmann equation,

where γ is the surface tension, V is the membrane electrical potential, and q is the excess mobile charge in the double layer of the membrane surface. Since plasmonic imaging is extremely sensitive to the mechanical deformation, I anticipated that the imaged signal is mainly from subtle morphological change from the cell during the action potential firing (Figure 6-10a). This prediction is supported by literatures. For example, swelling in nerve fibers associated with action potentials was reported(Iwasa, Tasaki et al. 1980). An atomic force microscope (AFM) study revealed voltage-induced mechanical responses in mammalian cells(Zhang, Keleshian et al. 2001). Nanometer scaled displacement in nerve fibers placed between two surfaces was observed with spectral-domain optical coherence phase microscopy (SD-OCT), where the reflection from the top surface served as a reference beam(Akkin, Joo et al. 2007). A more recent report showed that mechanical response of cells could be measured with an elegant piezoelectric nanoribbon transducer(Nguyen, Deshmukh et al. 2012). The AFM and SD-OCT use either a scanning probe or optical beam to measure a mechanical response at one location at time, which cannot map the entire sample simultaneously. The piezoelectric nanoribbon measures the mechanical response of the entire cells, but it is a non-imaging method. In contrast, the present plasmonic imaging technique allows mapping of local mechanical deformation of the entire neuron membrane associated with action potentials and other electrical activities with sub-nanometer detection limit and microsecond temporal resolution(Shan, Patel et al. 2010, Wang, Yang et al. 2012).

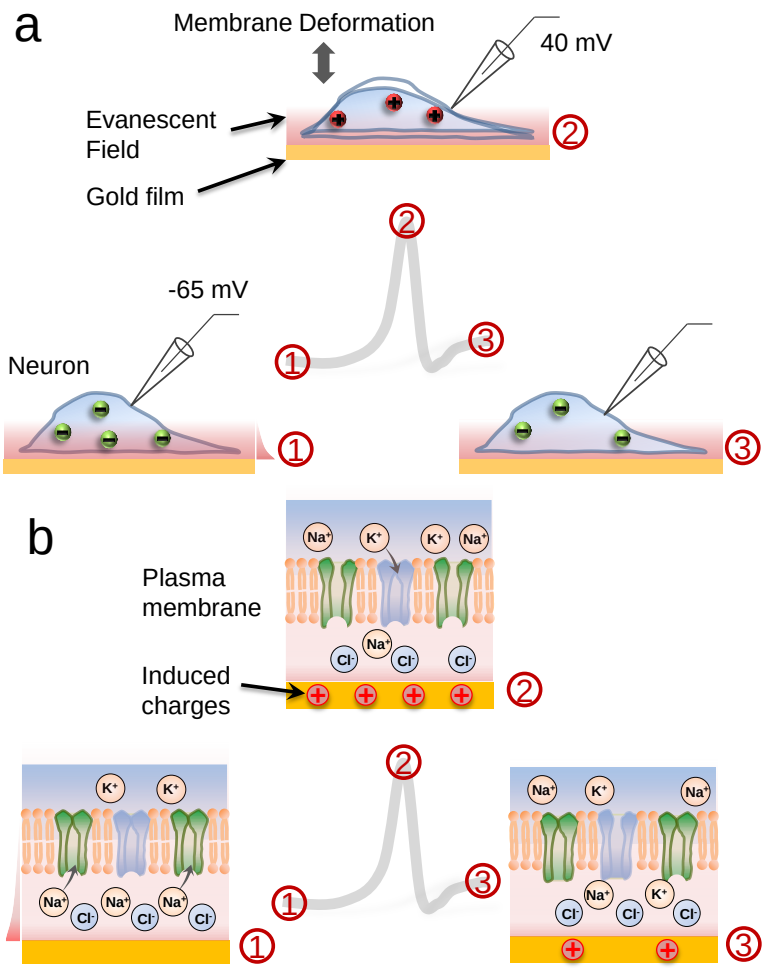

Figure 6-10 Mechanism of Plasmonic Imaging of Action Potential

(a) Deformation mechanism. (b) Electrical mechanism

Although thermodynamics predicts a surface tension change during an action potential, the magnitude of the membrane deformation is governed by cell stiffness and membrane potential(Zhang, Keleshian et al. 2001). To further quantify the cell deformation, I calculated local displacement from modulation amplitude based on intensity decay function along the z-axis. For small plasmonic intensity change ΔI, the fractional intensity change, $\Delta I/I$, is linear with displacement change Δz over decay constant λ. I experimentally verified that the intensity decay constant along the z-axis is

about 100 nm, which is close to theoretical simulation result(Shan, Fang et al. 2014, Yang, Yu et al. 2015). Therefore, with a typical 0.3-1‰ intensity change was observed for 100 mV depolarization, the associated membrane deformation is estimated to be 0.03-0.1 nm per 100 mV, which is corresponding to 0.075-0.2 mDeg resonance angle shift.

Note that associated with the action potential is the opening and closing of sodium and potassium ion channels, which change the local concentrations of sodium and potassium ions, in addition to membrane mechanical deformation. Since the plasmonic imaging is also sensitive to refractive index change near the surface, the change of local ionic concentrations may also lead to a change in the plasmonic image intensity. However, the corresponding change in the plasmonic image intensity is estimated to be at least 5 folds smaller (Materials and Methods). This consideration rules out local concentration change in the sodium and potassium ions as the imaging mechanism of the observed action potential.

Local charge density change induced by action potential may also affect the resonance frequency of surface plasmons, as plasmonic imaging is also sensitive to surface charge density (Figure 6-10b) (Foley, Shan et al. 2008, Wang, Foley et al. 2011). However, the similarity in the shapes of plasmonic intensity profile and membrane potential measured by patch clamp rules out the possibility that the imaged signal comes directly from extracellular recording, which should display a temporal derivative shape of the intracellular signal. On the other hand, the field-induced charge on the surface that is originated from intracellular action potential may also affect the gold chip and contribute to the imaged signal. However, the corresponding change in the plasmonic image intensity was estimated to be at least 5 folds smaller than the experimental value

(Materials and methods). It also predicts a positive intensity response for depolarization induced surface charge, which is opposite to the observation in both external modulation and spontaneous action potential firing cases. Therefore, the electrical mechanism may not be a dominant contribution to the plasmonic signal.

The membrane deformation model indicates that softer membrane will lead to a larger deformation. To examine this prediction, I measured neurons treated with cytochalasin D, which is known to soften the cell by inhibiting polymerization of the actin, the major component of the cytoskeleton(McDowell, Ellerbee et al. 2007). I indeed observed that the change in the plasmonic image intensity associated with action potential in cytochalasin D-treated neurons is ~20% larger than that of the control neurons (Figure 6-11). Thus, I conclude that the mechanical deformation of the cells accompanied with membrane potential is main driving mechanism for the optical signal.

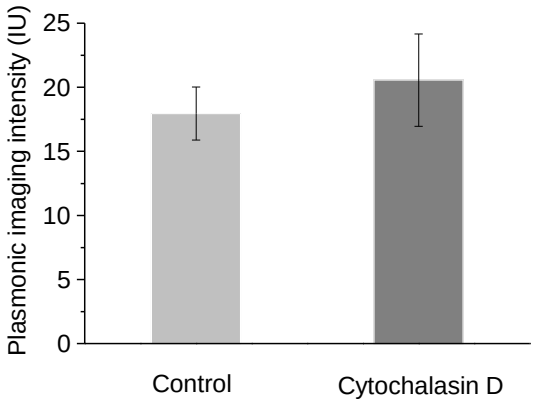

Figure 6-11 Effect of CD, an Actin Polymerization Inhibitor, on the Plasmonic Signals. 5 CD-treated and 10 control neurons were studied.

Conclusion

I have demonstrated a new principle to record action potential in single mammalian neurons optically by detecting membrane mechanical deformation with a plasmonic imaging technique. The imaging technique clearly resolves the individual action potential spikes with width and shape closely resemble those simultaneously recorded with the traditional patch clamp technique. This method is label-free and removes the possible effects of the labeling on the native functions of the neurons. This capability, together with the high spatial resolution, allows me to image the fast initiation and propagation of action potential in single neurons at subcellular level. The imaging setup is fully compatible with the traditional patch clamp recording and fluorescence microscopy, allowing the study of the same sample with multiple techniques. Although the present work is focused on cultured neurons as an effort to demonstrate the imaging capability, researchers can expand it to study neuronal networks *in vivo* by integrating it with the optotrode techniques(Kim, McCall et al. 2013, Caucheteur, Voisin et al. 2015). Currently, the signal-to-noise level is marginally sufficient for imaging signal action potential, various signal enhancement strategy may apply for better imaging quality. With the merit of non-perturbation to the target cells, I anticipate that the plasmonic recording technique will contribute to the understanding of action potential firing pattern formation and transition for the same cell during long-term monitoring and return the cell native state.

CHAPTER 7 IMAGING MECHANICAL WAVES THAT ACCOMPANY ACTION POTENTIAL IN MAMMALIAN NEURONS

Mechanical waves may accompany the action potential and play functional roles in neurons, but measuring the subtle mechanical waves in single mammalian neurons has been a challenge. Here I report an optical method to image membrane displacement in mammalian neurons with sub-micron spatial resolution and sub-ms temporal resolution, and quantify the displacement with sub-nm detection limit. I show that mechanical waves do accompany the action potential in mammalian neurons, and their shape and width are similar to those of the action potential. The amplitude of the mechanical wave varies from neuron to neuron, ranging from 0.2 - 0.4 nm. There is also a large variability in the local membrane displacement within a neuron. The basic phenomenon is consistent with theories, but the shape and variability of the mechanical waves call for further investigations.

Introduction

Action potentials (APs) play a central role in neuronal communication(Hodgkin and Huxley 1952). While most of the efforts to date have focused on recording the AP as an electrical signal, theoretical and experimental evidence has suggested that the AP is accompanied by a mechanical response, and the interplay between the electrical and mechanical responses is relevant to physiological functions of neurons(Bezanilla 2002, Martinac 2004, Coste, Mathur et al. 2010, Mueller and Tyler 2014). Despite the importance, the mechanical response is much less studied compared to the electrical signal. Here I describe a method to image mechanical responses in single neurons with sub-micron spatial resolution, sub-ms temporal resolution and sub-nm detection limit. Using this method, I image local mechanical waves that accompany the AP in single mammalian neurons. I compare the mechanical waves with the simultaneously recorded AP waves by the patch clamp electrophysiological method. I study neuron-to-neuron variability, and also local variability within a neuron in both the amplitude and direction of the membrane displacement. I compare the experimental results with theories.

Recent theories predicted that linear and non-linear (e.g., solitons) mechanical waves accompany AP propagation along the axonal membrane(Heimburg and Jackson 2005, El Hady and Machta 2015), and experiments observed mechanical responses in animal nerve fibers(Hill, Schubert et al. 1977, Iwasa, Tasaki et al. 1980, Tasaki and Iwasa 1982, Tasaki and Byrne 1988, Tasaki and Byrne 1990). However, detecting them in single mammalian neurons is challenging because the mechanical response is expected to be on the order of sub-nm, and live neurons move constantly due to thermal fluctuations and metabolic activities. To study the transient and local mechanical responses that

accompany the AP, the measurement must also have high temporal (millisecond) and spatial (microns) resolutions. Atomic Force Microscope (AFM)(Mosbacher, Langer et al. 1998, Zhang, Keleshian et al. 2001, Kim, Kosterin et al. 2007, Pamir, George et al. 2008), piezoelectric nanoribbons(Nguyen, Deshmukh et al. 2012) and various optical approaches(Cohen and Keynes 1971, Hill, Schubert et al. 1977, Ross, Salzberg et al. 1977, Iwasa, Tasaki et al. 1980, Akkin, Joo et al. 2007, Oh, Fang-Yen et al. 2012)have been developed to measure small mechanical responses in cellular membranes, but imaging subtle mechanical waves that accompany the AP in mammalian neurons with high temporal and spatial resolutions has been difficult.

To detect the mechanical waves that accompany the AP, I developed a method to track the membrane displacement of a neuron with an inverted optical microscope using a differential detection algorithm (Figure 7-1a)(Guan, Shan et al. 2015). I cultured rat hippocampal neurons on poly-D-lysine coated glass coverslip placed on the objective of the microscope. To initiate the AP, I patched the neuron with the standard patch clamp technique, recorded the electrical signal and imaged the associated membrane displacement simultaneously with the differential detection algorithm described below (Figure 7-1b).

The optical image reveals the individual neurons, and zooming-in of a neuron shows the edge of the neuron. I selected a rectangular region of interest (ROI) that includes the edge, and divided the ROI along the edge into two equal halves, one half is inside of the neuron, and the second half falls outside of the neuron (Figure 7-1b). I denote the intensities of the two halves as I_1 and I_2, respectively. If the neuron expands, then I_1 decreases and I_2 increases. Conversely, if the neuron shrinks, then I_1 increases and

I_2 decreases. The membrane displacement is proportional to $(I_1-I_2)/(I_1+I_2)$ within a displacement range of several hundred nm (Figure 7-2). I determined the range, and calibrated the relation between the displacement and normalized differential intensity, $(I_1-I_2)/(I_1+I_2)$, using the procedure described in Methods and Materials.

By measuring the normalized differential image intensity, $(I_1-I_2)/(I_1+I_2)$, within each ROI, I obtained the local membrane displacement at every location along the edge of the neuron (Figure 7-1b). The spatial resolution of the method is limited by optical diffraction, which is ~0.4 μm in the present case (numerical aperture of the subjective is 0.65). Compared to AFM that measures one location at a time, the present method is fast and allows multiple neurons and different regions of the same neuron to be imaged simultaneously. The differential detection algorithm reduces common noise, such as light intensity fluctuations, which leads to a detection limit of 0.2 nm of membrane displacement with a denoising scheme detailed in Methods and Supplementary Information.

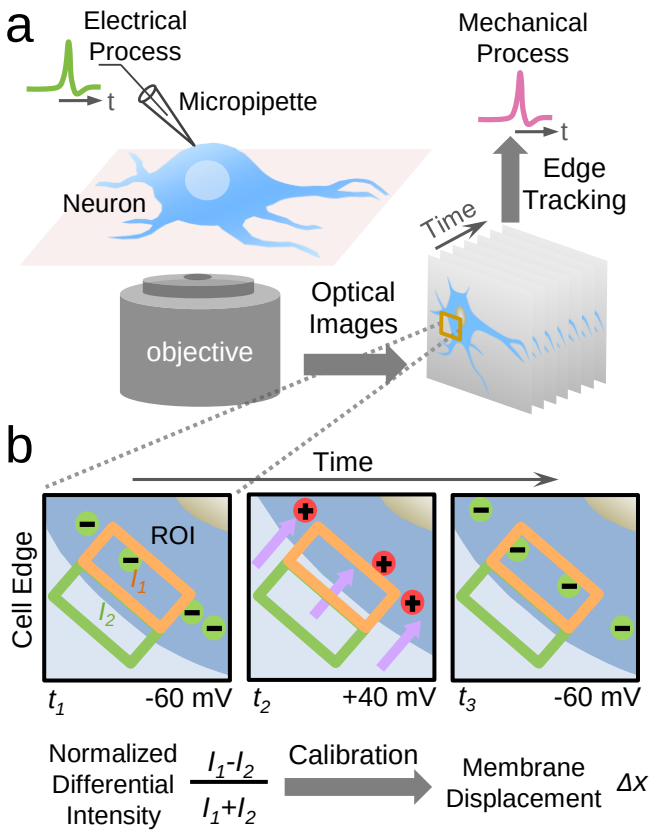

Figure 7-1 Optical Imaging of Mechanical Wave that Accompanies Action Potential in Single Mammalian Neurons.

a) Experimental setup showing a hippocampal neuron cultured on a glass slide mounted on an inverted optical microscope, which is studied simultaneously with the patch clamp configuration for electrical recording of the action potential, and optical imaging of membrane displacement associated with the action potential. b) Imaging and quantification of membrane displacement with a differential detection algorithm that tracks the edge movement of a neuron. A region of interest is selected to include a portion of the neuron edge, and divided into two halves along the edge (orange and green boxes) with intensities, I_1 and I_2, respectively. The expansion or shrinking of the neuron is measured by a membrane displacement, Δx, from the change in the intensities, which is proportional to the normalized differential intensity, $(I_1-I_2)/(I_1+I_2)$. See text for details.

Materials and Methods

Optical imaging of membrane displacement

The membrane displacement was measured with an inverted optical microscope (IX81) using a 60x objective (NA = 0.65), a halogen lamp in the Köhler configuration, and a sCMOS camera (Hamamatsu, Flash 4.0) for imaging. To image the membrane displacement in HEK293T cells, the camera was operated with a frame rate of 400 fps, and pixel density of 256 x 512 (2 pixel binning mode). To image action potential-induced mechanical waves in neurons, the frame rate of the camera was increased to 1603.5 fps with pixel density of 128 x 512. Images were streamed to a fast disk array consist of 4 solid-state hard disks (Samsung 840 Pro 512GB) in parallel writing mode (RAID 0). To minimize the shot noise, the image intensity captured by the camera was adjusted close to camera saturation. To synchronize the electrical recording with images, the camera was externally triggered by the patch clamp system. The whole setup was placed on a floating optical table (Newport RS2000) and enclosed in a custom built faradic cage and acoustic enclosure to minimize electrical and mechanical noises.

Electrophysiological recording

Electrophysiological signals were recorded in the whole-cell configuration using Axopatch 200B amplifier (Axon Instruments). To image membrane displacement in HEK293T cells, membrane potential was modulated sinusoidally in the voltage-clamp mode with typical frequency of 23 Hz for 10 seconds (otherwise indicated in manuscript). For action potential imaging in hippocampal neurons, multiple depolarization current pulses (typically 500 pA, 2-4 msec) were injected into the cell to evoke action potential trains at 23 Hz for 20 seconds (otherwise indicated in manuscript). Glass micropipettes

were prepared with a pipet puller (P-97, Sutter Instrument) with typical resistance of 3-8 MΩ. Before patching a cell, the micropipette was filled with intracellular recording solution consisting of 10 mM NaCl, 135 mM K-gluconate, 10 mM HEPES, 2 mM MgCl2, 2 mM Mg-ATP and 1 mM EGTA (pH 7.4). Cells and neurons were recorded in extracellular recording solution, containing 135 mM NaCl, 5 mM KCl, 1.2 mM MgCl2, 5 mM HEPES, 2.5 mM CaCl2 and 10 mM glucose at pH 7.4. The electrical signals were filtered by a 1 kHz low-pass Bessel filter.

Cell and neuron culture

Wildtype HEK293T cells (ATCC, CRL-3216) were seeded on a fibronectin (Sigma-Aldrich, f1141) coated petri dish one day before the experiment. Cells were cultured in DMEM (Lonza) medium with 10% FBS (Life Technologies, 10437077) according to the user's manual from ATCC. E18 rat hippocampus (Brainbits) were dissociated with papain and seeded on a poly-D-lysine (Sigma, P6407) coated glass coverslip at a density of ~105 neurons/cm2. After incubation in growth medium (NbActive4, Brainbits) in 5% CO2 humidified atmosphere at 37°C for 5-8 days, the neurons were ready for experiment.

Differential detection algorithm

The optical images were first interpolated five times in size by adding additional pixels. The image size represented by each pixel size was determined by dividing the physical dimension of the pixel in the sCMOS imager (6.5 μm, Hamamatsu Flash 4.0) with the optical zoom and digital interpolation in the system. An ROI with a typical size of 100 x 100 pixels (2.2 μm x 2.2 μm) was selected at one location at the cell edge and split into two halves, one inside (I_1) and one outside (I_2). To calibrate the response of

normalized differential intensity with displacement, the ROI was shifted by a certain number of pixels in the direction perpendicular to the edge (Figure 7-2). Normalized differential intensity, $(I_1-I_2)/(I_1+I_2)$, vs. pixel shift (displacement) showed a typical "S" shape (Figure 7-2). Within a certain range (marked between two dashed lines in Figure 7-2d, ~500 nm), the differential intensity change is linearly proportional to the pixel shift (displacement). I determined the slope of the linear region, and used it as the calibration factor to determine the membrane displacement with the differential detection algorithm (Figure 7-2e). For all the measurements performed in this work, the membrane displacement is small (less than few tens of nm), well within the linear region (Figure 7-3d).

For both HEK293T cells and hippocampal neurons, cell edges were manually identified, and the local membrane displacement was determined using the procedure described above. Note that the differential detection algorithm is insensitive to the accuracy of the edge identification as long as the edge falls within the ROI, and the displacement is within the linear rage (~500 nm) as shown in Figure 7-2e. After quantifying the displacement at one location, the ROI automatically stepped to an adjacent location, and the procedure was repeated until the displacement along the edge of the entire cell was determined. In the case of HEK293T cells, the ROI was stepped every 10 degrees to the centroid of the cell (average ~1.7 μm/step along the edge for 10 μm cell in radius). For neurons, the ROI was stepped every 64 pixels along the boundary (~1.4 μm/step for 60x zoom). It took about 5 mins to complete the analysis of one cell with the method, and it can be further optimized in the future.

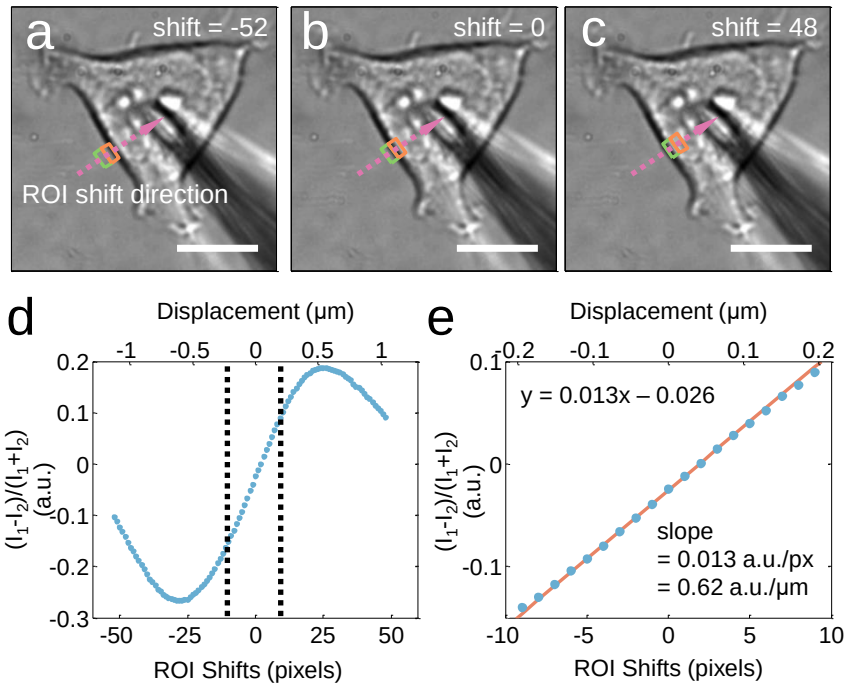

Figure 7-2 Calibration Procedure of Differential Algorithm

a-c) A ROI at the cell edge is shifted towards inside of the cell pixel by pixel. d) Normalized differential intensity profile $(I_1-I_2)/(I_1+I_2)$ vs. ROI positions (in pixels and μm). e) Zooming-in of the region between two vertical dashed lines in d) displaying a linear dependence, where the red line is linear fitting. Scale bar: 10 μm.

Denoising scheme and difference image

To resolve the subtle mechanical displacement, denoising procedures were applied to measurements of both HEK293T cells and hippocampal neurons. In the HEK293T experiment, because a sinusoidal potential was used to modulate the membrane, Fast Fourier Transform (FFT) filter was used to remove noise at frequencies other than the modulation frequency for each ROI (Supplementary Information). The amplitude and phase at the modulation frequency were quantified as magnitude and direction of the edge displacement while membrane potential depolarized.

To obtain the time difference image of the cell, FFT filter was applied to the image stack over time pixel by pixel. Since the mechanical response is in phase (0 or 180 degrees phase shift) with the applied potential modulation, real part image at the lock-in frequency was selected as the time difference image (the imaginary part measured response in +/-90 degrees). Mathematically, the time difference image (quantify the temporal information first) is equivalent to the differential detection scheme (quantify the spatial information first, then denoising along temporal dimension), and it provides a convenient way to visualize the membrane displacement, both in direction and amplitude. Images were spatially smoothed with 3×3 pixels (0.33×0.33 μm) mean kernel before FFT filtering.

For hippocampal neurons, repeated APs were evoked with typically 100-400 cycles. Both electrical signal and images were averaged over the repeating cycles, and averaged signal for single cycle was obtained. To observe the mechanical wave, time difference images were obtained by subtracting the first image from the averaged image stack. Mechanical displacement was quantified using the differential detection algorithm along the edge as described earlier from the averaged image stack. To remove spatial noise, the mean image stack was temporally detrended pixel-by-pixel using a fitted linear function, and digitally filtered with FIR low-pass filter with a cut-off frequency of 500 Hz.

Displacement quantification and data analysis

Local membrane displacement map was obtained by interpolating local displacement quantified by the differential detection algorithm. The displacement power spectral density and standard deviation between 20 – 200 Hz were quantified as the noise

level. All post-acquisition analysis was carried out by custom-written MATLAB (Natick, MA, USA) code.

Results and Discussion

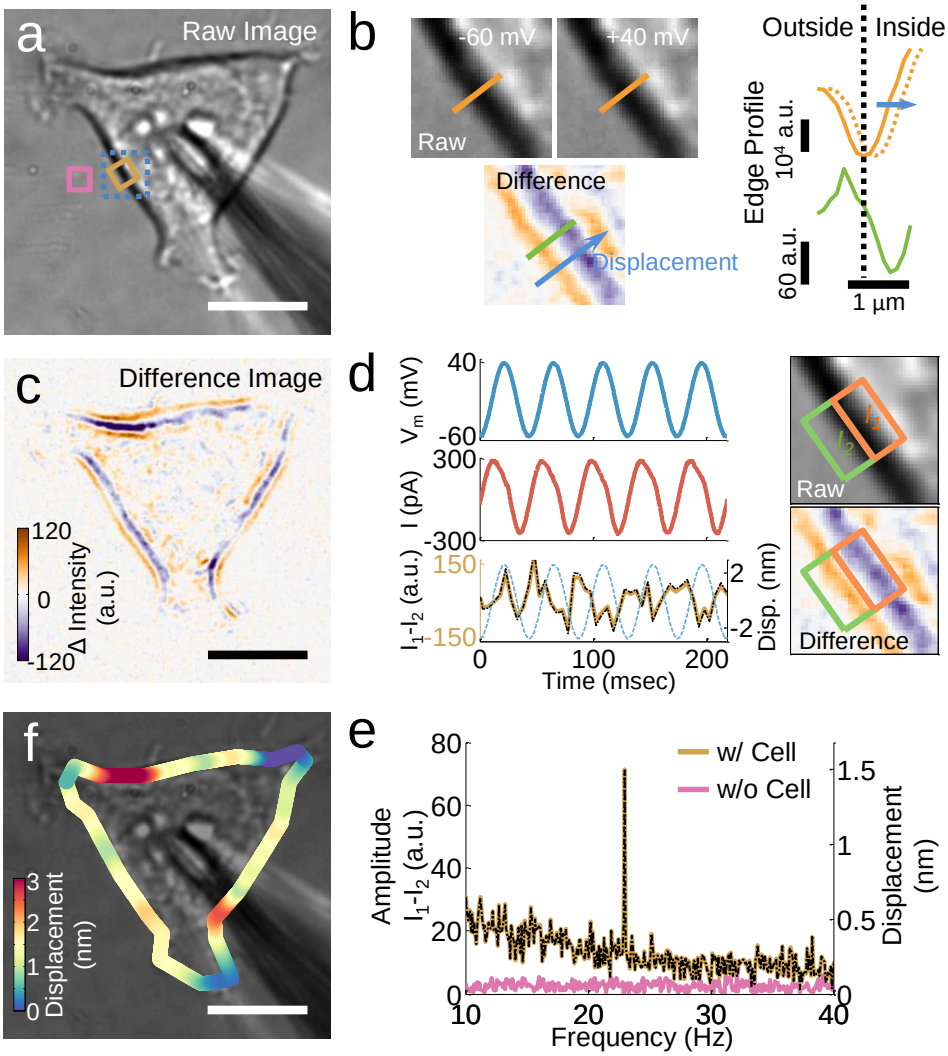

Optical imaging of membrane potential-induced membrane displacement

I first examined the method by applying it to measure membrane potential-induced mechanical displacement in HEK293T cells. For this purpose, I modulated the membrane potential of a HEK293T cell sinusoidally in the whole-cell patch clamp configuration, and recorded the electrical current and optical images simultaneously (Figure 7-3a). Figure 7-3d shows the current response (middle panel, red trace) to an applied potential modulated from -60 mV to 40 mV with frequency of 23 Hz (top panel,

Figure 7-3 Quantification of Membrane Depolarization-induced Membrane Displacement in Cells.

a) Bright field image of a HEK293T cell and a micropipette used to change the membrane potential. b) Left panel: Zooming-in of the bright field images (grey scale) of the cell edge at -60 and 40 mV, and difference image (colored) obtained by subtracting the bright field image obtained at -60 mV from that at 40 mV. The characteristic orange and purple lines represent the cell edge displacement. Right panel: Corresponding intensity profiles along lines indicated in the images, where the solid and dashed orange lines are from the bright field images at -60 mV and 40 mV, and the solid green line is from the difference image. c) Difference image of the entire cell showing cell edge displacement and local variability (intensities for the orange and purple bands) of the displacement. d) Left panel: Time traces of applied potential at frequency 23 Hz (blue), measured current (red) from the patch clamp setup, and differential intensity (I_1 -I_2, brown) from the optical imaging method. Note that the actual displacement determined from the differential detection algorithm is shown as a black line overlaid on top of the differential intensity, and the potential is indicated as dashed blue line. Right panel: A region of cell edge shown in raw bright field (grey scale) and difference (colored) images. e) Fast Fourier Transformation (FFT) power spectra of differential intensity in regions with (brown) and without (pink) cell (as indicated as colored squares in a). The FFT power spectrum of the membrane displacement is shown as a black dashed line. f) Membrane displacement map obtained from the differential detection algorithm. **Scale bar** in a, c, f): 10 μm.

blue trace). The current is due to polarization, as no AP is excited in HEK293T. This is also confirmed by the 90°-phase shift between the applied membrane potential and measured current. Associated with the membrane potential modulation, I expect a membrane displacement according to the thermodynamic theories that predict different effects, including piezoelectricity and flexoelectricity (Petrov 2006, Mosgaard, Zecchi et al. 2015). The membrane displacement is too small to be visualized directly from the

bright field optical image. For example, Figure 7-3b are two images of the cell edge (marked blue dashed line in Figure 7-3a) recorded at -60 and 40 mV, which show no visible difference. However, difference image obtained by subtracting the image at -60 mV from that at 40 mV shows clear contrast of the cell edge with an orange and a purple bands in Figure 7-3b, corresponding to an increase and decrease in the image intensity,

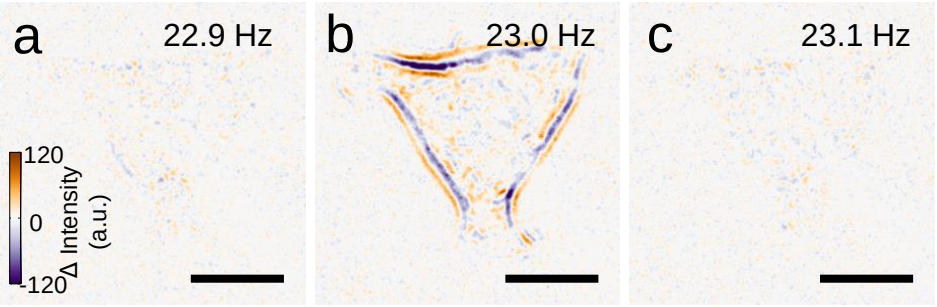

Figure 7-4 Difference Images at Different Frequencies

a-c) Difference images at the modulation frequency b) and nearby frequencies a) and c). Scale bar: 10 μm.

respectively (see Methods for obtaining difference image). This distinct contrast in the difference image reflects a membrane displacement, which can be understood by plotting intensity profiles across the cell edge at -60 (solid orange line) and 40 mV (dashed orange line). The difference between the two intensity profiles is simply a lateral displacement (Figure 7-3b). Subtraction of the two intensity profiles leads to regions with increased or decreased intensity, which gives rise to the orange and purple bands in the difference image.

The analysis above demonstrates that the potential-induced membrane displacement can be visualized by the difference image. Figure 7-3c is the difference image of the cell shown in Figure 7-3a, revealing contrast with the characteristic purple and orange bands along the cell edge. According to the differential detection algorithm,

the intensities of the purple and orange bands are I_1 and $-I_2$, which provide membrane displacement. The upper right of Figure 7-3d shows a ROI at a cell edge, with a half inside (I_1) and another half outside (I_2) of the cell, and the lower right of Figure 7-3d is

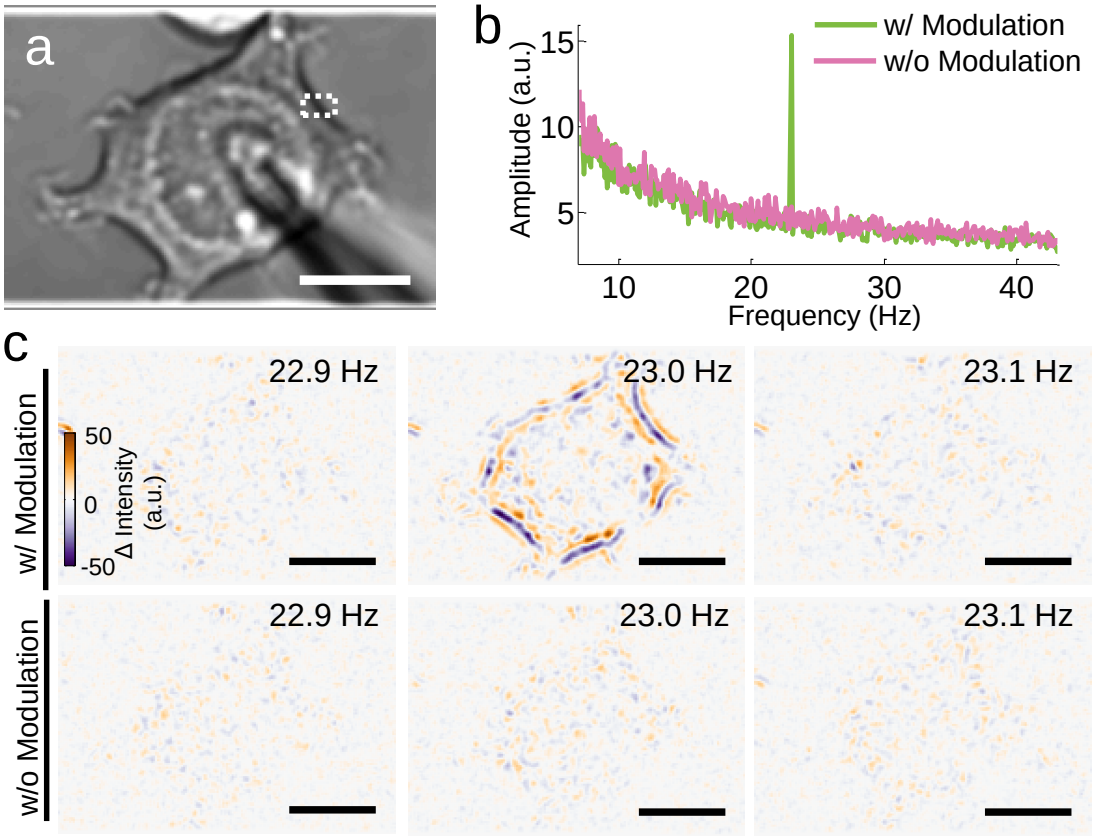

Figure 7-5 Cell Membrane Displacement with and without Membrane Potential Modulation

a) Optical image of a patched HEK293T cell. b) FFT power spectra of the same cell with (green) and without (pink) potential modulation at 23 Hz. c) Difference images of the cell with (top) and without (bottom) modulation at the modulation frequency and nearby frequencies. Scale bar: 10 μm.

the difference image of the same region. I_1-I_2 is the sum of the purple and orange bands in the difference image, which is proportional to the membrane displacement. Figure 7-3d (lower left panel) plots I_1-I_2 vs. time, showing a periodic oscillation due to membrane

depolarization-induced cell edge movement. Fast Fourier Transform (FFT) of the I_1-I_2 trace reveals a pronounced peak at 23 Hz, the frequency of membrane potential modulation (Figure 7-3e). The peak amplitude in the FFT spectrum provides an accurate measurement of the membrane displacement. The FFT analysis also reveals a 180° phase shift between the membrane potential and displacement, indicating that the cell edge shrinks as the membrane depolarizes.

I validated the above results by carrying out further control experiments and analysis. First, I did not detect any peak at the frequency of modulation in the FFT spectrum in regions without the cell (pink line, Figure 7-3e), indicating that the image intensity change at 23 Hz is due to the mechanical response of the cell to the membrane potential modulation. Second, I did not detect any peak in the FFT spectrum in the cell region when I turned off the membrane potential modulation (Figure 7-5), which demonstrates that the observed membrane displacement was truly originated from the membrane potential modulation. Finally, I detected little signals at frequencies other than the modulation frequency in the FFT spectrum, which shows that the measured potential-induced membrane displacement has sufficient signal-to-noise ratio compared to the background micro-motions of the cell arising from thermal fluctuations and metabolic activities (Figure 7-4).

Quantification of membrane potential-induced mechanical response

The analysis above shows that subtle cell membrane displacement can be visualized in the difference image, and measured by tracking the image intensity change along the cell edge with the differential detection algorithm. To quantify the displacement, I performed calibration using the procedure described in Methods and

Supplementary Information (Figure 7-2). The calibration allowed me to determine the local membrane displacement from the differential image intensity, $(I_1 - I_2)/(I_1 + I_2)$. Scale bars in Figure 7-3d and Figure 7-3e show the membrane displacement of the region shown in Figure 7-3a. The membrane displacement is about 1.5 nm, corresponding to 15 pm per mV. The signal to noise ratio (SNR) is ~7, as determined from the peak amplitude at the modulation frequency, and the background level near the modulation frequency, which leads to a noise level of ~0.2 nm of the region. The averaged displacement along the edge of the cell is ~1.4 nm. This number is consistent with model estimate based on the Lippmann equation (Zhang, Keleshian et al. 2001).

Because different regions of a cell have different membrane displacements, I plotted the local membrane displacement of a cell in Figure 7-3f, showing large variability in membrane displacement along the cell edge. Some regions displace by as many as several nm (red), while other regions by only a fraction of nm (dark blue). Heterogeneity in cellular membrane is well documented in literature, including expression level of membrane proteins, type of lipids and structure of cytoskeleton, which play various functional roles in the cell (Fletcher and Mullins 2010). The present study reveals large heterogeneity in the membrane potential-induced mechanical response(Kuznetsova, Starodubtseva et al. 2007).

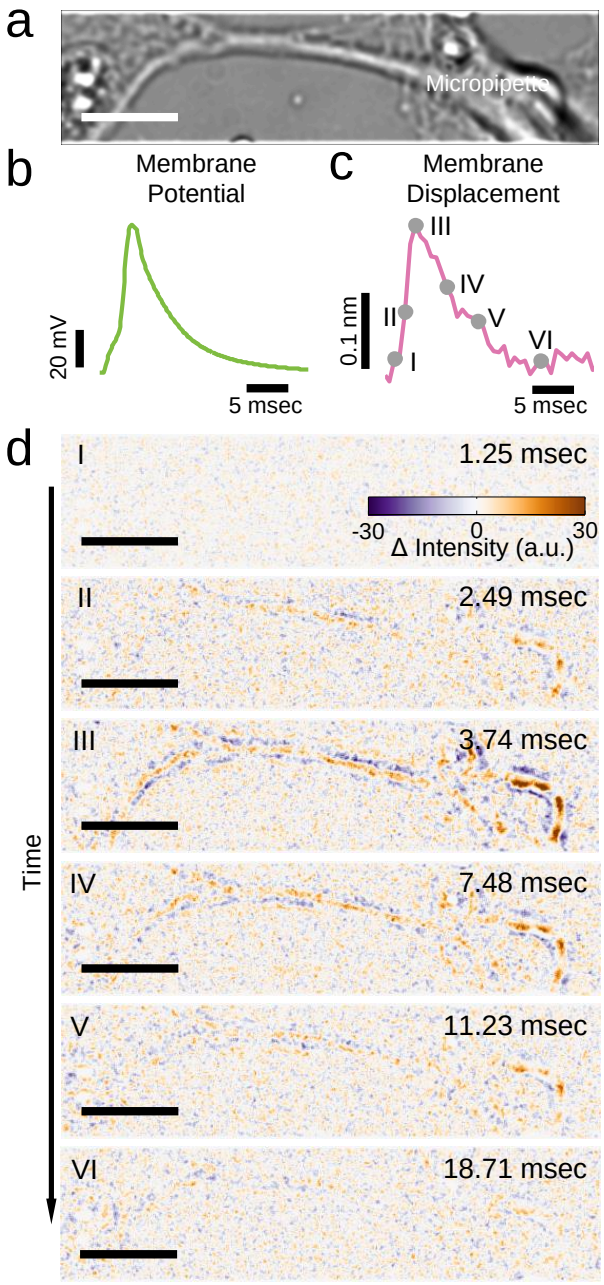

Figure 7-6 Detection of Mechanical Waves in Neurons Accompanying the Action Potential.

a) Bright field image of a hippocampal neuron. b) Action potential of the neuron (green). c) Simultaneously recorded membrane displacement of the same neuron (magenta). d) Snapshots of difference images of the hippocampal neuron at different stages of the action potential spike. The moments where the difference images were recorded are indicated by filled grey circles in c). Scale bar: 10 µm.

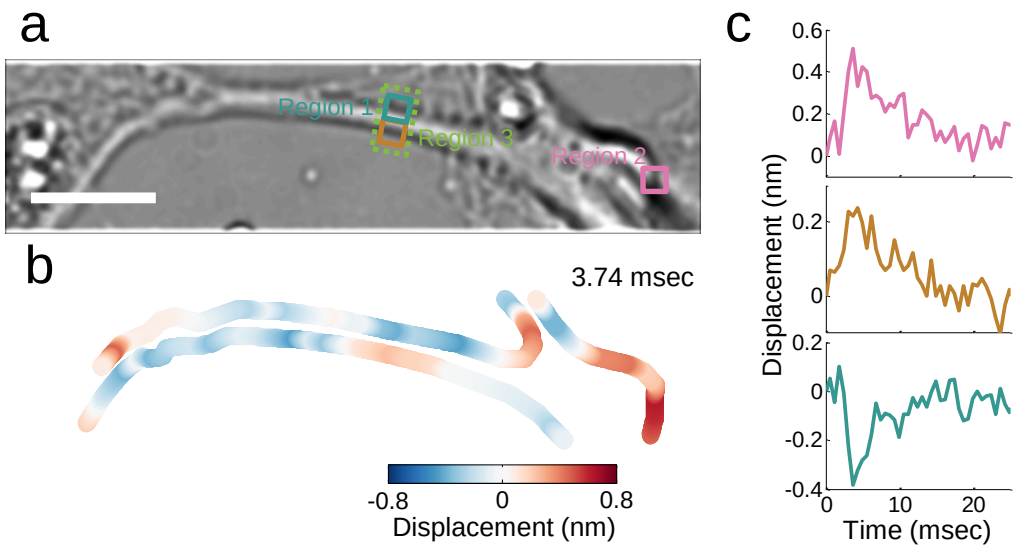

Figure 7-7 Mapping and Quantification of Local Membrane Displacement Associated with the Mechanical Wave.

a) Bright field image of a hippocampal neuron. b) Local membrane displacement map at the peak of the action potential, where red indicates outward displacement, blue indicates inward displacement. c) Mechanical waveforms at locations indicated by the corresponding colored squares in a). Scale bar: 10 μm

Imaging of mechanical waves that accompany action potential

I have demonstrated that potential-induced membrane displacement in cells can be imaged with sub-micron spatial resolution, and quantified with sub-nm precision. I now turn to the detection of mechanical waves that accompany the AP in primary neurons. I first identified a neuron with the bright-field optical microscope, and patched it with the patch clamp setup (Figure 7-6a). I then triggered the AP by injecting current into the neuron with the patch clamp micropipette, and recorded both the electrical potential (Figure 7-6b), and a stack of optical images with a frame rate of 1603 fps. To visualize the mechanical response, I obtained difference images by subtracting the first image from each of the images in the stack (see Methods). The difference images can be viewed as a

movie (Supplementary Information), which shows the transient mechanical response of the neuron during the AP. From the video, I can visualize the AP initiation and progression in the regions of axons and dendrites. This spatial information is not previously accessible by the traditional electrical recording or other methods.

Figure 7-6d shows a sequence of difference images captured at different stages of the AP (marked on Figure 7-6c). Before firing of the AP, the difference image is featureless (Figure 7-6d, I). As the AP rises, the difference image begins to show contrast (Figure 7-6d, II), and the image contrast reaches a maximum at the peak of the AP (Figure 7-6d, III). When the AP falls, the difference image contrast also decreases (Figure

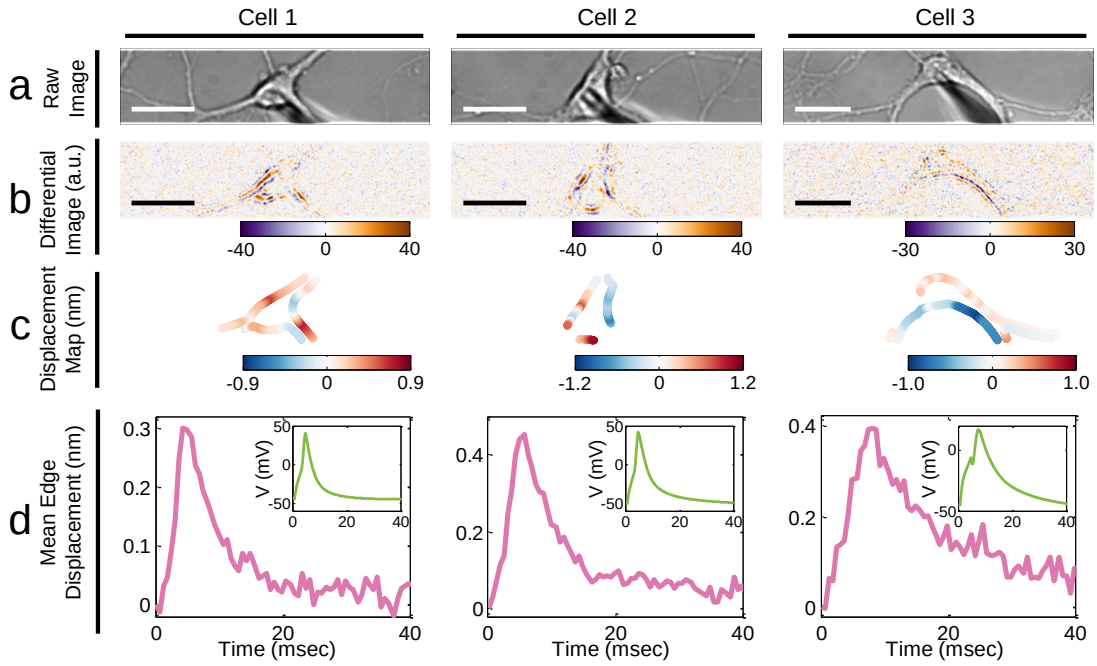

Figure 7-8 Heterogeneous Mechanical Responses of Neurons.
Bright field images (a), difference images (b), local membrane displacement maps (c) and mean membrane displacement profiles (d) of three hippocampal neurons during action potential firing. The simultaneously recorded corresponding action potential profiles for the neurons are presented in the insets of (d). Scale bars: Cell 1 and Cell 2: 15 μm; Cell 3: 20 μm.

7-6d, IV, and V), and eventually disappears to the background noise level (Figure 7-6d, VI). Note that the purple and orange bands in the difference images in Figure 7-6d

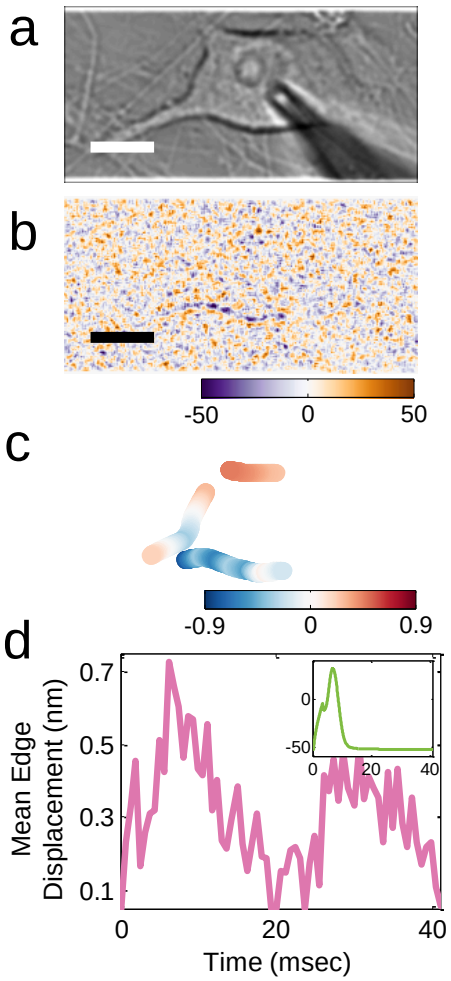

Figure 7-9 Mechanical Wave in Dorsal Root Ganglion (DRG) Neurons
Bright field image a), difference image b), displacement map c) and mean displacement magnitude d) (pink curve) of the DRG neuron mechanical response. Inset in d) shows the action potential. Scale bar: 10 μm.

represent decrease and increase in the image intensity, which is expected for the membrane displacement (expansion or shrinking) as I discussed earlier.

I quantified the membrane displacement using the differential detection algorithm and obtained the overall transient mechanical deformation during the AP. To clearly

resolve the small membrane displacement in the presence of micro-motion of the mammalian neurons, I evoked the AP repeatedly and obtained the average transient membrane displacement (Figure 7-6c), which shows that accompanying the AP, there is membrane displacement with waveform similar to that of the AP (see Methods and Supplementary Information for the procedure). The maximum amplitude of the membrane displacement takes place at the peak of the AP and is ~0.2 nm (at ~90 mV depolarization potential). A recent theory based on linear mechanics predicted an AP induced membrane displacement in neurons(6). For hippocampal neurons, the theory estimates that the maximum membrane displacement that accompanies the AP is ~0.1 nm, which is close to the present observation. However, the predicted mechanical waveform contains an oscillatory feature with a small negative displacement region followed by a more dominant positive displacement region, which is in contrast to the present observation that mechanical and electrical waveforms are similar. The observed mechanical waveform appears to resemble more closely with that of the soliton model(Heimburg and Jackson 2005, Andersen, Jackson et al. 2009, Shrivastava and Schneider 2013, Shrivastava and Schneider 2014).

The observation of membrane displacement with amplitude of ~0.2 nm shown in Figure 7-6c is an averaged value over the entire neuron. The optical method here also provides valuable local information, which reveals large variability in the local membrane displacement, not only in the amplitude but also the polarity. Figure 7-7b shows the local displacement along the edge of a neuron (see Figure 7-7a for the optical image). In some regions (e.g., region 1), the displacement is negative (blue, cell membrane moves inward), indicating shrinking of the neuron. In other regions (e.g.,

region 2), however, the displacement is positive (red, cell membrane moves outward), which is expected for expansion or swelling of the neuron. There are also regions (e.g., region 3) showing positive displacement on one side and negative displacement on the opposite side, suggesting a displacement of the entire section of the neuron in one direction. Figure 7-7c plots the membrane displacement waveforms at different locations. Despite the polarity difference, the waveforms are similar in shape to each other, and also to the electrically recorded AP.

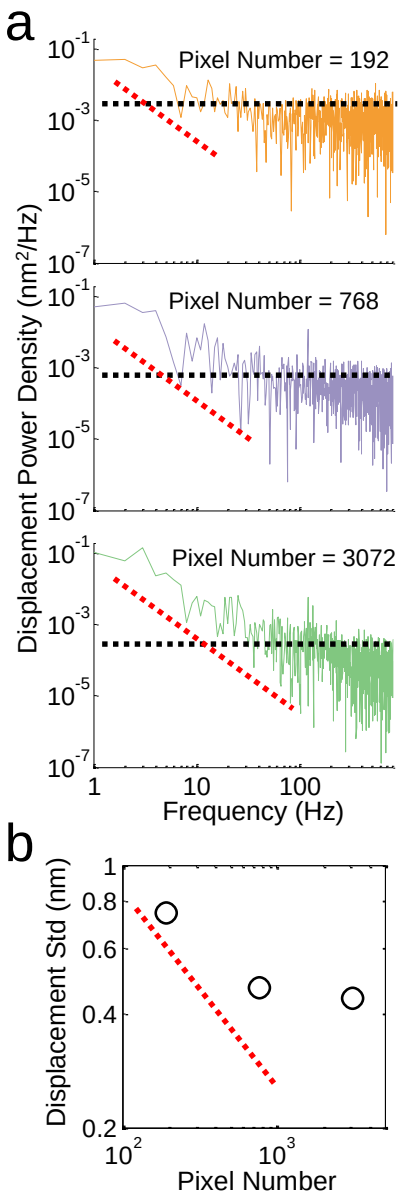

Figure 7-10 Noise Spectra and Effect of Averaging Over Multiple Pixels on Signal to Noise Ratio

a) Displacement noise power density of selected ROI with different pixel numbers, where the black dashed line indicates the level of shot noise, and dashed line indicates linear dependence of cell intrinsic noise with a slope of -2.

b) Standard deviation of displacement vs. pixel numbers.

Although the observation that mechanical waves accompany the AP is consistent

with the recent theories, the detailed local variability in the mechanical deformation calls for more detailed theories. The mechanical wave theories assume a uniform cylinder for the neuron axon, and consider primarily elastic energy associated with membrane surface area changes(El Hady and Machta 2015). Elastic energy may also be stored in the

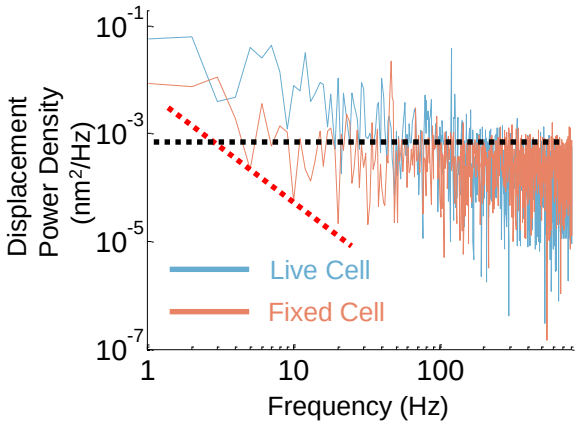

Figure 7-11 Cell Intrinsic Micro-motion Noise
Displacement noise power density of a live (blue) and fixed (red) cell, where the black dashed line marks the shot noise level, and the red dashed line indicates linear dependence of cell intrinsic noise with a slope of -2. Live cell displays 10 times higher noise level at the low frequency level than the fixed cell.

membrane curvature that is related to bending modulus(Petrov and Sachs 2002, Petrov 2006). Additionally, a more complete theory may also need to consider the local structural and mechanical variability in neurons, and the interaction of neurons with the supporting surface.

I imaged the mechanical deformation in 11 different neurons, and observed mechanical waves that accompany the AP in every neuron (Figure 7-8). I also observed the mechanical wave in cultured rat Dorsal Root Ganglion (DRG) neurons (Figure 7-9), which suggests that the mechanical waves accompany the AP is a robust phenomenon. My data also show that despite both positive and negative membrane displacements are

observed within a neuron, the absolute displacement averaged over a whole neuron displays a waveform that matches well with the simultaneously recorded AP. The average maximum displacement is ~0.3 nm, corresponding to ~4 pm/mV, but the maximum mechanical wave amplitude varies from ~0.2 to ~0.4 nm, from neuron to neuron (Figure 7-8). The width of the mechanical waveform matches that of the AP for each neuron (Figure 7-8).

The data discussed above show that the AP is accompanied by a mechanical wave in the cell membrane, and the corresponding membrane displacement is a fraction of nm. To optimize the detection of such small displacement, I analyzed different noise sources. At high frequencies (>200 Hz), shot noise dominates (Figure 7-10), which can be reduced by increasing pixel size (or number) and light intensity. However, at low frequencies (<200 Hz), the intrinsic cell micro-motions dominate the noise spectrum as shown in the Supplementary Information (Figure 7-11 and Figure 7-12).

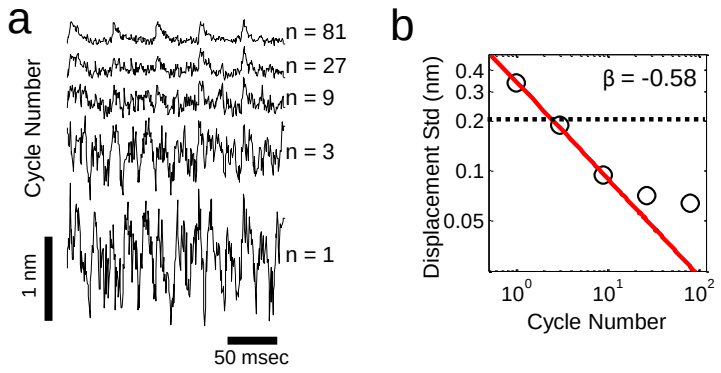

Figure 7-12 Noise Reduction by Averaging Data Over Repeated Cycle of Action Potential

a) Mechanical wave that accompanies the action potential averaged over different numbers of action potential cycle. b) Standard deviation of membrane displacement vs. number of cycle in the averaging, where the black dashed line indicates the signal level, and the red solid line is fitting of the data by a power law with an exponent of -0.58.

Conclusion

In summary, I have imaged local membrane displacement in single mammalian neurons during the initiation and propagation of the action potential, and observed that a mechanical wave accompanies the action potential. The mechanical wave and AP have similar shapes and widths, and their peaks are synchronized with each other within the temporal resolution (0.6 ms) of the present imaging method. The mechanical wave is observed in nearly every neuron studied in this work, indicating the phenomenon is universal, but the amplitudes of the mechanical waves in different neurons are different, varying between 0.2 – 0.4 nm. There is also large variability in the local membrane displacement along the edge of a neuron, both in amplitude and direction: some regions expand while others shrink. Despite the local variability, the absolute displacement of a neuron displays a waveform similar to that of the action potential. While mechanical waves are anticipated to accompany the action potential by theories, detailed descriptions of the waveform, and the local variability in the membrane displacement call for more detailed theories.

CHAPTER 8 CONCLUSION AND PERSPECTIVES

Conclusion

The major findings and contributions of my current doctoral projects include:

I. I developed a label-free imaging technique for tracking single organelle dynamics with nanometer precision. This plasmonic imaging method can track the dynamics of organelles in 3D with high localization precision (5 nm) and temporal (10 ms) resolution. Using this technique, I observed nanometer steps of organelle transportation along neurite microtubules in neurons in native state. This provides molecular-scaled information of the motor proteins behind the organelle transportation. By tracking the organelle transportation, I also reconstructed the 3D structure of neurite microtubule bundles in live cells. The technique has great potential to provide a powerful new tool for quantitative analysis of intracellular dynamic in live cells.

II. I developed a plasmonics-based imaging technique for visualizing heterogeneous subcellular displacement accompanied with electrical stimulation. I used this method to map both amplitude and direction of deformation down to subcellular level. Using this technique, I characterized electromechanical coupling of mammalian cells and discovered a bidirectional deformation mode inside cells. The results show an elastic behavior during cell deforming from Hertz to hundreds of Hertz range, mainly determined by mechanical property of the cytoplasm. This imaging technique provides a novel detecting strategy for measuring cell membrane potentials, including action potential firing in neurons.

Results of this study enable further insights into biological functions from an electromechanical aspect in systems.

III. I developed a plasmonics-based technique for imaging electrical activity in single neurons with sub-millisecond resolution. I visualized action potential in mammalian neurons using this non-invasive label-free technique. The technique also resolved the fast initiation and propagation of electrical signals. Single action potentials and ion channel related activity can also be observed. The technique sheds lights on brain imaging and neuronal circuitry studies, which will lead to a greater understanding of the mechanisms of neurodegenerative diseases.

IV. I visualized mechanical wave associated with action potential in single mammalian neurons using bright-field optical imaging technique. The shape and width of mechanical waves were similar to those of the action potential. The amplitude of the mechanical wave varies from neuron to neuron, ranging from 0.2 - 0.4 nm. I also showed the heterogeneous response of mechanical wave within a neuron. This study demonstrated the possibility of optically studying mechanical waves that accompany action potentials, which will provide new insights into understanding the physiological function of mechanical waves and unveiling the interplay between electrical and mechanical signals during action potentials.

Perspectives

All my works focused on simple mechanical sensors with quick and label-free readouts. Mechanical signatures are fundamental properties of all cells. These features can be used as physical biomarkers for monitoring change of cell status, such as stem cell differentiation and cancer cell progression. However, a huge gap remains for correlating

physical readouts and biological functions. I anticipate the optical imaging approaches will help simplify the physical measurements and potentially bridge the gap.

I demonstrated the possibility of optically measuring small deformation at extremely fast time scale. The measurement accuracy is close to the conventional approaches for small deformation detection, such as scanning microscope. However, these optical approaches described here provide spatial information and allow fast and local measurement. After pushing the measurements to nanometers and microseconds levels, I anticipate new biological phenomenon will be observed. Combining with fluorescence microscopy and other biochemical/biophysical manipulating tools, I anticipate this approach will help accelerate the understanding of biochemical mechanisms of cell mechanics.

Future works include:

I. Development of label-free imaging technique for visualizing action potential. In my works, I demonstrated the possibility of visualizing action potential associated mechanical signal with multicycle trace averaging. Developing a label-free microscopy with sensitive algorithms to resolve single action potential spikes is critical and will become a powerful tool for direct measuring action potential at large scale. Success of developing this technique will allow a large-scale mapping of hundreds of neurons at the tissue level and will be useful for studying inter-neuronal communications. Current limitation of visualizing single individual action potential spikes is from the intrinsic motion of the neurons. Practically, although amplitudes of neuron intrinsic motion and action potential induced motion are similar, they have different characteristic

features and can be potentially separated by varieties of digital signal processing methods, such as signal filtering, fitting and transformation to other spaces. To enhance the action potential associated mechanical signal, biological approaches, such as transgenic approach can also be employed. Membrane potential sensitive motor proteins, such as prestin, will be potentially a signal amplifier and indicator for mechanically-resolving action potential in neurons. In fact, this genetic encoded mechanical indicator (GEMI) approach can be a universal signal transducer for biological system and finally imaged with mechanical deformation in microscope. With combination of current algorithms in computer vision, such as video magnification, I anticipate a simple module compatible with bright-field microscopy will be available for action potential imaging and direct visualization.

II. Studying cell (electro)mechanics and its underlying mechanism by combining with fluorescence microscopy and other biochemical/biophysical tools. Since my work demonstrated the possibility of studying subcellular mechanical displacement, understanding the molecular mechanism of heterogeneous response is important. By combining with fluorescence microscope, cytoskeleton/membrane/extracellular structures can be labeled and its local mechanical response can be simultaneously measured by optical approaches in this work. Biochemical/biophysical tools will allow me to accurately perturb the system, for example, cutting single actin fiber, and studying the local mechanical response. These fundamental studies will help to elucidate the local cell mechanics in response to perturbations. Electromechanical study may also reveal

the local membrane potential distribution via quantifying local displacement response.

III. Development of fast mechanophenotyping methods using flow cytometry. My works demonstrated the possibility of studying subtle deformations at extreme high speed. This allows a fast mechanophenotyping in a flow cytometry setting. High-throughput single-cell mechanophenotyping is thus achievable. This will allow a systematical study of mechanical signatures of cancer cells, and their relationship with molecular cancer biomarkers. It will also be possible to study mechanical signature of circulating tumor cells (CTCs) and quantify cell-cell interactions, such as immune synapse formation during T-cell activation in a high-throughput manner, which is previously impossible. These studies will lead to the discovery of biophysical biomarkers and possibly provide new methods for cancer diagnosis and high-throughput screening.

IV. Label-free phenotyping with machine leaning. In principle, the cell morphology are collective results of all forces generated from inside and outside of the cells. Morphology itself at certain time with multiple cells can be viewed as different states of sampled dynamic motions at different time. Therefore, the static morphology contains the mechanical signature of cells. By quantifying the morphology with deep leaning algorithms, I would expect mechanical signature change of cells can be revealed. This would be a very simple method for reading out the physical parameters. The revealed mechanical signature alternation could be related to extracellular forces change, cell-cell interactions perturbations that induced from deficiency of surface molecules or intracellular signaling events that

hinder the cell mechanical panel. This approach will also provide a pilot study for histological phenotyping at the tissue level. Subcellular morphology such as nucleus can also be studied. Nucleus mechanics are expected to contain information about cell cycles, high order chromosomal structure that related to epigenetic states. Studying nucleus mechanics may provide new insights into stem cell differentiation and identification of lineage determination.

V. Multiplexing and systematic study of biophysical properties with biochemical approaches. I expect my work can potentially bridge the gap between biochemical research and biophysical quantification. By applying current biotechnologies, such as omics techniques, single-cell RNA-sequencing or imaging techniques, such as multiplexing fluorescence labeling, I expect to correlate the mechanical parameters with its molecular basis at the system level. This would provide a new perspective on molecular basis of cell biophysical properties. These studies will provide new insights into biochemically controlling and manipulating physical properties of the cells. I anticipate the study will lead to new discovery of other (bio/chemo)physical therapies that can control the migration and metastasis of cancer cells instead of current radiation physical therapies that only kill the cells.

.

REFERENCES

Akkin, T., C. Joo and J. F. de Boer (2007). "Depth-resolved measurement of transient structural changes during action potential propagation." Biophysical Journal **93**(4): 1347-1353.

Andersen, S. S., A. D. Jackson and T. Heimburg (2009). "Towards a thermodynamic theory of nerve pulse propagation." Progress in Neurobiology **88**(2): 104-113.

Bao, G. and S. Suresh (2003). "Cell and molecular mechanics of biological materials." Nature Materials **2**(11): 715-725.

Berlin, S., E. C. Carroll, Z. L. Newman, H. O. Okada, C. M. Quinn, B. Kallman, N. C. Rockwell, S. S. Martin, J. C. Lagarias and E. Y. Isacoff (2015). "Photoactivatable genetically encoded calcium indicators for targeted neuronal imaging." Nature Methods **12**(9): 852-858.

Bezanilla, F. (2002). "Voltage sensor movements." The Journal of General Physiology **120**(4): 465-473.

Bezanilla, F. (2008). "How membrane proteins sense voltage." Nature Reviews Molecular Cell Biology **9**(4): 323-332.

Boyden, E. S., F. Zhang, E. Bamberg, G. Nagel and K. Deisseroth (2005). "Millisecond-timescale, genetically targeted optical control of neural activity." Nature Neuroscience **8**(9): 1263-1268.

Caiazzo, M., Y. Okawa, A. Ranga, A. Piersigilli, Y. Tabata and M. P. Lutolf (2016). "Defined three-dimensional microenvironments boost induction of pluripotency." Nature Materials.

Caucheteur, C., V. Voisin and J. Albert (2015). "Near-infrared grating-assisted SPR optical fiber sensors: design rules for ultimate refractometric sensitivity." Optics Express **23**(3): 2918-2932.

Chan, D. C. (2006). "Mitochondria: dynamic organelles in disease, aging, and development." Cell **125**(7): 1241-1252.

Chen, H. and D. C. Chan (2009). "Mitochondrial dynamics–fusion, fission, movement, and mitophagy–in neurodegenerative diseases." Human Molecular Genetics **18**(R2): R169-R176.

Chen, T.-W., T. J. Wardill, Y. Sun, S. R. Pulver, S. L. Renninger, A. Baohan, E. R. Schreiter, R. A. Kerr, M. B. Orger, V. Jayaraman, L. L. Looger, K. Svoboda and D. S.

Kim (2013). "Ultrasensitive fluorescent proteins for imaging neuronal activity." Nature **499**(7458): 295-+.

Chung, S. H. and R. A. Kennedy (1991). "Forward-backward non-linear filtering technique for extracting small biological signals from noise." Journal of Neuroscience Methods **40**(1): 71-86.

Cohen, L. B. and R. D. Keynes (1971). "Changes in light scattering associated with the action potential in crab nerves." The Journal of Physiology **212**(1): 259-275.

Coste, B., J. Mathur, M. Schmidt, T. J. Earley, S. Ranade, M. J. Petrus, A. E. Dubin and A. Patapoutian (2010). "Piezo1 and Piezo2 are essential components of distinct mechanically activated cation channels." Science **330**(6000): 55-60.

Cross, S. E., Y.-S. Jin, J. Rao and J. K. Gimzewski (2007). "Nanomechanical analysis of cells from cancer patients." Nature Nanotechnology **2**(12): 780-783.

Cui, B., C. Wu, L. Chen, A. Ramirez, E. L. Bearer, W. P. Li, W. C. Mobley and S. Chu (2007). "One at a time, live tracking of NGF axonal transport using quantum dots." Proceedings of the National Academy of Sciences of the United States of America **104**(34): 13666-13671.

Darling, E. M. and D. Di Carlo (2015). "High-throughput assessment of cellular mechanical properties." Annual Review of Biomedical Engineering **17**: 35-62.

De Vos, K. J., A. J. Grierson, S. Ackerley and C. C. Miller (2008). "Role of axonal transport in neurodegenerative diseases*." Annual Review of Neuroscience **31**: 151-173.

Debanne, D. (2004). "Information processing in the axon." Nature Reviews Neuroscience **5**(4): 304-316.

Debarre, D., W. Supatto, A. M. Pena, A. Fabre, T. Tordjmann, L. Combettes, M. C. Schanne-Klein and E. Beaurepaire (2006). "Imaging lipid bodies in cells and tissues using third-harmonic generation microscopy." Nature Methods **3**(1): 47-53.

DeWitt, M. A., A. Y. Chang, P. A. Combs and A. Yildiz (2012). "Cytoplasmic dynein moves through uncoordinated stepping of the AAA+ ring domains." Science **335**(6065): 221-225.

Dou, W., D. Zhang, Y. Jung, J. X. Cheng and D. M. Umulis (2012). "Label-free imaging of lipid-droplet intracellular motion in early Drosophila embryos using femtosecond-stimulated Raman loss microscopy." Biophys Journal **102**(7): 1666-1675.

Downing, T. L., J. Soto, C. Morez, T. Houssin, A. Fritz, F. Yuan, J. Chu, S. Patel, D. V. Schaffer and S. Li (2013). "Biophysical regulation of epigenetic state and cell reprogramming." Nature Materials **12**(12): 1154-1162.

El Hady, A. and B. B. Machta (2015). "Mechanical surface waves accompany action potential propagation." Nature Communications **6**: 6697.

Evans, E. and R. Hochmuth (1978). "Mechanochemical properties of membranes." Current Topics in Membranes and Transport **10**: 1-64.

Fletcher, D. A. and R. D. Mullins (2010). "Cell mechanics and the cytoskeleton." Nature **463**(7280): 485-492.

Foley, K. J., X. Shan and N. J. Tao (2008). "Surface Impedance Imaging Technique." Analytical Chemistry **80**(13): 5146-5151.

Grewe, B. F., D. Langer, H. Kasper, B. M. Kampa and F. Helmchen (2010). "High-speed in vivo calcium imaging reveals neuronal network activity with near-millisecond precision." Nature Methods **7**(5): 399-405.

Gu, Y., W. Sun, G. Wang, K. Jeftinija, S. Jeftinija and N. Fang (2012). "Rotational dynamics of cargos at pauses during axonal transport." Nature Communications **3**: 1030.

Guan, Y., X. Shan, F. Zhang, S. Wang, H.-Y. Chen and N. Tao (2015). "Kinetics of small molecule interactions with membrane proteins in single cells measured with mechanical amplification." Science Advances **1**(9): e1500633.

Guilak, F., D. M. Cohen, B. T. Estes, J. M. Gimble, W. Liedtke and C. S. Chen (2009). "Control of stem cell fate by physical interactions with the extracellular matrix." Cell Stem Cell **5**(1): 17-26.

Heimburg, T. and A. D. Jackson (2005). "On soliton propagation in biomembranes and nerves." Proceedings of the National Academy of Sciences of the United States of America **102**(28): 9790-9795.

Hill, B. C., E. D. Schubert, M. A. Nokes and R. P. Michelson (1977). "Laser interferometer measurement of changes in crayfish axon diameter concurrent with action potential." Science **196**(4288): 426-428.

Hirokawa, N. and R. Takemura (2005). "Molecular motors and mechanisms of directional transport in neurons." Nature Reviews Neuroscience **6**(3): 201-214.

Hochbaum, D. R., Y. Zhao, S. L. Farhi, N. Klapoetke, C. A. Werley, V. Kapoor, P. Zou, J. M. Kralj, D. Maclaurin, N. Smedemark-Margulies, J. L. Saulnier, G. L. Boulting, C. Straub, Y. K. Cho, M. Melkonian, G. K.-S. Wong, D. J. Harrison, V. N. Murthy, B. L.

Sabatini, E. S. Boyden, R. E. Campbell and A. E. Cohen (2014). "All-optical electrophysiology in mammalian neurons using engineered microbial rhodopsins." Nature Methods **11**(8): 825-833.

Hodgkin, A. L. and A. F. Huxley (1952). "A quantitative description of membrane current and its application to conduction and excitation in nerve." The Journal of Physiology **117**(4): 500-544.

Hoffman, B. D. and J. C. Crocker (2009). "Cell mechanics: dissecting the physical responses of cells to force." Annual Review of Biomedical Engineering **11**: 259-288.

Howard, J. and A. A. Hyman (2003). "Dynamics and mechanics of the microtubule plus end." Nature **422**(6933): 753-758.

Huang, B., M. Bates and X. Zhuang (2009). "Super-resolution fluorescence microscopy." Annual Review of Biochemistry **78**: 993-1016.

Huang, B., W. Wang, M. Bates and X. Zhuang (2008). "Three-dimensional super-resolution imaging by stochastic optical reconstruction microscopy." Science **319**(5864): 810-813.

Huang, B., F. Yu and R. N. Zare (2007). "Surface plasmon resonance imaging using a high numerical aperture microscope objective." Analytical Chemistry **79**(7): 2979-2983.

Iwasa, K., I. Tasaki and R. C. Gibbons (1980). "Swelling of nerve fibers associated with action potentials." Science **210**(4467): 338-339.

Janmey, P. A. and C. A. McCulloch (2007). "Cell mechanics: integrating cell responses to mechanical stimuli." Annual Review of Biomedical Engineering **9**: 1-34.

Jin, L., Z. Han, J. Platisa, Julian R. A. Wooltorton, Lawrence B. Cohen and Vincent A. Pieribone (2012). "Single action potentials and subthreshold electrical events imaged in neurons with a fluorescent protein voltage probe." Neuron **75**(5): 779-785.\

Jungst, C., M. J. Winterhalder and A. Zumbusch (2011). "Fast and long term lipid droplet tracking with CARS microscopy." Journal of Biophotonics **4**(6): 435-441.

Kerssemakers, J. W., E. L. Munteanu, L. Laan, T. L. Noetzel, M. E. Janson and M. Dogterom (2006). "Assembly dynamics of microtubules at molecular resolution." Nature **442**(7103): 709-712.

Kim, G., P. Kosterin, A. Obaid and B. Salzberg (2007). "A mechanical spike accompanies the action potential in mammalian nerve terminals." Biophysical Journal **92**(9): 3122-3129.

Kim, T.-i., J. G. McCall, Y. H. Jung, X. Huang, E. R. Siuda, Y. Li, J. Song, Y. M. Song, H. A. Pao, R.-H. Kim, C. Lu, S. D. Lee, I.-S. Song, G. Shin, R. Al-Hasani, S. Kim, M. P. Tan, Y. Huang, F. G. Omenetto, J. A. Rogers and M. R. Bruchas (2013). "Injectable, cellular-scale optoelectronics with applications for wireless optogenetics." Science **340**(6129): 211-216.

Kole, M. H. P., S. U. Ilschner, B. M. Kampa, S. R. Williams, P. C. Ruben and G. J. Stuart (2008). "Action potential generation requires a high sodium channel density in the axon initial segment." Nature Neuroscience **11**(2): 178-186.

Kole, M. H. P. and G. J. Stuart (2008). "Is action potential threshold lowest in the axon?" Nature Neuroscience **11**(11): 1253-1255.

Korchev, Y. E., Y. A. Negulyaev, C. R. W. Edwards, I. Vodyanoy and M. J. Lab (2000). "Functional localization of single active ion channels on the surface of a living cell." Nature Cell Biology **2**(9): 616-619.

Kralj, J. M., A. D. Douglass, D. R. Hochbaum, D. Maclaurin and A. E. Cohen (2012). "Optical recording of action potentials in mammalian neurons using a microbial rhodopsin." Nature Methods **9**(1): 90-U130.

Kural, C., H. Kim, S. Syed, G. Goshima, V. I. Gelfand and P. R. Selvin (2005). "Kinesin and dynein move a peroxisome in vivo: a tug-of-war or coordinated movement?" Science **308**(5727): 1469-1472.

Kuznetsova, T. G., M. N. Starodubtseva, N. I. Yegorenkov, S. A. Chizhik and R. I. Zhdanov (2007). "Atomic force microscopy probing of cell elasticity." Micron **38**(8): 824-833.

Leckband, D. (2000). "Measuring the forces that control protein interactions." Annual Review of Biophysics and Biomolecular Structure **29**(1): 1-26.

Levental, I., P. C. Georges and P. A. Janmey (2007). "Soft biological materials and their impact on cell function." Soft Matter **3**(3): 299-306.

Lin, M. T. and M. F. Beal (2006). "Mitochondrial dysfunction and oxidative stress in neurodegenerative diseases." Nature **443**(7113): 787-795.

Lu, P., V. M. Weaver and Z. Werb (2012). "The extracellular matrix: a dynamic niche in cancer progression." The Journal of Cell Biology **196**(4): 395-406.

Mallik, R., B. C. Carter, S. A. Lex, S. J. King and S. P. Gross (2004). "Cytoplasmic dynein functions as a gear in response to load." Nature **427**(6975): 649-652.

Martinac, B. (2004). "Mechanosensitive ion channels: molecules of mechanotransduction." Journal of Cell Science **117**(12): 2449-2460.

McDowell, E. J., A. K. Ellerbee, M. A. Choma, B. E. Applegate and J. A. Izatt (2007). "Spectral domain phase microscopy for local measurements of cytoskeletal rheology in single cells." Journal of Biomedical Optics **12**(4): 044008-044008-044011.

McMahon, H. T. and J. L. Gallop (2005). "Membrane curvature and mechanisms of dynamic cell membrane remodelling." Nature **438**(7068): 590-596.

Moeendarbary, E. and A. R. Harris (2014). "Cell mechanics: principles, practices, and prospects." Wiley Interdisciplinary Reviews: Systems Biology and Medicine **6**(5): 371-388.

Mosbacher, J., M. Langer, J. K. Hörber and F. Sachs (1998). "Voltage-dependent membrane displacements measured by atomic force microscopy." The Journal of General Physiology **111**(1): 65-74.

Mosgaard, L. D., K. A. Zecchi and T. Heimburg (2015). "Mechano-capacitive properties of polarized membranes." Soft Matter **11**(40): 7899-7910.

Mueller, J. K. and W. J. Tyler (2014). "A quantitative overview of biophysical forces impinging on neural function." Physical Biology **11**(5): 051001.

Nan, X., E. O. Potma and X. S. Xie (2006). "Nonperturbative Chemical Imaging of Organelle Transport in Living Cells with Coherent Anti-Stokes Raman Scattering Microscopy." Biophysical Journal **91**(2): 728-735.

Nan, X., P. A. Sims, P. Chen and X. S. Xie (2005). "Observation of individual microtubule motor steps in living cells with endocytosed quantum dots." The Journal of Physical Chemistry. B **109**(51): 24220-24224.

Nan, X., P. A. Sims and X. S. Xie (2008). "Organelle tracking in a living cell with microsecond time resolution and nanometer spatial precision." ChemPhysChem **9**(5): 707-712.

Nguyen, T. D., N. Deshmukh, J. M. Nagarah, T. Kramer, P. K. Purohit, M. J. Berry and M. C. McAlpine (2012). "Piezoelectric nanoribbons for monitoring cellular deformations." Nature Nanotechnology **7**(9): 587-593.

Oh, S., C. Fang-Yen, W. Choi, Z. Yaqoob, D. Fu, Y. Park, R. R. Dassari and M. S. Feld (2012). "Label-free imaging of membrane potential using membrane electromotility." Biophysical Journal **103**(1): 11-18.

Otto, O., P. Rosendahl, A. Mietke, S. Golfier, C. Herold, D. Klaue, S. Girardo, S. Pagliara, A. Ekpenyong and A. Jacobi (2015). "Real-time deformability cytometry: on-the-fly cell mechanical phenotyping." Nature Methods **12**(3): 199-202.

Pamir, E., M. George, N. Fertig and M. Benoit (2008). "Planar patch-clamp force microscopy on living cells." Ultramicroscopy **108**(6): 552-557.

Patterson, G., M. Davidson, S. Manley and J. Lippincott-Schwartz (2010). "Superresolution imaging using single-molecule localization." Annual Review of Physical Chemistry **61**: 345-367.

Peterka, D. S., H. Takahashi and R. Yuste (2011). "Imaging voltage in neurons." Neuron **69**(1): 9-21.

Petrov, A. G. (2006). "Electricity and mechanics of biomembrane systems: flexoelectricity in living membranes." Analytica Chimica Acta **568**(1-2): 70-83.

Petrov, A. G. and F. Sachs (2002). "Flexoelectricity and elasticity of asymmetric biomembranes." Physical Review. E: Statistical, Nonlinear, and Soft Matter Physics **65**(2 Pt 1): 021905.

Peyronnet, R., D. Tran, T. Girault and J.-M. Frachisse (2014). "Mechanosensitive channels: feeling tension in a world under pressure." Frontiers in Plant Science **5**.

Phillips, R., T. Ursell, P. Wiggins and P. Sens (2009). "Emerging roles for lipids in shaping membrane-protein function." Nature **459**(7245): 379-385.

Pickup, M. W., J. K. Mouw and V. M. Weaver (2014). "The extracellular matrix modulates the hallmarks of cancer." EMBO Reports: e201439246.

Plodinec, M., M. Loparic, C. A. Monnier, E. C. Obermann, R. Zanetti-Dallenbach, P. Oertle, J. T. Hyotyla, U. Aebi, M. Bentires-Alj and R. Y. Lim (2012). "The nanomechanical signature of breast cancer." Nature Nanotechnology **7**(11): 757-765.

Popovic, M. A., N. Carnevale, B. Rozsa and D. Zecevic (2015). "Electrical behaviour of dendritic spines as revealed by voltage imaging." Nature Communications **6**.

Popovic, M. A., A. J. Foust, D. A. McCormick and D. Zecevic (2011). "The spatio-temporal characteristics of action potential initiation in layer 5 pyramidal neurons: a voltage imaging study." The Journal of Physiology **589**(17): 4167-4187.

Pourati, J., A. Maniotis, D. Spiegel, J. L. Schaffer, J. P. Butler, J. J. Fredberg, D. E. Ingber, D. Stamenovic and N. Wang (1998). "Is cytoskeletal tension a major determinant of cell deformability in adherent endothelial cells?" American Journal of Physiology-Cell Physiology **274**(5): C1283-C1289.

Qiu, W., N. D. Derr, B. S. Goodman, E. Villa, D. Wu, W. Shih and S. L. Reck-Peterson (2012). "Dynein achieves processive motion using both stochastic and coordinated stepping." Nature Structure and Molecular Biology **19**(2): 193-200.

Rai, A. K., A. Rai, A. J. Ramaiya, R. Jha and R. Mallik (2013). "Molecular adaptations allow dynein to generate large collective forces inside cells." Cell **152**(1-2): 172-182.

Reck-Peterson, S. L., A. Yildiz, A. P. Carter, A. Gennerich, N. Zhang and R. D. Vale (2006). "Single-molecule analysis of dynein processivity and stepping behavior." Cell **126**(2): 335-348.

Ross, W. N., B. M. Salzberg, L. B. Cohen, A. Grinvald, H. V. Davila, A. S. Waggoner and C. H. Wang (1977). "Changes in absorption, fluorescence, dichroism, and Birefringence in stained giant axons: : optical measurement of membrane potential." The Journal of Membrane Biology **33**(1-2): 141-183.

Schindler, T. D., L. Chen, P. Lebel, M. Nakamura and Z. Bryant (2014). "Engineering myosins for long-range transport on actin filaments." Nature Nanotechnology **9**(1): 33-38.

Schneider, C. A., W. S. Rasband and K. W. Eliceiri (2012). "NIH Image to ImageJ: 25 years of image analysis." Nature Methods **9**(7): 671-675.

Shan, X., I. Díez-Pérez, L. Wang, P. Wiktor, Y. Gu, L. Zhang, W. Wang, J. Lu, S. Wang and Q. Gong (2012). "Imaging the electrocatalytic activity of single nanoparticles." Nature Nanotechnology **7**(10): 668-672.

Shan, X., I. Diez-Perez, L. Wang, P. Wiktor, Y. Gu, L. Zhang, W. Wang, J. Lu, S. Wang, Q. Gong, J. Li and N. Tao (2012). "Imaging the electrocatalytic activity of single nanoparticles." Nature Nanotechnology **7**(10): 668-672.

Shan, X., Y. Fang, S. Wang, Y. Guan, H.-Y. Chen and N. Tao (2014). "Detection of charges and molecules with self-assembled nano-oscillators." Nano Letters **14**(7): 4151-4157.

Shan, X., X. Huang, K. J. Foley, P. Zhang, K. Chen, S. Wang and N. Tao (2009). "Measuring surface charge density and particle height using surface plasmon resonance Technique." Analytical Chemistry **82**(1): 234-240.

Shan, X., U. Patel, S. Wang, R. Iglesias and N. Tao (2010). "Imaging Local Electrochemical Current via Surface Plasmon Resonance." Science **327**(5971): 1363-1366.

Shan, X., S. Wang and N. Tao (2010). "Study of single particle charge and Brownian motions with surface plasmon resonance." Applied Physics Letters **97**(22)

Sheng, Z.-H. and Q. Cai (2012). "Mitochondrial transport in neurons: impact on synaptic homeostasis and neurodegeneration." Nature Reviews Neuroscience **13**(2): 77-93.

Shrivastava, S. and M. F. Schneider (2013). "Opto-mechanical coupling in interfaces under static and propagative conditions and its biological implications." PloS One **8**(7): e67524.

Shrivastava, S. and M. F. Schneider (2014). "Evidence for two-dimensional solitary sound waves in a lipid controlled interface and its implications for biological signalling." Journal of The Royal Society Interface **11**(97): 20140098.

Sims, P. A. and X. S. Xie (2009). "Probing dynein and kinesin stepping with mechanical manipulation in a living cell." ChemPhysChem **10**(9-10): 1511-1516.

St-Pierre, F., J. D. Marshall, Y. Yang, Y. Y. Gong, M. J. Schnitzer and M. Z. Lin (2014). "High-fidelity optical reporting of neuronal electrical activity with an ultrafast fluorescent voltage sensor." Nature Neuroscience **17**(6): 884-889.

Surcel, A., W. P. Ng, H. West-Foyle, Q. Zhu, Y. Ren, L. B. Avery, A. K. Krenc, D. J. Meyers, R. S. Rock and R. A. Anders (2015). "Pharmacological activation of myosin II paralogs to correct cell mechanics defects." Proceedings of the National Academy of Sciences of the United States of America **112**(5): 1428-1433.

Tasaki, I. and P. Byrne (1990). "Volume expansion of nonmyelinated nerve fibers during impulse conduction." Biophysical Journal **57**(3): 633-635.

Tasaki, I. and P. M. Byrne (1988). "Large mechanical changes in the bullfrog olfactory bulb evoked by afferent fiber stimulation." Brain Research **475**(1): 173-176.

Tasaki, I. and K. Iwasa (1982). "Rapid pressure changes and surface displacements in the squid giant axon associated with production of action potentials." The Japanese Journal of Physiology **32**(1): 69-81.

Trepat, X., G. Lenormand and J. J. Fredberg (2008). "Universality in cell mechanics." Soft Matter **4**(9): 1750-1759.

Tsutsui, H., S. Karasawa, Y. Okamura and A. Miyawaki (2008). "Improving membrane voltage measurements using FRET with new fluorescent proteins." Nature Methods **5**(8): 683-685.

Tyler, W. J. (2012). "The mechanobiology of brain function." Nature Reviews Neuroscience **13**(12): 867-878.

Vale, R. D. (2003). "The molecular motor toolbox for intracellular transport." Cell **112**(4): 467-480.

Wang, S., X. Shan, U. Patel, X. Huang, J. Lu, J. Li and N. Tao (2010). "Label-free imaging, detection, and mass measurement of single viruses by surface plasmon resonance." Proceedings of the National Academy of Sciences of the United States of America **107**(37): 16028-16032.

Wang, W., K. Foley, X. Shan, S. Wang, S. Eaton, V. J. Nagaraj, P. Wiktor, U. Patel and N. Tao (2011). "Single cells and intracellular processes studied by a plasmonic-based electrochemical impedance microscopy." Nature Chemistry **3**(3): 249-255.

Wang, W., Y. Yang, S. Wang, V. J. Nagaraj, Q. Liu, J. Wu and N. Tao (2012). "Label-free measuring and mapping of binding kinetics of membrane proteins in single living cells." Nature Chemistry **4**(10): 846-853.

Wirtz, D., K. Konstantopoulos and P. C. Searson (2011). "The physics of cancer: the role of physical interactions and mechanical forces in metastasis." Nature Reviews Cancer **11**(7): 512-522.

Yang, C., M. W. Tibbitt, L. Basta and K. S. Anseth (2014). "Mechanical memory and dosing influence stem cell fate." Nature Materials **13**(6): 645.

Yang, Y., H. Yu, X. Shan, W. Wang, X. Liu, S. Wang and N. Tao (2015). "Label-free tracking of single organelle transportation in cells with nanometer precision using a plasmonic imaging technique." Small **11**(24): 2878-2884.

Yildiz, A., J. N. Forkey, S. A. McKinney, T. Ha, Y. E. Goldman and P. R. Selvin (2003). "Myosin V walks hand-over-hand: single fluorophore imaging with 1.5-nm localization." Science **300**(5628): 2061-2065.

Yildiz, A., M. Tomishige, R. D. Vale and P. R. Selvin (2004). "Kinesin walks hand-over-hand." Science **303**(5658): 676-678.

Zhang, P.-C., A. M. Keleshian and F. Sachs (2001). "Voltage-induced membrane movement." Nature **413**(6854): 428-432.

Zipfel, W. R., R. M. Williams, R. Christie, A. Y. Nikitin, B. T. Hyman and W. W. Webb (2003). "Live tissue intrinsic emission microscopy using multiphoton-excited native fluorescence and second harmonic generation." Proceedings of the National Academy of Sciences of the United States of America **100**(12): 7075-7080.